修士論文

# Dilution of heavy elements in galaxies and its implications

# (銀河内での重元素の希釈とその帰結)

Yuta Tarumi (垂水 勇太)

令和2年1月6日

# Contents

# Part I
# Introduction

The Universe has been attracting human's intellectual curiosity for more than 2000 years. Since astronomical objects are very far away, it is always challenging to clarify their properties. As humans develop science, more and more interpretation can be given to observational signals. The development of spectrometer allows us to investigate the spectral energy distribution of emission from astronomical objects. The development of quantum mechanics allows us to identify the existence and abundance of a certain element or molecule by the emission and absorption feature. By the modeling of stellar inner structure and explosive events like supernovae (SNe) or neutron-star merger (NSM) we learn how these elements are synthesized. Such chemical abundances are crucial probes to investigate not only the formation and evolution of astronomical objects like stars or galaxies, but also in the cosmological context like cosmic reionization.

Stellar archaeology is a powerful and (relatively) recently developed methodology to investigate high redshift Universe ($6 \lesssim z \lesssim 30$). Since the speed of light is not infinite, the simplest way to investigate the high-redshift Universe is to observe objects at high redshift. However, this is difficult from the observational point of view. If we use the cosmological parameters taken from the most recent Planck result, the luminosity distance to an object at $z = 6$ is about 200 Glyr. Compared to stars in our galaxy (which are mostly within 100 klyr), the observed flux is weaker by $\sim 10^{12}$ if the absolute luminosity is the same. Another way to investigate high-redshift Universe is to investigate the properties of nearby stars in detail, and study the formation environment of such stars. This method is named "Stellar archaeology", and also "near-field cosmology". The recent development of high-dispersion spectroscopy ($R \gtrsim 30000$) allows us to measure the abundance of elements in extreme detail. Archaeological approach will be important in the next decade.

One important research subject are Population III (Pop III) stars. All the stars we have observed contain heavy elements such as Calcium or Iron. Pop III stars are stars with primordial composition, namely $\sim 76$ % of hydrogen, $\sim 24$ % of helium, and a trace amount of lithium in mass. It is theoretically predicted that due to the lack of coolant, their mass distribution is biased to heavy end compared to nearby stars. The first part of this thesis is the work on the Pop III initial mass function (IMF) by archaeological approach. The IMF is an important information of Pop III stars, because most of stellar properties are determined by their mass. Using the abundance of elements that are synthesized in SNe, we model the history of star formation and therefore element synthesis in each dark-matter halo. Previous works assume that inside each dark-matter halo heavy elements distribute homogeneously. However, a hydrodynamics simulation of galaxies at high redshift suggests that in significant fraction ($\sim 20$ %) of galaxies the assumption is not true: a lot of galaxies with large inhomogeneities exist. For the first time, we model the inhomogeneity of galaxies in terms of Iron abundance, and estimate the effect of inhomogeneity on the prediction of Pop III IMF.

The second half of this thesis is relevant to two research topics. I briefly introduce the topics in turn. One is the r-process. The r-process is one of the most important process for heavy element synthesis. In neutron-rich environment, heavy element nuclei capture neu-

trons and increase their mass. If the neutron-capture is quicker than $\beta$-decay, the process is called "r-process". With the high-dispersion spectroscopy we can measure the abundance of r-process elements such as europium (Eu). They were previously beyond the capabilities of existing instruments because the abundance itself is quite small, and the absorption feature could not be identified with a poor resolution in wavelength. The astrophysical sites of r-process are still not understood, although we have a few candidates. The only confirmed candidate are neutron-star mergers (NSMs). In a gravitational-wave event GW170817, electromagnetic counterpart was observed. The light curve shows the feature of radioactive decay of r-process elements. However, from chemical evolution studies of our galaxy (van de Voort et al. 2019; Côté et al. 2019), some evidences are against the scenario that assume the NSMs are the dominant r-process sites. Other candidates are special kinds of SNe, such as magneto-rotational SNe (MRSNe). We can expect that for the coming decade the number of observations of stellar Eu abundance grows a lot. Therefore the quantitative modeling of r-process abundance evolution is important.

The other targets are satellite galaxies. In $\Lambda$-CDM Universe, the current standard cosmology paradigm, about 80 % of matter is dark matter, and remaining 20 % is the particles we know ("baryons": protons, neutrons, nuclei and even including electrons). The abundant dark-matter behaves as the potential well that confines "baryons" to a small region. Such confinement is required to form stars and galaxies, as they form in high density environment. In this paradigm, the halos grow by hierarchical structure formation: i.e. first smaller structures are formed, and then they grow by mergers and accretions. Satellite galaxies are the galaxies that reside in the same halo as our galaxy. Particularly, ultra-faint dwarfs (UFDs) are satellite galaxies with luminosity $L < 10^5 \mathrm{L}_\odot$. It is expected that UFDs mainly form their stars before cosmic reionization. Satellite galaxies (and particularly UFDs) are important, because stars in satellites often retain the information of the past. In terms of element synthesis, the elemental abundances of stars are (basically) locked when they are formed. Therefore from the elemental abundances of old stars we can infer the elemental abundances of gas clouds in the past. Stars in UFDs are ideal probes for gas clouds in high-redshift galaxies. Also in terms of kinematics, satellites and UFDs are important, because they may be the origins of halo stars. The origins of halo stars (stars that reside in the halo but far away from the disk) has long been a mystery. Satellite galaxies can be disrupted when they fall into the halo, and therefore they can be the origins of halo stars. The modeling of dynamical disruption is an ongoing research. As in these examples, understanding satellites and UFDs can have a lot of implications on galaxy formation and evolution, which makes them a really exciting research topics.

The second half of this thesis is to model the r-process enrichment of the UFDs. By now we have observations of Eu (a representative r-process element) abundances of stars in 14 UFDs. Interestingly, there are only two UFDs that are highly r-process enriched. This means that the origin of the r-process elements in the UFDs should be rare and prolific. A widely accepted interpretation is that the origin of the r-process enrichment in each UFD is an NSM. We follow this interpretation, and further investigate what we can learn about the UFDs and the binary neutron stars. Previous works have clarified that the exact merger (in-spiral) time and explosion energies are not very influential to Eu abundances of stars. We extend their research, to clarify which physical condition is the most influential to observed Eu abundances of stars in UFDs.

# Part II
# Metal mixing in the high-redshift Universe

## 1 Background

### 1.1 Population III (Pop III) stars

#### 1.1.1 "Metals" in the Universe

Before introducing Population III stars, first we need to explain "Metals" in astronomy. "Metals" are elements other than hydrogen (H) and helium (He). H and He are abundantly produced in the early history of the Universe ("Big-Bang nucleosynthesis"), but elements heavier than lithium do not exist in the Universe right after the Big-Bang. Astronomers call such elements "metals".

Metals play a crucial role in astronomy, particularly in star formation and galaxy evolution, because of its complex electron energy levels. In order to make small-size structure (such as stars), we need to take away the thermal kinetic energy (which originally was gravitational potential) of the gas by some channel, otherwise the large pressure of gas prevents itself from collapsing. Such processes are called "cooling". There are several cooling channels. One of the important cooling process is "metal-line cooling", in which the energy is taken away by photons emitted from transition between electron energy levels (de-excitation) of metals. H and He have a quite simple electron energy level structure, and cannot contribute to cooling if the typical internal energy of gas is below the energy difference of main quantum number $n = 1$ and $n = 2$.

The complex electron energy levels makes it possible to measure the elemental abundances in the Universe. What astronomers observe is mainly photons, and photons with energy corresponding to some electron transition can be used as the smoking gun for the existence of the element. Wanting to use the photon energy as a tracer for elements, astronomers developed elaborate techniques of spectroscopy. Currently the highest spectral resolution observation is typically $\delta\nu/\nu = R \sim 50000$, which allow us to detect and measure the abundance of many kinds of elements. The elemental abundance pattern can also be used to investigate various astrophysical objects, including Pop III stars and ultra-faint dwarf galaxies which we introduce later.

#### 1.1.2 What are the "Population III (Pop III)" stars and why are they important?

All the stars in the Universe are classified as Population I, II, or III. Pop I stars are metal-rich, and usually reside in the Galactic disk. Pop II stars are metal-poorer than Pop I stars, but still they contain significant amount of metals. Pop III stars are completely metal-free stars. Since the metal line cooling is not efficient, gases cool with "$H_2$ cooling". In Fig. 1 we show a comparison of cooling rate from atomic hydrogen, molecular hydrogen, and metals. As we

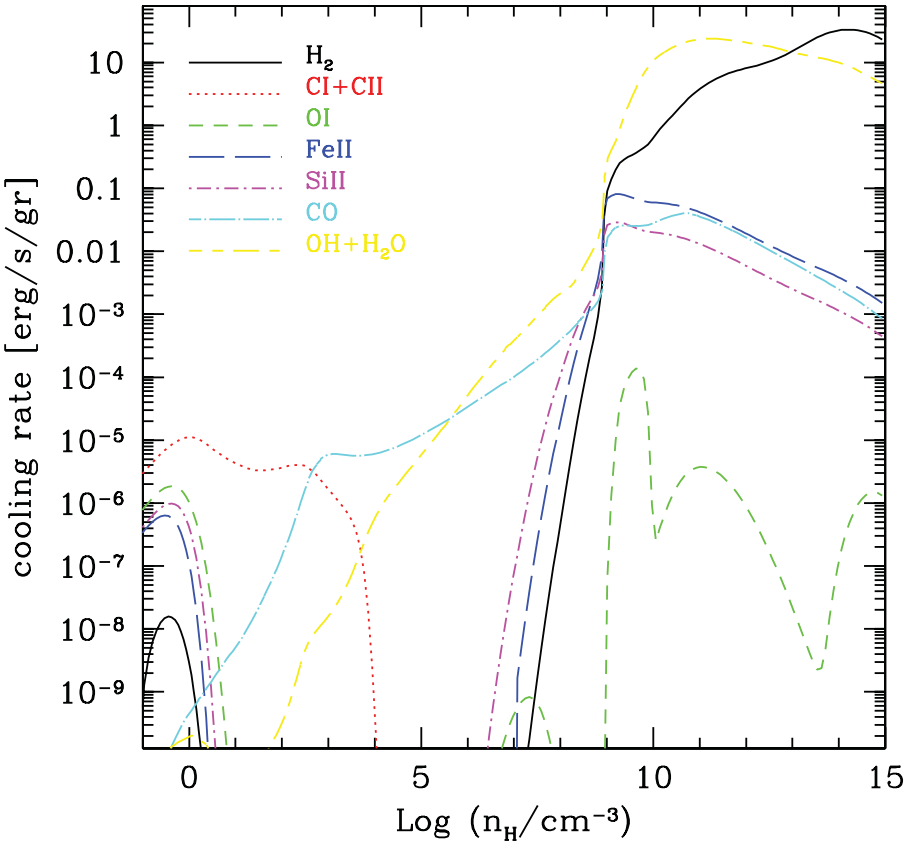


Figure 1: Cooling rates of various coolants. $H_2$ can work as a coolant, but far less efficiently: metals such as OH or CO work better than hydrogen molecules. The figure is taken from Fig. 2 of Schneider et al. (2012).

can see in the figure, this is inefficient compared to metal-line cooling, and the temperature of the gas at the time of the collapse tends to be higher than metal-richer stars like Pop I and Pop II. Higher temperature (i.e. high pressure) prevent the gases from fragmenting (i.e. downsizing), and eventually gases collapse with gravity, forming massive stars. So far, humans have never observed a completely metal-free star, so the Pop III stars are just theoretically predicted objects. Nevertheless, researchers believe the existence of the Pop III stars, and the relevant research is actively ongoing.

The Pop III stars are by itself interesting. Here we give two examples of benefits from the complete Pop III IMF. One is the understanding of fragmentation physics, and the other is stellar physics. Predicting how a gas cloud fragments is difficult. Currently hydrodynamic simulations are conducted in search of the Pop III IMF, but the results are yet to converge. If we could determine the Pop III IMF, we can understand (or we will have understood) the gas fragmentation better. Such gas fragmentation is ubiquitous all over the Universe, so such understanding is quite valuable. The other interest is in terms of stellar physics. Currently stellar physics are basically well understood, like we know a lot of properties like temperatures and lifetimes are mostly determined by its mass. However, stellar behavior is actually quite uncertain. One (in)famous problem is the death of massive stars, called "Supernovae" (SNe). Many SNe have been observed (we already have light curves, which

means we are observing the moment of explosion), therefore the stars should explode in the end. However, in simulations, stars do not (properly) explode. What astronomers are doing is artificially injecting energy in the core and blow out the stellar envelope. This problem remains as a huge obstacle to predict the metal mass ejected from SNe. Relevant to the uncertainty, the origin of intermediate-mass ($20 \sim 70 M_\odot$) black holes is still unknown. Stars with metals have strong stellar wind, as metals in the stellar atmosphere work as the source of the optical depth. The strong stellar wind blows most of the masses before the collapse, and the BH in the end typically have mass around $10 M_\odot$ at most. Whereas in Pop III stars, their stellar wind is not so strong, leaving possibility to form heavier ($\sim 30 M_\odot$) BHs. They can explain the origin of many BHs observed in gravitational waves from BH-BH merger. The investigation into Pop III stars can deepen our understanding on stellar physics.

Pop III stars are important not only by its innate interests, but also by its effects on cosmic evolution. One obvious interest is the galaxy evolution in high-redshift universe. The Universe should be reionized by $z \sim 6$ to explain Gunn-Peterson trough in the AGN spectra. Since Pop III stars are massive, they can produce a lot of ionizing photons. They are also important in the context of BH formation. With three gravitational-wave detectors (two LIGOs and one VIRGO) working, many BHs with $\sim 30 M_\odot$ are observed. Metal-rich stars have strong stellar wind, and significant mass loss before BH formation is predicted. Due to the difficulty on avoiding the stellar wind effect, Pop III stars are now considered promising as the origins of such BHs.

The Universe is being enriched with metals, and usually the fraction of metals monotonically increases with time. This means that the Pop III stars likely to reside in small galaxies in the very old Universe. However, due to the limitations of our observational reach, we can only observe each star in our galaxy (which means $z = 0$). This does not mean we cannot gain the information of the old times observationally: the metal contents of a star is fixed at the moment of formation. If we can identify "old" stars, then it is equivalent to observe the old times. The method to gain information about the past by observing old stars in our galaxy is called "stellar archaeology". Currently humans have observed a lot of metal-poor stars, but we have never observed any metal-free stars. From the non-detection of metal-free stars some researchers claim that there are no "Pop III Survivors" in the MW (Magg et al. 2019).

### 1.1.3 Are Pop III stars massive?

The difference between Pop III stars and Pop II stars is the cooling rate of the progenitor gas cloud. Since Pop III stars are metal (and also dust) free, the progenitor gas cannot cool efficiently: only the coolants are $H_2$ and HD molecules. Consequently metal-free gas collapses at high temperature like a few hundred kelvin, while metal-rich gas collapses at $\sim 10$ kelvin. In Fig. 2 I show the temperature evolution of gas taken from Omukai (2000). We can see that metal-free gas cloud remains warm while it collapses. This high temperature leads to higher fragmentation mass.

The masses of gas fragments are mostly Jeans mass, which is determined by the competition between pressure and gravity:

$$M_J = (250 M_\odot) \left( \frac{c_s}{1 \text{ km s}^{-1}} \right)^3 \left( \frac{n}{10^3 \text{ cm}^{-3}} \right)^{-1/2} \tag{1}$$

where $c_s$ is the sound velocity and $n$ is the number density of hydrogen gas. The sound velocity $c_s$ is the contribution from pressure, which is proportional to $T^{1/2}$. Therefore $M_J \propto T^{3/2}\rho^{-1/2}$. In a high temperature environment small structures cannot be formed (assuming the initial densities $\rho$ or pressures $\sim \rho T$ are the same).

One important parameter for the gas collapse is the adiabatic index $\gamma$. Suppose the gas cloud satisfies

$$PV^\gamma = const. \Leftrightarrow V \propto P^{-1/\gamma}. \tag{2}$$

We also assume that the gas follows the equation of state of ideal gas:

$$PV = NkT. \tag{3}$$

Combining these, we can have the relation between pressure $P$ and temperature $T$:

$$P \propto T^{\frac{\gamma}{\gamma-1}} \tag{4}$$

We can derive a polytropic relation from the relations above:

$$P \propto \rho^\gamma. \tag{5}$$

Then, Jeans mass $M_J$ is:

$$M_J \propto T^{3/2}\rho^{-1/2} \propto \rho^{\frac{3}{2}(\gamma-\frac{4}{3})}. \tag{6}$$

If the Jeans mass and the density positively correlates, then it does not collapse. If they negatively correlates, then it catastrophically collapses. The critical exponent is $\gamma = 4/3$. If cooling is effective, the collapsing cloud temperature is kept to almost constant, which corresponds to $\gamma = 1$. In this case the gas cloud collapses. If the cooling is inefficient, the collapse is just an adiabatic compression, in which $\gamma$ is 5/3 (if the components are in atoms) or 7/5 (if the components are in molecules). The cooling and optical depth are relevant. As long as the gas is optically thin, they can cool by radiation, and the gas collapses because the adiabatic index is close to 1. However, once the gas cloud becomes optically thick, they cannot cool and adiabatic index increases close to (5/3). Once it becomes optically thick, metallicity difference is meaningless: anyway they cannot radiate its energy away. Therefore the densities and temperatures of protostellar cores are rather similar between metal-free and metal-rich gas clouds.

The crucial difference between Pop III and Pop I/II stars is the accretion rate from the protostellar disk. The protostellar core is still small like $10^{-2}$ $M_\odot$. The mass of stars are mostly determined by the accretion from the protostellar disk. Let us estimate the accretion rate. Suppose the outer layer (accretion disk) falls freely onto the protostellar core, the accretion rate is:

$$\dot{M} \simeq \frac{M_J}{t_{\rm ff}} \simeq \rho(c_s t_{\rm ff})^3/t_{\rm ff} \propto c_s^3 \propto T^{3/2} \tag{7}$$

therefore the $\dot{M}$ is higher in metal-free gas than in metal-rich gas. This higher accretion rate leads to higher stellar mass.

In summary,

- Since metal-free gas cloud is less likely to fragment, each gas fragment is more massive ($\sim 1000$ $M_\odot$).

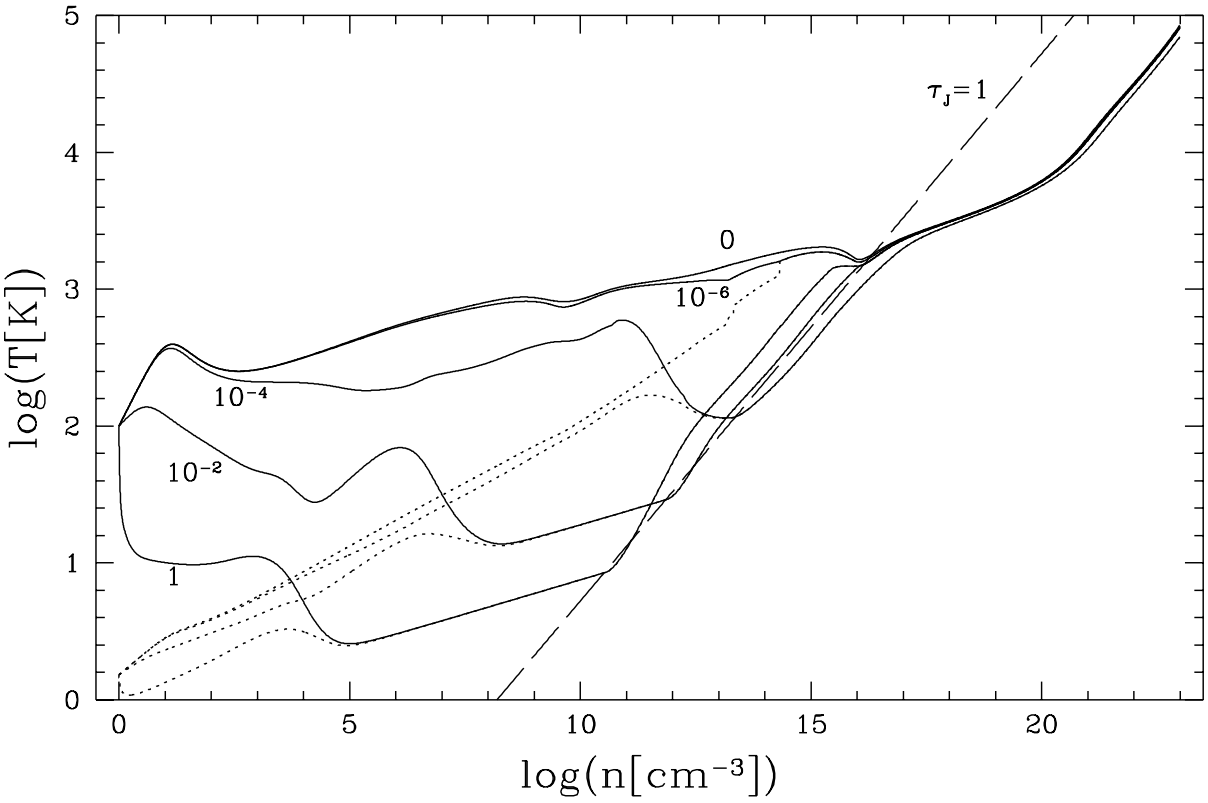


Figure 2: The temperature evolution of collapsing clouds with different metallicities. The solid curves are the evolution of gas temperature as it collapses. The number near each line is the metallicity. The figure is taken from Fig. 1 of Omukai (2000).

- However, the mass of protostellar core is almost the same as in metal-rich protostellar core.
- The key difference between metal-free and metal-rich gas clouds is the accretion rates from the protostellar disk. Pop III stars are massive because the accretion rate is high.

## 1.2 MPstars observation

The recent development of high-dispersion observation let us measure the elemental abundances of very metal-poor stars. Typical telescopes are: very large telescope (VLT), Subaru high-dispersion spectrograph (HDS, $R \simeq 60000$), Keck observatory HDS ($R \simeq 40000$) DuPont and MIKE at La Campanas observatory. They are the follow-up obsrevations from surveys like DES or SDSS.

## 1.3 CEMP stars

Carbon-enhanced metal-poor (CEMP) stars are recently investigated both theoretically and observationally. The (typical) definition is: (i) it is metal-poor ([Fe/H]$< -1$), and (ii) it is carbon-enhanced ([C/Fe]$> 0.7$). The second definition can be ([C/Fe]$> 1.0$), but the exact criterion is not important. If a CEMP star is also enriched with s-process elements (such as strontium (Sr) or barium (Ba)) or r-process elements (such as europium (Eu)), the star is called CEMP-s or CEMP-r star. If the star does not show the feature of s- or r-process, the star is called CEMP-no star. CEMP stars are important, because they give us important hints for nucleosynthesis events in the Universe. High metallicity stars like our Sun have experienced a lot of metal enrichment events. Contributions from various origins are convoluted, therefore it is quite difficult to disentangle. Usually a large number of enrichment smears out the peculiarity of each enrichment events, and the elemental abundances look more or less the same. Stars with peculiar elemental abundance leave the information of each peculiar metal production event.

Observationally there are many CEMP stars observed. In Fig. 3 we show the stellar abundance distribution of carbon and iron. It is grouped into three, but the number of groups or the grouping criteria are still on debate. The fraction of carbon-enhanced stars increases as it gets metal-poor. In Fig. 4 we show a figure from Placco et al. (2014). In this figure CEMP-s and CEMP-r stars are excluded, and only CEMP-no stars are included. Basically at lower [Fe/H] the fraction of CEMP-no stars increase. There remains a huge uncertainty in the calculation of stellar atmosphere (see, e.g. Norris and Yong (2019)).

The origin of carbon enhancement is a theoretical challenge, and many theoretical works are ongoing. For CEMP-s stars, the most promising channel is binary mass transfer (Lucatello et al. 2005). Suppose there is a binary stars. The heavier star first exhaust hydrogen in the core, and later it enters asymptotic-giant branch (AGB) phase. In this phase the stellar envelope inflates and engulfs the binary. Inside the envelope, nucleosynthesis occurs. In the AGB phase carbon and s-process elements are synthesized (Gallino et al. 1998), therefore enriching the partner with carbon and s-process elements. This scenario naturally explains the enhancements in carbon and s-process elements. However, for CEMP-r stars and CEMP-no stars, we do not have convincing scenario. For CEMP-no stars, various scenarios exist:

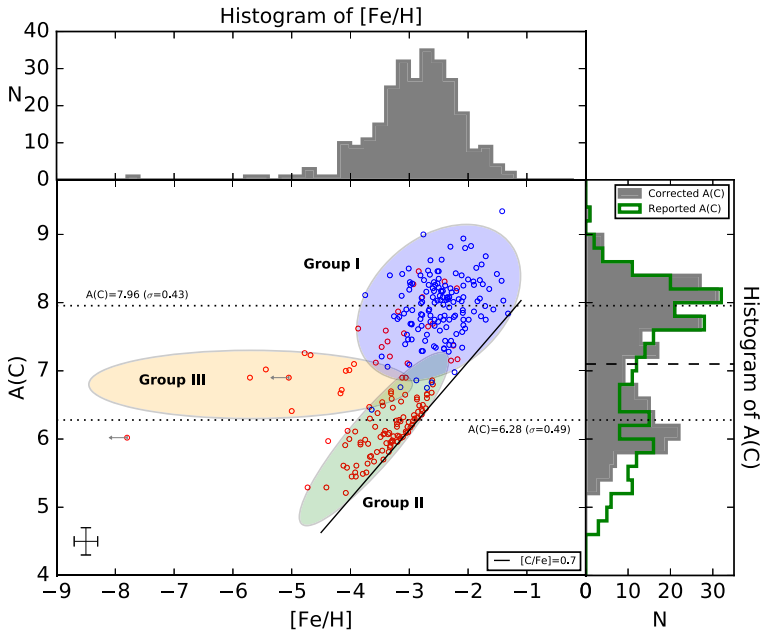


Figure 3: The distribution of carbon and iron abundances among observed stars. The blue circles are CEMP-s/rs stars, and the red circles are CEMP-no stars. Three groups are identified by observers. The classification is purely by the distribution on this plane. Group I is the most carbon-enhanced stars, which are mostly CEMP-s/rs stars. Group II is less carbon-enhanced, but still CEMP stars. Group III is moderately enriched with carbon, and they widely distribute on [Fe/H] axis. The figure is taken from Fig. 1 of Yoon et al. (2016).

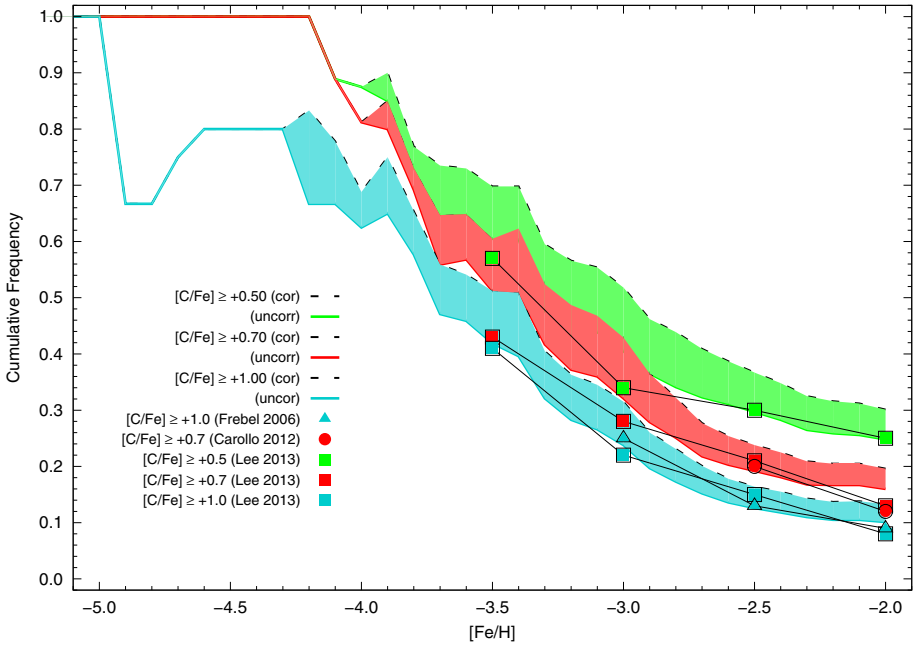


Figure 4: The fraction of CEMP-no stars in each metallicity bin. At lower [Fe/H] the stars are likely to be carbon-enhanced. However, there is a large uncertainty in this fraction coming from stellar atmosphere calculation, see Norris and Yong (2019). This figure is taken from Fig. 16 of Placco et al. (2014).

carbon enhancement from faint SNe (Ishigaki et al. 2014), mass transfer from a companion star (Arentsen et al. 2019), and inhomogeneous metal mixing (Hartwig and Yoshida 2019). There are only a few CEMP-r stars, and no plausible explanation exists.

# 2 Previous works

## 2.1 A direct simulation of SNe shock shell expansion into the environment (Smith et al. 2015)

They have pointed out that the external enrichment can be an important channel for Pop III to Pop II transition. They are mainly interested in Pop III to Pop II transition. They follow the stellar winds and explosions from Pop III stars and see how neighboring halos are enriched. In one of the cases they found that the neighboring halos are enriched to $10^{-4} \leq Z \leq 10^{-2}$ via external enrichment. They also estimated the fraction of externally enriched halos, and they report that the fraction is not large.

Their main target is to study how the stellar wind and SN shells and remnants enrich the neighboring halo. Therefore the important physics are the explosion and expansion of SN shocked shell, hydrodynamics to solve metal mixing into hydrogen gas, spatial position, and star formation. For the stellar explosion, they model the end of the free-expansion phase by injecting the energy of $10^{51}$ erg and the metal of 11.19 $M_\odot$, with the total ejecta of 38.6 $M_\odot$. For hydrodynamics, they use a simulation with adaptive mesh refinement (AMR) code ENZO

(Bryan 2014). For the spatial position, they take the initial condition to be the Gaussian random field, which is the most realistic scheme to model the initial density distribution. The most well-resolved cells have a baryon mass resolution of 0.259 $M_\odot$. For the star formation, they allow Pop III star formation if all the conditions below are satisfied:

- The baryon density exceeds $10^7 \mathrm{cm}^{-3}$.
- The gas flow is convergent ($\nabla v_{\mathrm{gas}} < 0$).
- The gas contains enough fraction of hydrogen molecules: $5 \times 10^{-4}$.
- The metallicity is less than $10^{-6} Z_\odot$.

They do not have to model the Pop II star formation because they are not interested in stellar feedback from Pop II stars: they just explicitly follow the collapse of metal-enriched gas cloud.

In Fig. 5, we show a figure from their simulation. The top panels show the wide region, and the bottom panels show the narrow region. From the bottom panels we can see that the neighboring halos can be enriched to $Z = -2$, if the halo is close to the Pop III forming halo. Note that such highly enriched halos are rather rare: in top left panels there are a lot of halos that are not enriched. They also estimate the typical separation of minihalos, and concluded that external enrichment can be a non-negligible source of Pop III to Pop II transition.

## 2.2 A direct simulation of Pop III formation, I (Hirano et al. 2014)

These are set of a state-of-the-art direct simulation of Pop III star formation. Since star formation includes physics of wide dynamic range, it is virtually impossible to follow all the evolution. In their simulation, they combine two simulations that solve two different density regimes: first they solve only the hydrodynamics from gas cloud to the formation of protostellar core, and then they include radiation to investigate the mass acquisition of protostellar core. Their main target is to investigate the relation between gas accretion rate and the resulting stellar mass.

They run a cosmological simulation with smoothed particle hydrodynamics (SPH) code. Within a large ($\sim$ 1cMpc/$h$ box, first they identify a candidate minihalo for the Pop III star formation. The candidates are chosen so that (i) they are virialized dark matter halos with density more than 200 times the average of the Universe at the moment, (ii) they are isolated, so that they are not affected by the chemical nor radiative feedbacks. Then they zoom-in the candidates, and follow the evolution until the central density of the cloud reaches $n_{\mathrm{H}} = 10^{13} \mathrm{cm}^{-3}$. This is the runaway collapse phase, in which the gases are optically thin and they can dump the energy to external radiative field.

Next they run a 2D (axisymmetric) radiation hydrodynamic simulations. The initial conditions are the based on the outputs of the cosmological simulation described above. As a result, they derive a fitting formula to predict the resulting stellar mass from the accretion rate:

$$M_{\mathrm{PopIII}} = 100 \mathrm{M}_\odot \left( \frac{\dot{M}_{\mathrm{cloud}}}{2.8 \times 10^{-3} \mathrm{M}_\odot \mathrm{yr}^{-1}} \right)^{0.8}. \tag{8}$$

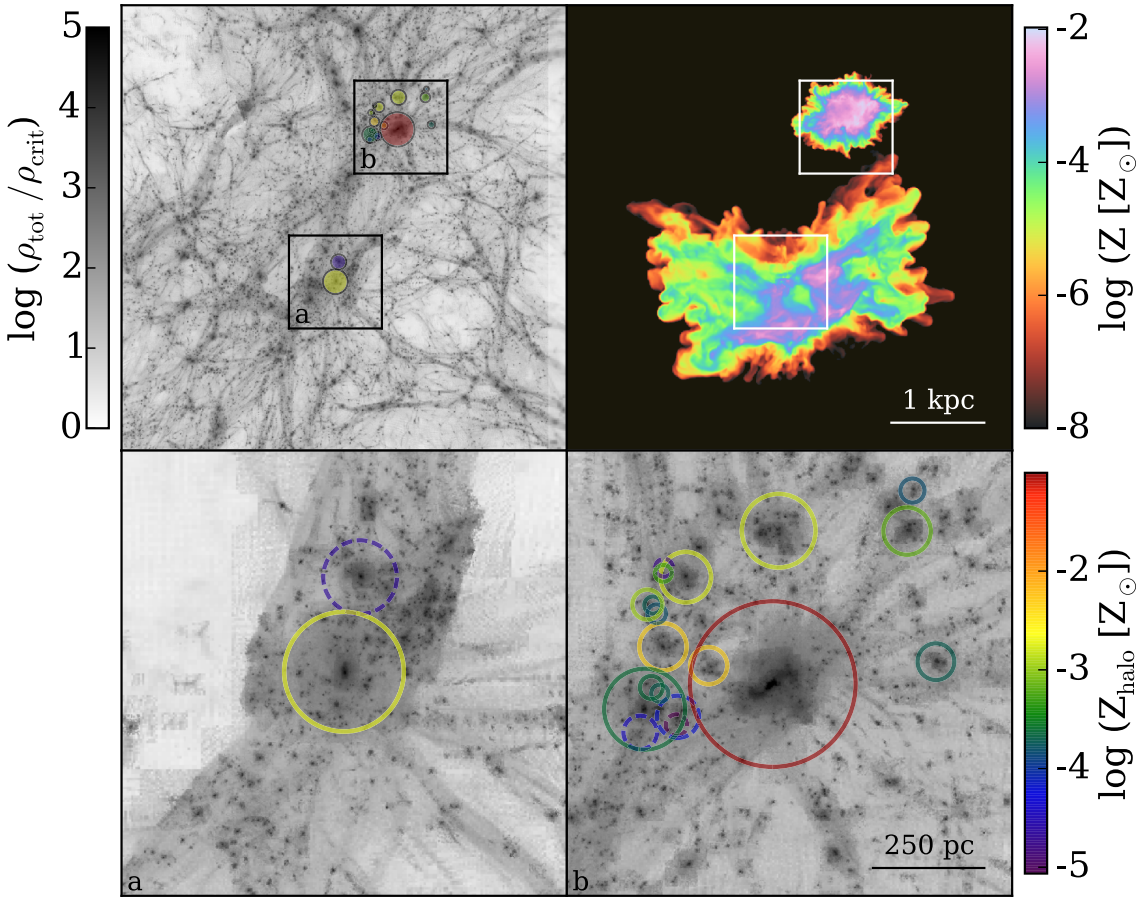


Figure 5: Figures showing the expansion of SNe ejecta to the environment. The top two panels are projections of a wide region. The top left is the density, and the top right is the metallicity. The bottom two panels are density projections of two narrow regions indicated in the top left panel. On the top right panel we can see the ejected metals mix into ambient hydrogen gas inhomogeneously. On the bottom panels, colored circles shows the metallicity of dense gas by their colors, and the virial radii by their sizes. The dashed circles are too small that they may not be able to cool and form stars. This figure is taken from Fig. 13 of Smith et al. (2015).

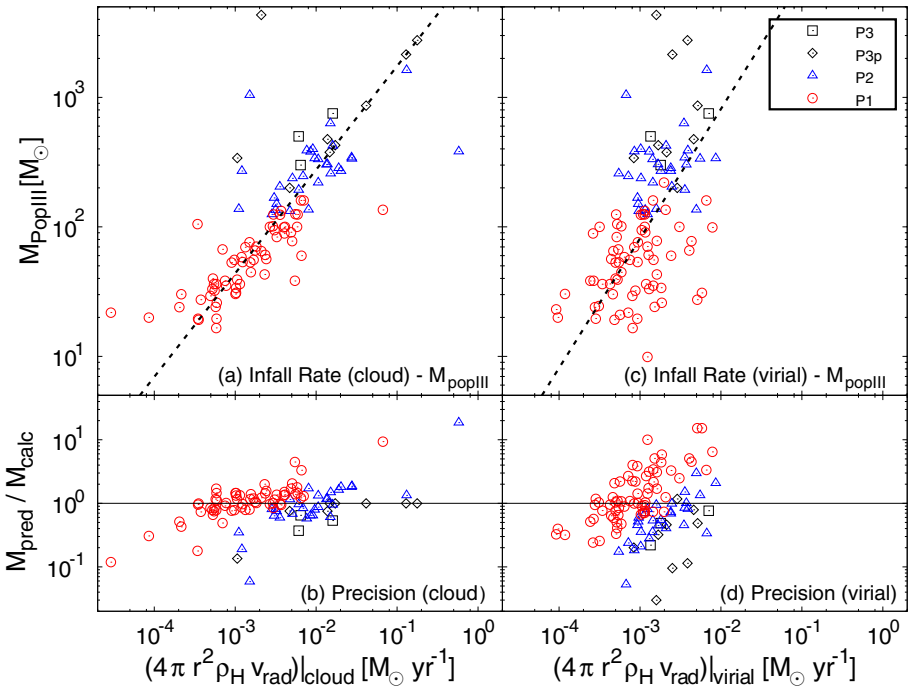


Figure 6: The relations between the mass of Pop III stars and the accretion rates. The top left panel is the relation between $M_{\rm PopIII}$ and the infall rate at cloud scale $\dot{M}_{\rm cloud}$. The dotted line is the fitting line Eq. 8. The top right panel is the relation between $M_{\rm PopIII}$ and the infall rate at dark-matter halo scale $\dot{M}_{\rm virial}$. The bottom two panels are the residuals of datapoints from the subtraction of fitting relations. The figures are taken from Fig. 14 of Hirano et al. (2014).

In Fig. 6 we show the relation between $M_{\rm PopIII}$ and $\dot{M}_{\rm cloud}$. The left panels show that if they use the fitting relation Eq. 8 they can predict the resulting stellar mass typically within a factor of two.

## 2.3 A direct simulation of Pop III formation, II (Hirano et al. 2015)

In their previous work (Hirano et al. 2014), they derive an equation that estimates the resulting stellar mass from the accretion rate onto the star-forming clouds. In this work they extend their analysis to account for the effect from different environments. They increased their sample size (1540 halos) to make statistically sound sample, and they simulate the effect of radiation from Pop III stars nearby. They claim that the star-formation mode is different by whether the region is irradiated or not. Pop III stars formed under irradiative environment (Pop III.$2_{\rm D}$) stars are more massive than those formed under no radiation environment (Pop III.1).

They implement an elaborate chemical network so that they can follow the evolution of collapsing gas cloud while taking cooling into account properly. The important molecules are $H_2$ and HD molecules: since Pop III stars do not have metal or dust, all they can use as the coolant to collapse are these molecules. They calculate the in-fall rate at Jeans radius and

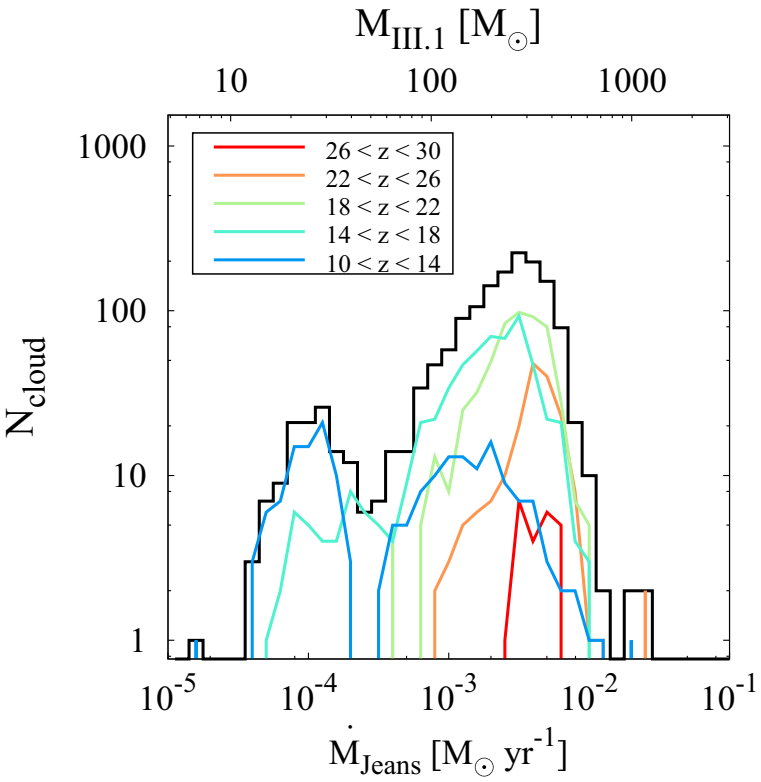


Figure 7: The in-fall rate (therefore stellar mass) distribution of Pop III.1 stars in their simulations. The gas clouds collapse with HD-cooling are typically $\dot{M}_{\rm Jeans} \simeq 10^{-4}{\rm M}_{\odot}$ (left peak), and the gas clouds collapse with $H_2$-cooling are typically $\dot{M}_{\rm Jeans} \simeq 3 \times 10^{-3}{\rm M}_{\odot}$ (right peak). On the axis on the top they show the stellar mass estimated from the in-fall rate. This figure is taken from Fig. 10 of Hirano et al. (2015).

they find that its distribution is bimodal. In Fig. 7 we show the estimated mass distribution of Pop III.1 stars.

## 2.4 Using semi-analytical approach to model the star formation in MW Hartwig et al. (2015)

This work is the first implementation of the SAM (for more information see later chapter) we used for the project. Their goal is to give a constraint on the lower limit of Pop III IMF by non-detection of metal-free stars. It has many model parameters, but they focuses on a few important parameters when they calibrate the model: the parameters are (i) Pop III star formation efficiency, and (ii) minimum mass of Pop III stars. With the calibrated model, they made predictions on (i) the lower mass limit of Pop III stars, (ii) Pop III stellar mass in each minihalo, and (iii) the conditions that cause Pop III to Pop II transition.

The SAM models physical processes in the Universe by simple analytical models. First, the SAM requires a dark-matter merger tree to work on. In this paper they prepared merger tree by extended Press-Schechter (EPS) method. On each halo in the merger tree, the SAM assumes a galaxy. The halos are metal-free when they are initialized. Star formation occurs

when a halo meets all the conditions for the star formation. For Pop III star formation, the conditions are: (i) the halo is massive enough to form $H_2$ molecules, (ii) dynamical heating by galaxy merger is not too strong, (iii) the galaxy is metal-free, and (iv) Lyman-Werner (LW) radiation is not too strong so that $H_2$ molecules can survive and work as a coolant. For Pop II/I stars they adapt a rather simple model, motivated by a cosmological simulation.

First they calibrate the Pop III star formation efficiency $\eta_*$ by comparing the Thomson scattering optical depth to its model prediction[1]. Thomson scattering is a scattering of photons by free electrons. In cosmological context the photons are cosmic microwave background (CMB) photons, and the electrons are intergalactic ones. We can measure the optical depth $\tau$ from the cross correlations of polarizations of CMB. After cosmic reionization ($z \sim 8$), the Universe is anyway ionized: therefore no effect can be observed by the difference of Pop III star formation models. Before the cosmic reionization, when the hydrogen atoms repeatedly reionized and recombined, the contribution to $\tau$ is sensitive to the Pop III star formation model. The $\eta_*$ is calibrated to $\eta_* = 0.01$. They also check the calibration by (i) the metal enrichment history by comparing to the metallicities of damped Lyman-$\alpha$ (DLA) systems, and (ii) the strength of unresolved X-ray background. In both comparisons the SAM model prediction is consistent to existing observations.

Having determined the Pop III star formation efficiency $\eta_{\rm III}$, next they investigate the Pop III survivors today. The important value for the Pop III survivors is the total Pop III stellar mass in the MW. This is easily accessible if the $\eta_*$ is already determined. They do not explicitly give the quantity, but they calculate the predicted number of Pop III survivors for each $M_{\rm min}$, the lower mass limit of Pop III stars. From the number of survivors today $N_{\rm surv}$ and the total number of stars in the MW they can execute a statistical test: Assuming the observation is a random sampling of existing stars, what is the possibility that there are $N_{\rm surv}$ of Pop III survivors but we have never observed any of them? If this value is small (like less than 5%), we can eliminate the possibility that there are more than $N_{\rm surv}$ of Pop III survivors in the MW. With this method, they obtain the constraints on the $M_{\rm min}$. In Fig. 8 we show the figure that shows the constraints on the $M_{\rm min}$. The red, green, and blue curves are the required sample sizes to eliminate the $M_{\rm min}$ model at significance level 68.27%, 95.55%, and 99.75%. The curve on the left shows the estimate for the halo stars, and the curve on the right shows the estimate for the bulge stars. The arrows on left-top are the number estimates of stars that are already observed. The halo stars are already in a good range: models that allow low-mass Pop III stars can already be excluded. For example, Pop III IMF with $M_{\rm min} = 0.65{\rm M}_\odot$ is already excluded with 95% confidence level.

## 2.5 Constraining the lower limit of Pop III IMF by the non-detection of Pop III stars (Magg et al. 2018)

They use the previous version of A SLOTH to investigate which galaxy is likely to host Pop III survivors. Before this work many of SAMs are based on EPS merger trees. However, when we discuss about formation of Pop III stars, spatial information is important. For example when we take into account external effects like chemical enrichment and LW photon

[1]Note that their definition of $\eta_*$ is a bit different from usual definition: $M_* = \eta_{\rm III} f_{\rm LW} \frac{\Omega_{\rm b}}{\Omega_{\rm m}} M_{\rm halo}, \eta_{\rm III} = \eta_* f_{\rm LW}$, where $f_{\rm LW} \simeq 0.06$

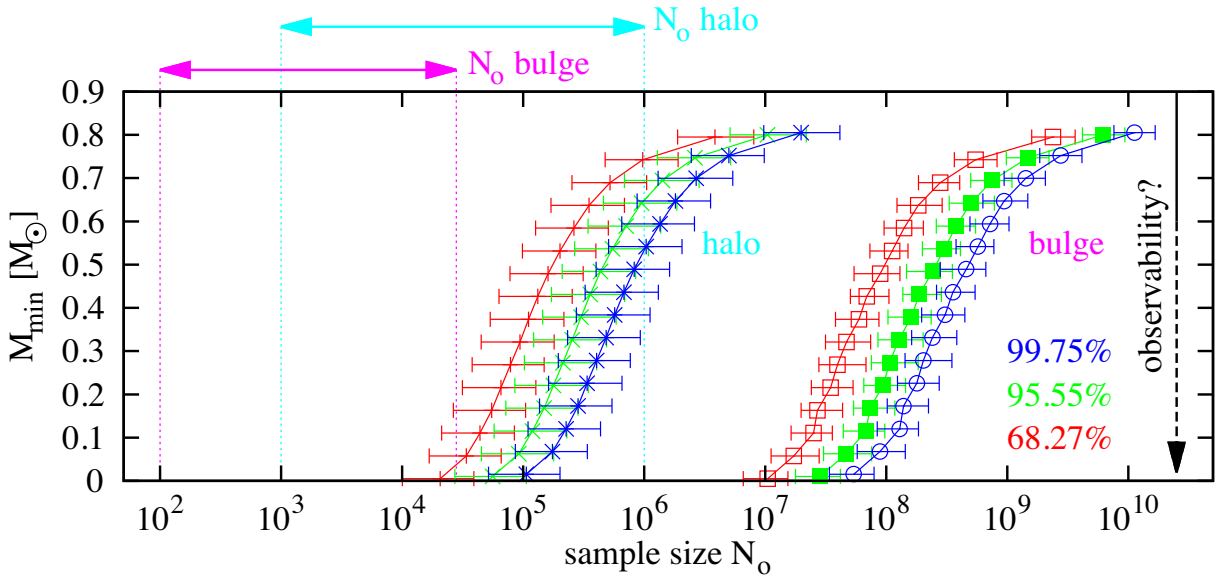


Figure 8: A figure shows the constraints on the lower IMF limit. The curves of three different colors correspond to different significance level they use. The three curves on the left are the constraints obtained by taking halo stars as the sample, and the other three on the right are the ones by taking bulge stars as the sample. The two arrows on the top left are the current sample sizes of halo stars and bulge stars. The figure is showing that the current sample size of halo stars is already enough to set limit on the lower limit of Pop III IMF. This figure is taken from Fig.12 of Hartwig and Yoshida (2019).

fluxes from neighboring halos, we need distances to the halos nearby. They use merger trees extracted from a N-body simulation (Griffen et al. 2016). With the merger trees with spatial information, they construct models to properly take (i) chemical feedback, and (ii) radiative feedback from stars into account. They argue that if we want to find Pop III survivors, the best strategy is to look for satellite galaxies, especially small ones.

The SAM is an extension of Hartwig et al. (2015). Their improvements are interactions between halos in terms of chemical enrichment and radiation. When a star formation occurs in a halo, they assume there is an "metal-rich bubble" that expands from the halo. The radius expands monotonically. The expansion speed is assumed to be constant, assuming feedbacks from multiple stars contribute to the driving power of the radius expansion. After Pop III star formation, the shell expands for "recovery time" $t_{\rm recov} = 100$Myr. After $t_{\rm recov}$, Pop II star formation occurs and the expansion of "metal-rich bubble" is delegated to Pop II star formation. The star formation also contribute to radiative feedback. The important photons are ionizing photons ($h\nu > 13.6$eV) and LW photons ($13.6 > h\nu > 11.2$eV). Around a star-forming halo, they can define an ionized region. The ionization has an effect to hinder star formation although it does not completely quench. The LW radiation is implemented as an uniform background radiation: this effect delays Pop III star formation by photodissociating $H_2$ molecules.

In Fig. 9 we show the fraction of Pop III survivors in galaxies as a function of stellar mass. The figure clearly shows that the Pop III survivors likely to reside in galaxies with small stellar mass. This is natural because in large galaxies the number of Pop II stars is large, therefore decreasing the fraction of Pop III survivors. They also give estimates on the number of Pop III survivors that are in red giant branch (RGB) (so that they are sufficiently bright to be observed). They find that satellite galaxies with $M_* \simeq 10^5 M_\odot$ host one Pop III survivor that is in RGB phase on average. This estimate led them conclude that if the minimum Pop III mass is less than 0.8 $M_\odot$, we can find Pop III survivors by closely investigating the stars in dwarf galaxies.

## 2.6 Observationally constraining the survival of Pop III stars (Magg et al. 2019)

They argued that from the fact that we have never observed any Pop III stars we can constrain that there are no Pop III survivors in the MW. The key feature is that they use the observational bias: extremely metal-poor (EMP, [Fe/H] $< -3$) and ultra metal-poor (UMP, [Fe/H] $< -4$) stars are likely to be investigated in detail and reported. They use a simple statistical argument that "If the probability of metal-free stars among EMP (UMP) stars is $P_{\rm EMP}(P_{\rm UMP})$, the probability of non-detection is $(1 - P_{\rm EMP})^{N_{\rm EMP}}((1 - P_{\rm UMP})^{N_{\rm UMP}})$". They claim that current observational sample size of UMP stars is already enough to exclude the models with a lot of Pop III survivors.

They calculate the number of Pop III survivors in the MW by a top-heavy IMF: log-flat from $0.6M_\odot$ to $150M_\odot$. Typically the numbers of Pop III survivors are a few times 1000, depending on which merger tree they use. Also they calculate the number of EMP and UMP stars in the MW, and derive the fractions of metal-free stars out of EMP/UMP stars. Recently a survey (Youakim et al. 2017) find that EMP and UMP stars consists of 1/800 and 1/80000 of the stars in the MW. They estimate the number of stars in the halo to be

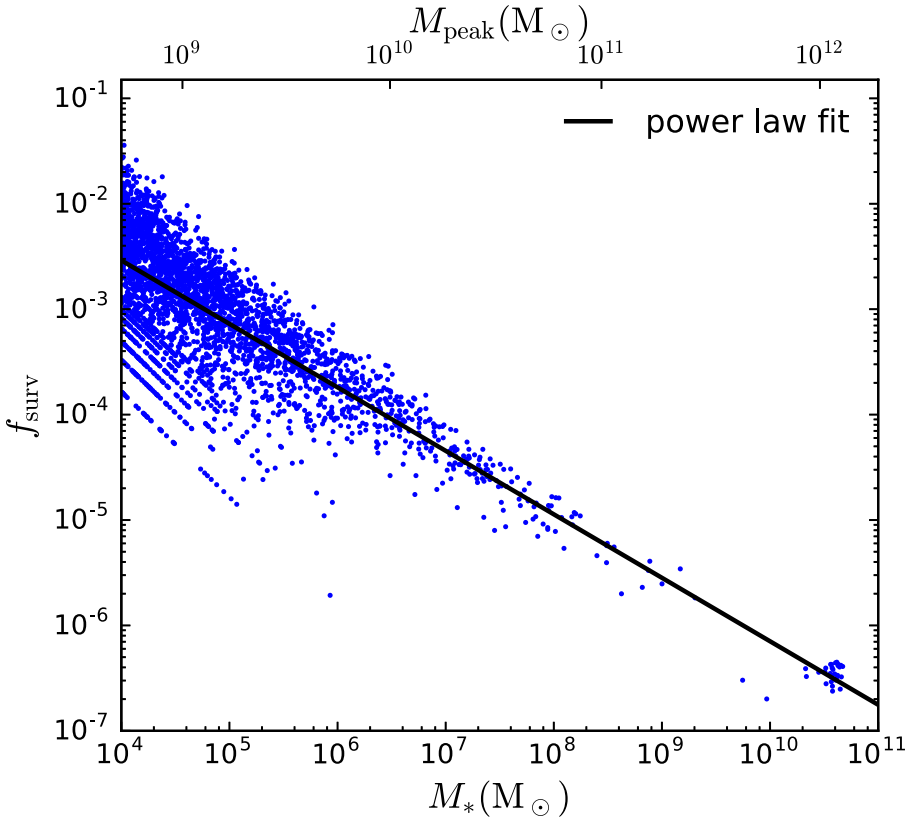


Figure 9: A figure that shows the fraction of Pop III survivors as a function of stellar mass. Since total masses of Pop III stars are not much different in any halos, the $f_{\rm surv}$ is lower in massive halos. This figure is taken from Fig. 6 of Magg et al. (2018).

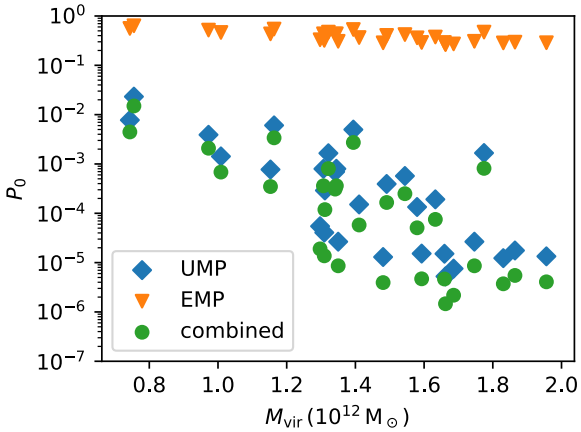


Figure 10: A figure shows the $P_0$ estimates from all the merger trees. The differences in $P_0$ comes from differences in the numbers of Pop III survivors. With EMP stars they claim that Pop III survivors should have been observed by now if they existed. This figure is taken from Fig. 2 of Magg et al. (2019).

$\simeq 1.7 \times 10^9 {\rm M}_\odot$, assuming the stellar mass in the halo to be $10^9 {\rm M}_\odot$ and the average mass of each star is $0.6 {\rm M}_\odot$. The estimated numbers of EMP and UMP stars are:

$$N_{\rm EMP,tot} = 2.08 \times 10^6 \tag{9}$$
$$N_{\rm UMP,tot} = 2.08 \times 10^4. \tag{10}$$

With the number estimates of EMP and UMP stars, they can calculate the fractions of Pop III survivors out of EMP and UMP stars $P_{\rm surv,EMP} = N_{\rm surv}/N_{\rm EMP,tot}$ and $P_{\rm surv,UMP} = N_{\rm surv}/N_{\rm UMP,tot}$. These are typically $P_{\rm surv,EMP} = 0.001$ and $P_{\rm surv,UMP} = 0.1$. The numbers of EMP and UMP stars observed are $N_{\rm EMP,obs} = 532$ and $N_{\rm UMP,obs} = 42$. Therefore the probability of not detecting any Pop III survivors can be calculated as:

$$P_{0,\rm EMP} = (1 - P_{\rm surv,EMP})^{N_{\rm EMP,obs}} \tag{11}$$
$$P_{0,\rm UMP} = (1 - P_{\rm surv,UMP})^{N_{\rm UMP,obs}} \tag{12}$$

If the $P_0$ is very small, we can exclude the null hypothesis: "the number of Pop III survivors can be calculated by an log-flat IMF from $0.6 {\rm M}_\odot$ to $150 {\rm M}_\odot$". Since the detected fraction of UMP stars is higher than that of EMP stars, $P_{0,\rm UMP} < P_{0,\rm EMP}$. Therefore the estimates with UMP stars set a better constraints. Since $(1 - 0.1)^{42} \sim 0.01$, they can exclude the Pop III IMF that they assume. In Fig. 10 I show the key figure from their paper. The differences in $P_0$ comes from differences in the numbers of Pop III survivors.

# 3 Motivation: What do we want to understand?

One obvious but far-away goal is to clarify the Pop III IMF.

In many SAMs, each galaxy is one-zone, i.e. we assume that inside the galaxies are completely homogeneous in terms of metallicity, and the stars forming in the galaxy has the same metallicity as the other gas components. However, the metal distribution can be

quite inhomogeneous: see Fig. 11. The colors show that even within one halo metallicity can be different by five orders of magnitude. In the previous version of A SLOTH (for detailed explanation please see section 4.2), there was a free parameter "dilution factor". But the distribution of the dilution factor was arbitrarily determined. My work is to improve the dilution factor: namely, determine the dilution factor as a function of some galaxy properties, by the analysis of cosmological simulation. Hereafter we call this parameter "dZ".

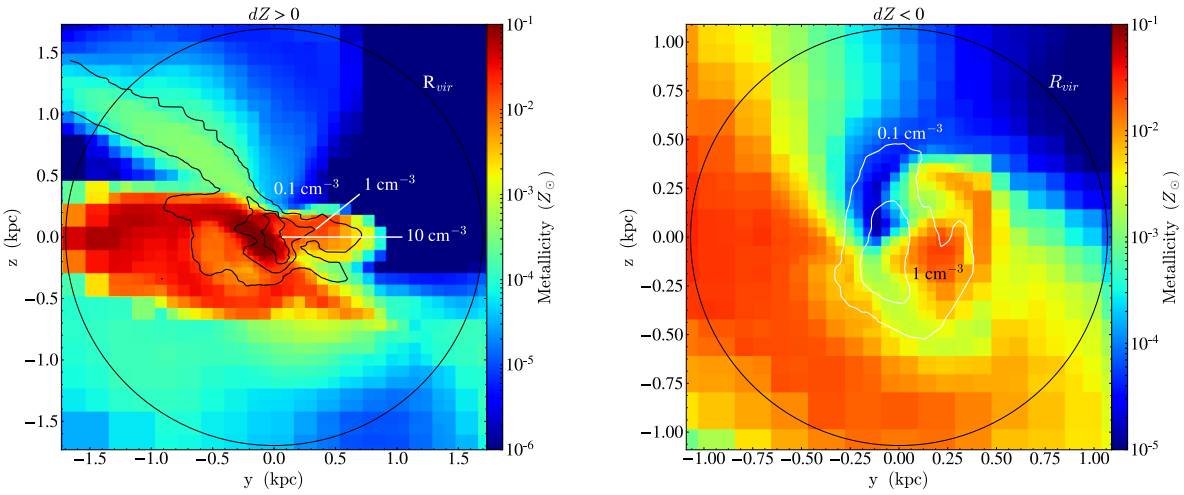


Figure 11: Two galaxies in Renaissance simulation at $z = 12$. The left panel is a galaxy in which dense gas is metal-richer than average gas. The right panel is a galaxy in which dense gas is metal-poorer than average gas. metallicity inhomogeneity can be quite large even within one halo.

The SAM is always calibrated to reproduce some observations. When we investigate the Pop III IMF with A SLOTH the most important calibration is the metallicity distribution function (MDF) at low [Fe/H]. In this case the "dZ" is crucial: wrongly distributed dZ can bias the [Fe/H] distribution, and therefore give us a wrong result. This is the first work to quantify the metallicity inhomogeneity in each galaxy and discuss the implications.

# 4 Method1: SAM

Here we explain how we model the galaxy formation in each halo. We use an semi-analytical model implemented by Tilman Hartwig and recently named "Ancient Star formation and Local Observables by Tracing Haloes (A-SLOTH)". "Semi-analytical" means that some processes are treated with simplified analytical formula, while some processes are treated with sophisticated manner. Essentially, the SAM is a modeling of galaxies inside dark matter halos. For the preparation of dark matter haloes, two options are popular: PS theory, and dark-matter only N-body calculation. Recent abundant computational power supports us to choose the N-body calculation, because the haloes have geometrical information and further modeling related to external enrichment is easier and can be physically motivatable. A-SLOTH uses the result of "Caterpillar simulation" (Griffen et al. 2016).

On each dark matter halo (and in the initial condition all haloes are metal-free), A-SLOTH judges whether the halo can form Pop III stars inside. This is determined with two criteria: whether the halo is massive enough, and whether the Lyman-Werner(LW) radiation is weak enough, both for allowing molecular cooling to form Pop III stars. The mass threshold of molecular cooling is the one in Glover (2013). I use the homogeneous LW background.

## 4.1 Pop III star formation

Pop III stars are metal-free stars. Therefore some coolant is needed to form Pop III stars. In current standard Pop III formation scenario the coolant is $H_2$ molecule. In A-SLOTH Pop III stars are formed if the main coolant is molecular hydrogen. Hydrogen molecules can be formed inside a halo that is massive enough (see Glover (2013)):

$$M = 3 \times 10^6 \mathrm{M}_\odot \left( \frac{1+z}{10} \right)^{3/2}. \tag{13}$$

This corresponds to a virial temperature of $T_{\rm vir} = 2200$ K. It is expected that if we take the streaming velocity between baryons and dark matters into account, the star formation will be delayed (Schauer et al. 2019). We do not include such baryonic streaming.

Also, photodissociation come into play (O'Shea and Norman 2008). $H_2$ molecules can be dissociated by Lyman-Werner radiation (photons with $11.2\mathrm{eV} < h\nu < 13.6\mathrm{eV}$). This LW radiation can prevent Pop III star formation particularly in small halos. In A SLOTH we require a second mass criterion as a function of LW radiation $M_{\rm LW}(f_{\rm LW})$ for Pop III star formation. The origins of LW radiation are massive stars and possibly AGNs. A SLOTH models the LW radiation flux based on Greif and Bromm (2006). Also, photoionization by newly formed stars are followed explicitly. If a halo sits in an ionized region, higher mass criterion is assigned: if the virial temperature exceeds $10^4$ K, then the halo is allowed to form Pop III stars.

Since Pop III stars are metal-free stars, a star-forming gas cloud should be metal-free to form Pop III stars. The crucial difference between Pop III stars and Pop II stars is the cooling of gas. The critical metallicity of the star formation mode transition is not identified, but typically $-6 < Z < -4$ is assumed, considering the cooling properties at such metallicities. One obvious source of uncertainty is the dust cooling. Formation of dust is not understood, therefore the relation between the amount of dust and metallicity is uncertain, which makes it difficult to calculate the contribution of dust to cooling rate. A previous work (Chiaki et al. 2017) found that observationally we have never observed any star with:

$$10^{[\mathrm{C/H}]-2.30} + 10^{[\mathrm{Fe/H}]} \leq 10^{-5.07}. \tag{14}$$

The truncation comes from the difference in dust cooling. The carbon abundance is a good tracer for carbon grain, and the iron abundance is a good tracer for silicate dust. We allow Pop III star formation if the Eq. 14 is satisfied. Once the [Fe/H] and [C/H] of a star-forming region (= [Fe/H] and [C/H] of a halo, corrected with dZ) fail to meet the Eq. 14 criterion, the star formation mode is changed to Pop II one.

In Pop III star forming halo,

$$M_* = \eta_{\rm III} \frac{\Omega_b}{\Omega_m} M_h \tag{15}$$

of Pop III stars are formed at one timestep, where $\eta_{\rm III}$ is Pop III star formation efficiency. This is a free parameter and it needs to be calibrated. The stars that are formed following a primordial IMF, which is also determined by three parameters (see below).

The initial mass of a star basically determines its lifetime and final fate. In A SLOTH, low-mass ($M_* < 10{\rm M}_\odot$) stars contribute to chemical enrichment by binary mass transfer. Stars with $10{\rm M}_\odot \leq M_* < 40{\rm M}_\odot$ stars explode as CCSNe and therefore enrich the host halo. Stars with $40{\rm M}_\odot \leq M_* < 100{\rm M}_\odot$ do not contribute to chemical enrichment since they become black holes and nothing is ejected. Stars with $100{\rm M}_\odot \leq M_* < 140{\rm M}_\odot$ stars explode as CCSNe. Stars with $140{\rm M}_\odot \leq M_* < 260{\rm M}_\odot$ stars explode as pair-instability SNe (PISNe) and highly enrich the host halo. Stars with $260{\rm M}_\odot \leq M_*$ do not contribute to chemical enrichment since they become black holes. The yield is following Nomoto et al. (2013). We also assume some fraction of $10{\rm M}_\odot \leq M_* < 40{\rm M}_\odot$ stars explode as faint SNe which is carbon-normal and iron-poor. Theoretically this faint SNe is important because they are one of the candidate of the origin of CEMP-no stars. We have one parameter "faint fraction" that needs to be calibrated. The yield of the faint SNe is from Ishigaki et al. (2014).

Some fraction of the produced metals escapes from the host halo. We assign a free parameter $f_{\rm eject}$. Another free parameter $f_{\rm fallback}$ determines the fraction of metals remain in the host halo. The sum of ejection and fallback fractions $f_{\rm eject} + f_{\rm fallback}$ is not necessarily one, but we mostly investigate the models that satisfy $f_{\rm eject} + f_{\rm fallback} = 1$. The ejected metals can enrich neighboring halos. We assume that the wind escaping from the halo have a constant velocity $110\,{\rm km\,s^{-1}}$. When this metal-rich wind hits some other halos, the halos are enriched externally.

Pop III stars can be formed in small halos like $M_h \sim 10^{6\sim7}{\rm M}_\odot$. Pop III SNe can be sufficiently energetic to blow hydrogen gas out and quench star formation for a few tens of Myr. We take this effect into account: after the internal enrichment by Pop III stars, A SLOTH waits for some time to start Pop II star formation. How long we wait is a free parameter "recovery time" $t_{\rm recov}$. The $t_{\rm recov}$ is typically $10 \sim 100$Myr (Jeon et al. 2014; Chiaki et al. 2018). When a previously pristine halo enriched by external enrichment for the first time, A SLOTH wait for one free-fall time to start forming Pop II stars. The typical free-fall time at the redshifts of interest is about 100 Myr.

## 4.2 Pop II star formation

For Pop II star formation A SLOTH uses "bathtub model" which will be explained in more detail in Magg et al. (in prep.).

On each metal-enriched dark matter halo, A-SLOTH assume 4 baryonic components:

- Hot gas $M_{\rm hot}$: Gas that has just falls into the halo. They are still too hot to form stars. We assume the hot gas is cooled within one free-fall time.
- Cold gas $M_{\rm cold}$: Gas that has cooled and can form stars. We assume the cold gas becomes stars within one dynamical time. Also, the effect of stellar feedback blows some fraction of cold gas to outside the galaxy.
- Outflow gas $M_{\rm out}$: Gas that has escaped from the halo due to stellar feedback.
- Stars $M_{*,{\rm II}}$: Pop II Stars, the direct observables.

The first three gas components share the same metallicity (i.e. This is a one-zone calculation in this sense). In order to capture the inhomogeneity in the galaxy, we add one more parameter "dZ" to modify the metallicity of the stars formed in the galaxy. This is a metallicity difference between star-forming gas and average gas.

The exchange of mass within these four components is analytically modeled. We keep the sum of four components to $(\Omega_{\rm b}/\Omega_{\rm m})M_{\rm vir}$:

$$M_{*,\rm II} + M_{\rm hot} + M_{\rm cold} + M_{\rm out} + M_{*,\rm II} = \frac{\Omega_{\rm b}}{\Omega_{\rm m}} M_{\rm vir}. \tag{16}$$

The general structure that keep the total baryonic mass to its cosmic mean calculated from the host halo mass is from Agarwal et al. (2012). The timescales and efficiencies are modified.

The following set of calculation is executed every time the halo undergo a Pop II star formation:

1. Halo initialization. Each baryon component is set to the sum of all the progenitor halos. Therefore the mass accretion rate during a time-step $\Delta t$ is

$$\dot{M}_{\rm acc} = \frac{\Omega_{\rm b}}{\Omega_{\rm m}\,\Delta t} M_{\rm h} - \left(M_{*,\rm II} + M_{\rm hot} + M_{\rm cold} + M_{\rm out}\right) \frac{1}{\Delta t}. \tag{17}$$

2. Compute various timescales and the outflow efficiency driven by star formation. The timescales of interests are:

   - The free fall time $t_{\rm ff}$. Hot diffuse gas is cooled within the free-fall time. It is defined by

$$t_{\rm ff} = \sqrt{\frac{1}{(1+z)^3\, 192\, G\rho_{\rm m}}} = 5.2\,{\rm Gyr}\,(1+z)^{-\frac{3}{2}}\,, \tag{18}$$

     where $\rho_{\rm m}$ is the cosmic matter density at z=0. Hot gas is cooled via atomic cooling. The cooling time is mostly shorter than this free fall time. Therefore this $t_{\rm ff}$ is the most important timescale for the hot gas cooling.

   - The dynamical time $t_{\rm dyn}$. Cold gas is further cooled and form stars. A SLOTH assume that cold gas and stars are concentrated within the central 5 % of the virial radius $R_{\rm vir}$ of the halo (Mo et al. 1998). With this assumption the dynamical timescale can be computed as the ratio of the size and circular velocity:

$$t_{\rm dyn} = \frac{0.05\,R_{\rm vir}}{v_{\rm dyn}} = \sqrt{\frac{(0.05\,R_{\rm vir})^3}{G\,(M_{\rm cold} + M_{*,\rm II})}}, \tag{19}$$

     where $G$ is the gravitational constant and the central dynamical velocity in the center of the halo is

$$v_{\rm dyn} = \sqrt{\frac{G\,(M_{\rm cold} + M_{*,\rm II})}{(0.05\,R_{\rm vir})}}. \tag{20}$$

The outflow efficiency is determined by the energy input from SNe and the mass of gas.

- The outflow efficiency $\gamma_{\rm out}$. A fraction of cold gas is blown out by the energy injection from stellar feedback. The $\gamma_{\rm out}$ depends on two quantities: the energy injection and the binding energy of hydrogen gas in the galaxy. The effective specific binding energy is

$$\frac{1}{2}v_{\rm eff}^2 = \frac{1}{2}\left(v_{\rm dyn}^2 + v_{\rm circ}^2\right). \tag{21}$$

The circular velocity $v_{\rm circ}$ is defined analogously to the central dynamical velocity of the halo

$$v_{\rm circ} = \sqrt{\frac{GM_{\rm vir}}{R_{\rm vir}}}. \tag{22}$$

The specific energy input of SNe is

$$e_{\rm SN} = 8.7 \times 10^{15}\,{\rm erg\,g^{-1}}, \tag{23}$$

which corresponds to one $10^{51}$ erg SN per $57\,{\rm M_\odot}$ of stars formed. The ionizing radiation is

$$e_{\rm ion} = 5.2 \times 10^{16}\,{\rm erg\,g^{-1}}, \tag{24}$$

which is equivalent to assuming (i) 30000 ionizing photons per stellar baryon (Greif and Bromm 2006), (ii) 2.0 eV thermal energy injection for each photon and (iii) an escape fraction of 10 %. We assume that feedback by ionizing photons is only efficient in haloes that are barely above the atomic cooling limit and smoothly join the two regimes together:

$$\gamma_{\rm out} = \begin{cases} 2\frac{e_{\rm SN}}{16(v_{\rm eff}-20\,{\rm km\,s^{-1}})^2} & \text{if } v_{\rm eff} > 21\,{\rm km\,s^{-1}} \\ 2\frac{e_{\rm SN}+e_{\rm ion}}{(10\,{\rm km\,s^{-1}})^2} & \text{else.} \end{cases} \tag{25}$$

This is equivalent to assuming that the outflow speed is 10 km s$^{-1}$ if ionization is the dominant driver. The exact transition point chosen so that the stellar-mass to halo-mass relation matches good to the abundance matching relation (see below).

3. Solve the following differential equations with a forward Euler method:

$$\dot{M}_{*,\rm II} = \frac{M_{\rm cold}}{t_{\rm dyn}} \tag{26}$$

$$\dot{M}_{\rm out} = \gamma_{\rm out}\,\dot{M}_{*,\rm II} \tag{27}$$

$$\dot{M}_{\rm cold} = -\dot{M}_{*,\rm II} - \dot{M}_{\rm out} + \frac{M_{\rm hot}}{t_{\rm ff}} \tag{28}$$

$$\dot{M}_{\rm hot} = -\frac{M_{\rm hot}}{t_{\rm ff}} + \dot{M}_{\rm acc}. \tag{29}$$

4. Metal mass update:

- metal mass in gas-phase decreases by (i) lock-up in stars and (ii) outflow:

$$M_{\mathrm{metals,t+\Delta t}} = M_{\mathrm{metals,t}} \frac{M_{\mathrm{cold}} + M_{\mathrm{hot}}}{M_{\mathrm{cold}} + M_{\mathrm{hot}} + \Delta M_{*,\mathrm{II,tot}} + \Delta M_{\mathrm{out,tot}}}, \tag{30}$$

  where $\Delta M_{*,\mathrm{II,tot}}$ and $\Delta M_{\mathrm{out,tot}}$ are the stellar mass and outflow mass of this time step.

- Add metals generated during this time step

$$M_{\mathrm{metals}} = M_{\mathrm{metals}} + 0.05 \Delta M_{*,\mathrm{II,tot}}, \tag{31}$$

  where we took the IMF-averaged metal yields of 0.05 $\mathrm{M}_\odot$ per 1 $\mathrm{M}_\odot$ of star formation (Vincenzo et al. 2016).

- We use snowplough algorithm to compute the size of the metal-enriched region and propagate the ionization front. For detail see Magg et al. (2018).

In short, the SAM is a modeling of stars and galaxies (the SAM predicts stellar mass, metallicity distribution, Pop III mass, ...) onto dark matter halos. The resolution is poor (there are only a few components in each halo), but computationally efficient, and it lets us investigate the effect of each physical process.

# 5 Method2: Cosmological simulation

A simulation whose initial condition is a Gaussian random field and which includes the evolution of scale factor is called "cosmological simulation". Cosmological hydrodynamic simulations are the most precise simulation of the Universe by now, but they are computationally expensive. A wide dynamic range is the obstacle. If we want to simulate the formation and evolution of galaxies, we do not follow the formation of individual stars: we put a "star particle" if a gas cell meet certain criteria. A star particle is representing a "star cluster". We follow the IMF-averaged metal and heat ejection from the particle. This is an approximate treatment, but cosmological simulations explain various physical properties like the chemical evolution of galaxies.

Cosmological hydrodynamic simulation with appropriate scale can resolve the inner (density or chemical abundance) structure of each galaxy. However it is computationally expensive, if we follow both the formation of small-scale galaxy that forms Pop III stars and the formation of large galaxies like the MW. Therefore we first analyze cosmological simulation to extract a metal mixing model of the inner structure of each galaxy, and then implement the model to less expensive A SLOTH.

First we analyze cosmological simulations to gain insight into the dZ. Particularly, we want to clarify which properties are important to determine dZ. The results of cosmological simulation is also used to gain other calibrations for the SAM. With the "dZ" models derived from the cosmological simulation, next we use a SAM "A-SLOTH" to assess the effect of the metallicity inhomogeneity on metallicity distribution function and other observables. Our purpose for using the cosmological simulation is to gain a better calibration to the parameters, concretely (i) internal enrichment fraction at $z = 12, 15$, and 18, and (ii) The inhomogeneity parameter dZ.

## 5.1 Cosmological simulation

I analyze outputs of "Renaissance simulaiton", a dataset open to public. Here we briefly explain the simulation. For more information, see Xu et al. (2016). The Renaissance simulation is a large-scale (root boxsize: 28.4 cMpc/h) cosmological simulation (= the initial condition is random Gaussian field determined at the end of inflation). They use zoom-in technique: only the region of interest is refined with finer particles and cells. In the zoom-in region, dark-matter field is represented by particles with mass of $2.9 \times 10^4 M_\odot$. The gas properties (like density, metallicity or temperature) are implemented as a field value on mesh. The code uses adaptive mesh refinement (AMR) scheme: only high density region is refined, so that the code efficiently spend its computational resources on the interesting region. The spatial resolution is 19 comoving pc at the highest resolution cell. The simulation includes (i) the gravity of dark-matter particles, (ii) hydrodynamics and thermodynamics of gas field, (iii) chemistry and radiative feedback of gas field, (iv) star formation and feedback model, and (v) transport of ionizing / dissociating photons.

The main purpose of the simulation is to study the first galaxies at $z \gtrsim 10$ before or around the cosmic reionization. They prepare three separate regions with different average densities: "Rarepeak", "Normal", and "Void". This is to study the galaxy properties in different environments. For my work we want to study the galaxies in cosmological representative region, we mainly analyze the snapshot of "Normal" at $z = 12$. In order to test the robustness of dZ distribution (see below), we also analyzed the snapshots of "Normal" at $z = 15$ and "Rarepeak" at $z = 15$, and checked that the qualitative results remained the same. When we extract the internal enrichment fraction (see below), we used snapshots of "Normal" at $z = 12, 15, 18$. We thank the Renaissance team to make the data publicly available.

## 5.2 Sample selection

My purpose is to quantify the metallicity difference between star-forming gas and average gas. Hereafter we define "dense gas" as gas denser than 1 $\mathrm{cm}^{-3}$. To check the robustness of the criterion, we compared the metallicities of dense gases with different density criteria 1, 10 and 100 $\mathrm{cm}^{-3}$, and no significant difference was observed: see Fig. 12. We regard the dense gas as the star-forming gas. For the analysis, we only analyzed halos which contain dense gas. Also, to make sure that the halo is well-resolved, we require two additional conditions: (i) the halo contain more than 1000 gas cells within its virial radius, and (ii) the halo contain more than 10 dense gas cells. The numbers of halos in the analysis set is 2743, 6150, and 1145 for Normal $z = 12$, Rarepeak $= 15$, and Normal $z = 15$ dataset.

Star-forming gas should not only be dense, but also be cold. Therefore, if we only apply density criterion to identify star-forming gas, there can be some contaminants from hot, dense gas. For example SN shocks can compress gas and make high-density region, but such gas has high temperature. We visually check the density and temperature distribution of 10 randomly sampled galaxies. The dense gas distribution did not show any shell-like structure, and also the temperature of such dense gas was lower than $10^4$ K. Therefore we expect that SN shocks do not contribute to star formation.

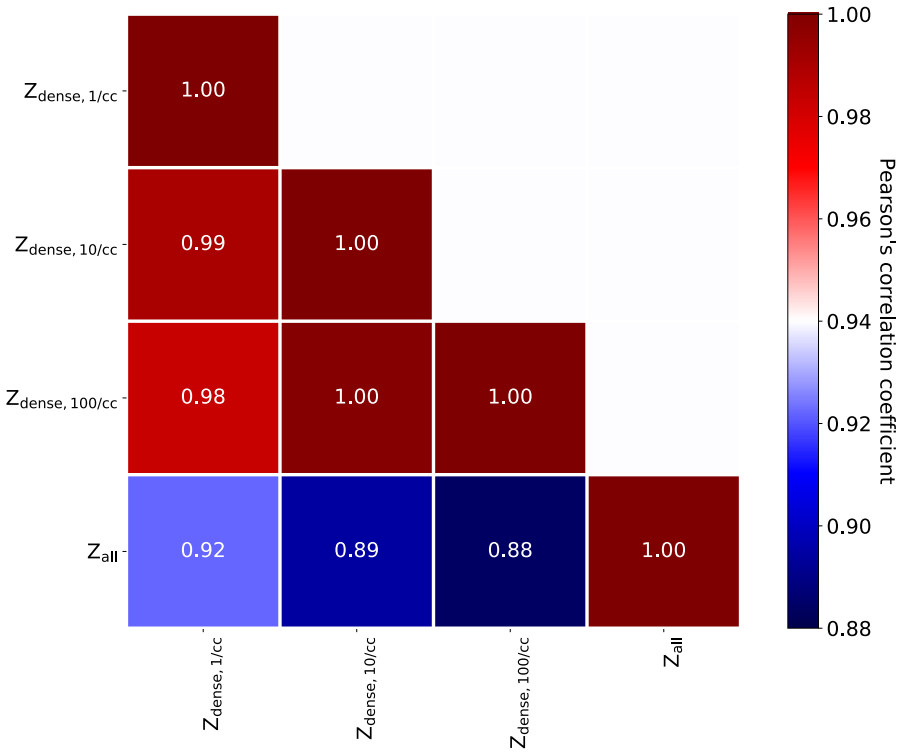


Figure 12: The correlations between metallicities of "dense gas" with different density criteria of halos without stars. The metallicities of gas denser than $1\mathrm{cm}^{-3}$ and $10, 100\mathrm{cm}^{-3}$ are almost the same, while they are somewhat different of average metallicity.

## 5.3 The metallicity shift parameter dZ

Our aim is to predict the metallicity of stars correctly. Currently the metallicity of star is assumed to be the same as the average metallicity of the galaxy. Therefore we model the difference between star-forming gas and average gas by introducing a parameter dZ:

$$dZ = Z_{\rm dense} - Z_{\rm all}. \tag{32}$$

The dZ quantifies the metallicity difference between dense gas and average of all gas in the halo. If there is a halo whose dense gas is metal-richer than average of gas inside, the dZ of the halo is positive. In Fig. 13 we show two galaxies from the sample. In the left panel, density contour and the color obviously shows that the central dense gas are metal-rich, typically $Z_{\rm dense} \simeq -2$. However, the metallicity of less dense gas is quite lower. In this case the dZ of this halo is positive. The opposite case is shown on the right panel: the dZ of this halo is negative (although it is difficult to confirm by human eye).

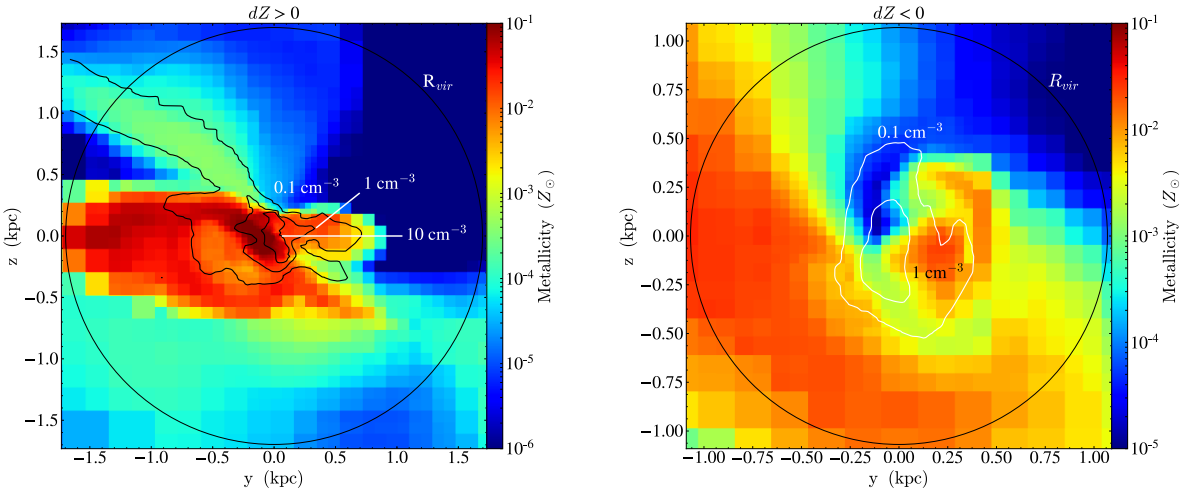


Figure 13: (Reprint) Two galaxies in Renaissance simulation at $z = 12$. The colors represent the gas metallicity. The contours represent the density contours of the galaxies. The left panel is a galaxy in which dense gas is metal-richer than average gas. The right panel is a galaxy in which dense gas is metal-poorer than average gas. metallicity inhomogeneity can be quite large even within one halo.

### 5.3.1 Interpretations for positive/negative dZ

We can think of various processes which make metallicity inhomogeneity inside each halo. The positive dZ can be realized by metal cooling. High metallicity gas cools quicker than low metallicity gas. Therefore there can be a bias: cooling, therefore star formation can take place preferentially in metal-rich region. The negative dZ can be realized by two reasons: shielding, and feedback origin. If dense gas formation happens earlier than enrichment from outside, the dense gas clump becomes metal-poorer compared to average gas. In previous

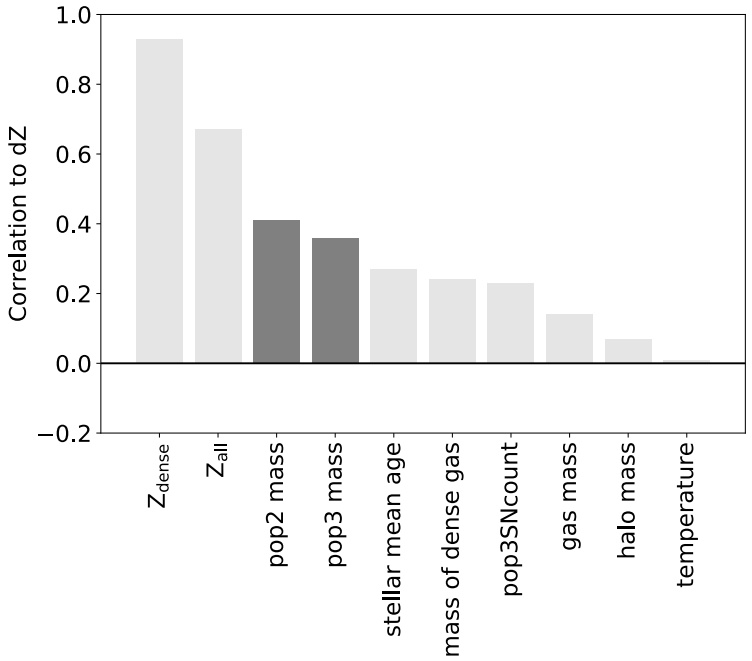


Figure 14: Pearson's correlation coefficients with $dZ$. The largest correlation is $Z_{\rm dense}$ and $Z_{\rm all}$, which is natural because they are included in the definition of $dZ$. The interesting correlation is the next parameters: pop2 mass and pop3 mass. This analysis lead me to further investigate the relation between stellar mass and $dZ$. Other parameters are not important to predict $dZ$.

studies it is supported that metal-rich wind cannot penetrate into an already dense gas clump (Jeon et al. 2014; Chen et al. 2017; Chiaki et al. 2018). Also, both the metals and energy originates from stars. Therefore metal-rich gas are likely to be hot in the first place (Emerick et al. 2018). The processes discussed above are all valid, and it is difficult to draw conclusion only with analytic estimates.

### 5.3.2 Correlations to dZ

The parameter dZ is defined on each halo. The goal here is to find a method to predict $dZ$ by parameters in SAM. First we search for the correlation between the $dZ$ and various physical properties of the galaxy. The correlations are shown in Fig. 14. We explored various parameters: Pop II stellar mass (pop2 mass: tracer for injected energy in the galaxy), Pop III stellar mass that went into SNe (pop3 mass), stellar mean age (stellar mean age: tracer for elapsed time from star formation), mass of dense gas (mass of dense gas), number of Pop III SNe in the halo (pop3SNcount, tracer for injected energy by Pop III stars), gas mass (gas mass), halo mass (halo mass), and mean temperature (temperature). The two highest correlations are natural: $Z_{\rm all}, Z_{\rm dense}$ are used to define $dZ$, therefore they can have quite a high correlation to $dZ$. The next correlations are the most interesting: stellar masses are correlated to $dZ$. We are looking into this in detail.

### 5.3.3 Internal/external enrichment

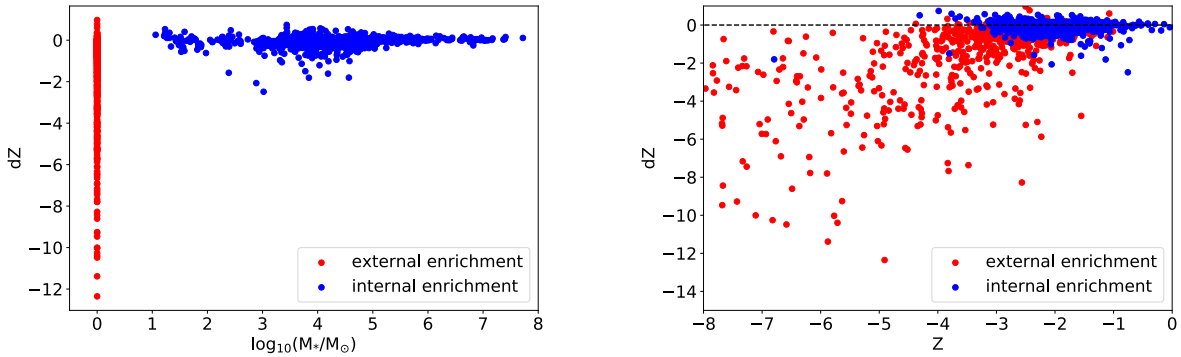


Figure 15: Scatter plot of dZ, as functions of the stellar mass and the metallicity. The left panel clearly shows a bimodality, suggesting that internal enrichment and external enrichment behave very differently in terms of dZ. We labeled halos without stars as "external enrichment", and haloes with stars as "internal enrichment". Since the horizontal axis is logarithmic, we artificially set $1M_{\odot}$ for haloes without any stars for illustration purpose. The right panel is the dZ distribution as a function of metallicity. The dZ distribution of internally enriched halos are mostly independent of metallicity, but the dZ distribution of externally enriched halos depends on the metallicity.

In Fig. 15 we show the distribution of dZ, as a function of stellar mass, and metallicity. The left panel clearly shows the bimodality between halos with stars and without stars. We split the dataset into two groups. One is "internally enriched halos", meaning that the halos contain stars, therefore they experienced internal enrichment. They may also be enriched via external enrichment, but the amount of metals is dominated by internal enrichment. The other is "externally enriched halos", meaning that the halos do not contain stars. Such halos can only be enriched externally. The internally enriched halos are shown in blue, and the externally enriched halos are shown in red. On the right panel, we show the dZ distribution as a function of average metallicity of the halo. We find the dZ behaves differently in internally enriched halos and externally enriched halos. Both for internal and external enrichment, there were no other factors that explain $dZ$. Therefore we assume that the $dZ$ is determined in a stochastic way, and we implement it that way.

### 5.3.4 The inhomogeneity dZ for internal enrichment

The inhomogeneity dZ of internally enriched halos distributes around 0, and we do not see any metallicity dependence. It means that the metallicities of star-forming gas and average gas are almost the same. We extract the $dZ$ distribution by fitting the with a Gaussian distribution function. The fitting result is $\mu = -0.03$ and $\sigma = 0.15$. The mean $dZ$ is slightly negative but almost zero, suggesting that on average star-forming gas and average gas are homogeneous in terms of metallicity. However, the distribution is a bit skewed: it has a longer tail on the negative $dZ$. The mean and standard deviation of the data points is -0.08

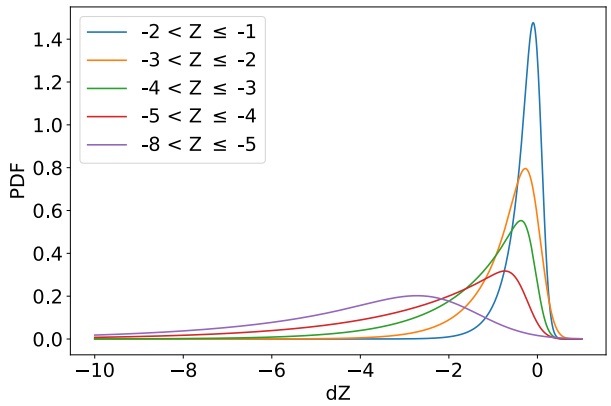


| Metallicity | $\mu$ | $\lambda$ | $\sigma$ |
|---|---|---|---|
| $-2 < Z \leq -1$ | -0.07 | 0.14 | 2.78 |
| $-3 < Z \leq -2$ | -0.01 | 0.24 | 1.41 |
| $-4 < Z \leq -3$ | 0.08 | 0.20 | 0.77 |
| $-5 < Z \leq -4$ | 0.16 | 0.19 | 0.38 |
| $-8 < Z \leq -5$ | 1.63 | 1.01 | 0.35 |

Figure 16: The left panel is the distribution functions of $dZ$ for external enrichment, and the right panel is the best-fitting parameters. These parameters are for "$-dZ$", not $dZ$ itself. We can see from the left panel that at higher metallicity $dZ$ becomes closer to zero, however they are significantly negative.

and 0.27 dex. 0.15 or 0.27 dex is actually small or comparable to other uncertainties, like observational errors coming from the stellar parameter ($T_{\rm eff}, \log g, ...$) uncertainties.

### 5.3.5 The inhomogeneity dZ for external enrichment

The importance of external enrichment for the formation of EMP stars has already been pointed out by Smith et al. (2015). The inhomogeneity $dZ$ of externally enriched halos are mostly negative. We can see this in Fig. 15. We can see an obvious increasing trend between metallicity and $dZ$, therefore we bin the metallicity with $\Delta Z = 1$ in the range $-5 < Z \leq -1$, and in $Z \leq -5$ we group them together. In each bin we calculate mean and standard deviation. Then we fit the distribution function of $dZ$ in each metallicity bin with an exponentially modified Gaussian distribution. The distribution has three free parameters, $(K, \mu, \sigma)$, and the probability distribution function $p(x; \mu, \sigma, \lambda)$ is

$$p(x; \mu, \sigma, \lambda) = \frac{\lambda}{2} \exp\left[\frac{\lambda}{2}(2\mu + \lambda\sigma^2 - 2x)\right] \mathrm{erfc}\left(\frac{\mu + \lambda\sigma^2 - x}{\sqrt{2}\sigma}\right), \tag{33}$$

where

$$\mathrm{erfc}(x) = 1 - \mathrm{erf}(x) \tag{34}$$

$$= \frac{2}{\sqrt{\pi}} \int_x^\infty e^{-t^2} dt. \tag{35}$$

The fitting results, are presented in Fig. 16. The table shows the evolution of the distribution function of $dZ$ with metallicity.

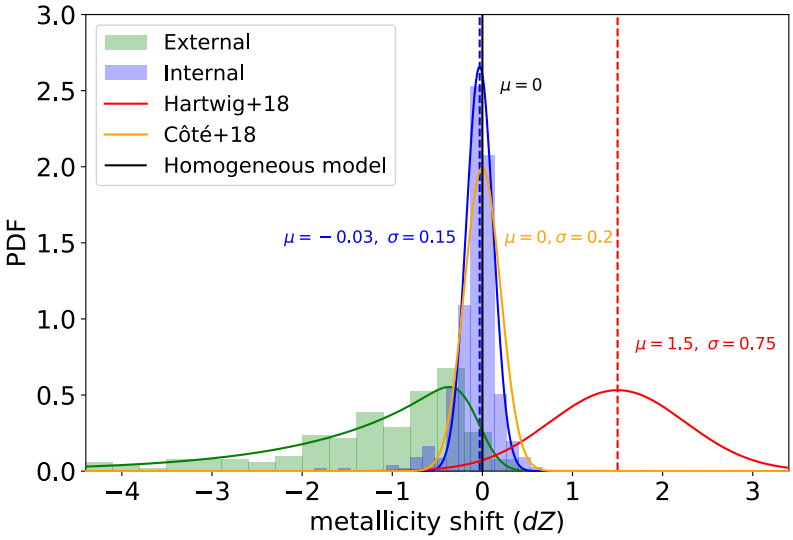


Figure 17: The comparison of $dZ$ distribution to previous research. For external enrichment we only show the distribution for $-4 < Z \leq -3$. The red Gaussian distribution is what our SAM previously assumed in Hartwig et al. (2018). The orange Gaussian distribution is the assumption in Côté et al. (2018). The black vertical line is the corresponding $dZ$ distribution in homogeneous models, such as de Bennassuti et al. (2017).

### 5.3.6 Implementation

Here we explain the implementation of the $dZ$ distribution derived above. In our SAM, at each timestep, star formation can occur. At the moment of star formation, if the halo of interest already have stars (whether Pop II or Pop III) we assume it is internally enriched. If the halo do not have stars at all, then we assume it is externally enriched. Then we pull one value from (internal/external) $dZ$ distribution randomly to determine the $dZ$ of the star formation event.

### 5.3.7 Comparison to previous research

In Fig. 17 we compare our $dZ$ distribution to other researches. This parameter has not been implemented explicitly in other research, but we can extract the corresponding parameter. In homogeneous models, since they calculate the stellar metallicities by galactic average metallicities, $dZ$ is always zero (black vertical line). In another SAM by Côté et al. (2018), a similar treatment is implemented. On the MDF calculated by simple mass argument, they convolve a Gaussian with $(\mu, \sigma) = (0, 0.2)$ to make their MDF fits better to observation. This distribution is quite similar to our $dZ$ for internal enrichment. In previous implementations of our SAM, the produced metals mix only with dense (and star-forming) gas, and the corresponding $dZ$ is mostly positive. However, the analysis of cosmological simulation suggests that this is not the case: metals are mixed well inside halo in internal enrichment, and in external enrichment metals are rather at low-density region.

In previous works some sub-grid models for Pop III formation was used in Sarmento

et al. (2017; 2019); Safarzadeh et al. (2018a). They model pristine fraction into each gas cell, and they allow Pop III star formation even in metal-rich gas cells. Their model is useful to follow the residual Pop III star formation in enriched region. The purpose of our model is to improve the calibration of our SAM by taking inhomogeneous mixing into account. For this purpose the difference of metallicity between star-forming and average gas, not the pristine fraction, is the most important value that should be modeled.

Another important research is Hirai and Saitoh (2017). They include a diffusion model in their SPH simulation. They model the exchange of masses (which is diffusion of metal on sub-grid scale) by metallicity gradient, shear, and a scaling factor (which is a model parameter). They calibrate the scaling factor by comparing the elemental abundance pattern. As a result they concluded that the metal mixes well within 40 Myr, shorter than the dynamical time (and therefore star-formation duration) of typical dwarfs. This means that in their simulation hydrogen gas and metals mix well. This is consistent to our internal enrichment result:

# 6 Result

Here we present the calibration of the SAM based on MDF, and discuss the effect of dZ. We also show other observables are reproduced as well.

Since the SAM "models" physical processes "analytically", and often the model parameters are not well constrained, we need a parameter calibration. In our work, the parameters are determined to reproduce some existing observation. Namely:

- Metallicity distribution function (MDF)
- Stellar mass - halo mass relation
- Internal enrichment fraction
- Thomson scattering optical depth

Other calibrations are included implicitly, when we choose the parameter ranges to sweep. We will explain a bit more in detail.

## 6.1 Metallicity distribution function (MDF)

The most important calibration is the metallicity distribution function (MDF). This is a distribution of stellar metallicities in the MW. [Fe/H] is often used as a tracer for metallicity, because we cannot obtain abundance of all elements, and Fe is an element relatively easy to measure. Our purpose here is to obtain the "best-fit" Pop III IMF. Therefore we only use extremely metal-poor (EMP) stars: stars with [Fe/H] $\leq -3.0$. Metal richer stars are also affected by later stars, and the inclusion of them can weaken our constraining power. For observational data we use 427 EMP stars from the SAGA database (Suda et al. 2008), which is updated at January 2019. We only include stars measured with a spectral resolution $R > 30000$, and we only include stars with iron detection. Also, stars that reside outside the central 300 kpc are excluded, in order to eliminate poorly-resolved halos at the edge of the simulation box.

Table 1: Parameter values in our fiducial model. This set of parameters best reproduces the MDF at [Fe/H] $\leq -3$ as we show below. We fix the Pop III metal fallback fraction at $f_{\rm fallback} = 1 - f_{\rm eject}$.

| Parameter | Value |
|---|---|
| Pop III SFE | $\eta_{\rm III} = 3 \times 10^{-3}$ |
| fraction of faint SNe | $f_{\rm faint} = 0.3$ |
| Pop III metal ejection fraction | $f_{\rm eject} = 60\%$ |
| lower IMF limit | $M_{\rm min} = 2{\rm M}_\odot$ |
| upper IMF limit | $M_{\rm max} = 180{\rm M}_\odot$ |
| IMF slope | $\alpha = 0.5$ |
| recovery time | $t_{\rm recov} = 50$ Myr |

We need a criterion for MDF comparison. We use the one-sample Kolmogorov-Smirnov (KS) test between A SLOTH prediction (continuous distribution) and 427 metallicities of EMP stars (427 discrete data). We run our SAM on 30 independent MW-like halo trees extracted from Caterpillar simulation (Griffen et al. 2016). Here we explain in a bit more detail. First, we run SAM on each tree, and obtain MDF. Then we execute the KS test on each MDF (so we execute KS tests for 30 times for one parameter set) and the observed data. The null hypothesis here is "The observation of 427 stars are randomly sampled from the model MDF". Finally we obtain 30 p-values, and we count the number of trees that pass the KS test at 1% significance level for each parameter set.

The model parameters are calibrated so that the number of KS test-approved trees is maximized. Our calibrated model parameters are presented in Table. 1. The calibrated Pop III IMF has a slope $\alpha = 0.5$ with the minimum mass $M_{\rm min} = 2{\rm M}_\odot$ and the maximum mass $M_{\rm max} = 180{\rm M}_\odot$. For this parameter set, all trees pass the KS test. Hereafter we only discuss models that have only one different parameters from the fiducial model. Other set of parameters, ($t_{\rm recov} = 60$ Myr and $f_{\rm ej} = 80\%$) also allowed all trees to pass the KS test. We compare these parameter sets to the fiducial by additional criteria: KS test with 5% significance level, and internal/external enrichment fractions. The 5% significance level KS test eliminates ($f_{\rm ej} = 80\%$) model, and the external enrichment fraction comparison picks up the fiducial model parameters.

In Fig. 18 we show the comparison of primordial IMFs between our calibration and a direct simulation (Hirano et al. 2015). Our calibrated IMF disfavors very massive stars ($\gtrsim 200{\rm M}_\odot$). Stars of masses $140 < M_* < 260{\rm M}_\odot$ explode as PISNe, which often produce a lot of metals. Halos that experience such PISN are mostly enriched directly to [Fe/H] $\gtrsim -3$. Stars more massive than 260 $\rm M_\odot$ do not contribute to metal enrichment because they directly collapse into black holes. Models with quite high $M_{\rm max}$ is disfavored because with that parameter there are not enough stars at $-5 \leq$ [Fe/H] $\leq -3$.

Our new metal mixing model makes a long tail at the low-metallicity end. In Fig. 19 we show the MDF comparison between model with and without dZ. For relatively high [Fe/H] ($\gtrsim -4.5$), internal enrichment is the dominant channel for enrichment. The dZ for internally enriched halos are typically $dZ \simeq 0$, and we do not see any large effect. However, when we discuss the number of stars with [Fe/H] $\lesssim -4.5$ the inhomogeneity is important. Since (i) the star-forming region is metal-poorer than the simplest estimate, and (ii) MDF is usually

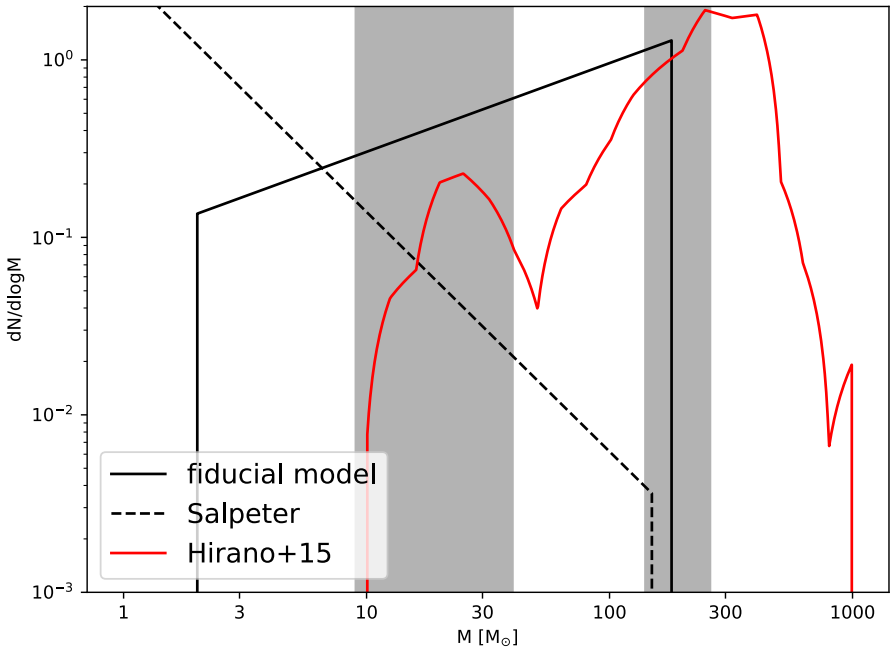


Figure 18: Comparison of Pop III IMF, between A SLOTH calibration and one direct simulation. The black line shows the calibrated primordial IMF. The red line shows the primordial IMF derived by Hirano et al. (2015). The black dashed line is the Salpeter slope to guide the eye. Taking inhomogeneity into account does not modify the IMF prediction. The gray bands are the mass ranges where a lot of metal is ejected.

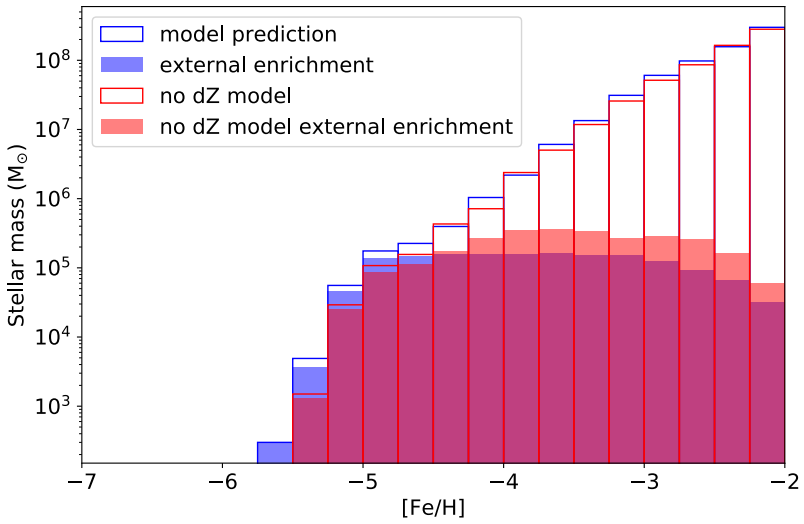


Figure 19: MDF prediction of a tree with the fiducial parameter set. Four histograms are overplotted, but first we explain two of them. The open blue histogram shows the model prediction. The open red histogram also shows the model prediction, but we do not apply dZ. The two histograms are slightly different. Since the KS test is sensitive to the difference of median between two samples, we do not see any difference in the IMF prediction between with and without dZ model. This is because it only slightly changes the overall MDF. Noticable difference can be seen at [Fe/H] $< -4.5$, and in external enrichment. The filled blue histogram shows the MDF only from stars formed by external enrichment. The filled red histogram shows similar to the filled blue one, but we do not apply dZ again. Since the inhomogeneity is larger for external enrichment, [Fe/H] of stars that are formed only from external enrichment are strongly affected by the inhomogeneity. We can see that the filled blue histogram is shifted to low-[Fe/H] end from the filled red histogram. This shifting is caused by the fact that in external enrichment star-forming gas are on average metal-poorer than average of the gas in the halo.

an increasing function at this [Fe/H], the number of stars increases at [Fe/H] $\lesssim -4.5$.

In Fig. 20 we show how the MDF changes with the modification of parameters. Particularly we show the models with different metal ejection mass from Pop III stars:

- Pop III star formation efficiency $\eta_{\rm III}$: $10^{-1}, 10^{-4}$
- Maximum mass of Pop III stars $M_{\rm max}$: $100, 260 {\rm M}_\odot$.

The $\eta_{\rm III} = 10^{-4}$ and the $M_{\rm max} = 100$ models produce less metals at one Pop III star formation event, whereas $\eta_{\rm III} = 10^{-1}$ and the $M_{\rm max} = 260$ models are the opposite. The decrease in Pop III metal mass increases the number of stars at [Fe/H] $\sim -4$, and vice versa. The fiducial parameter is the best to make the MDF compatible with the observation.

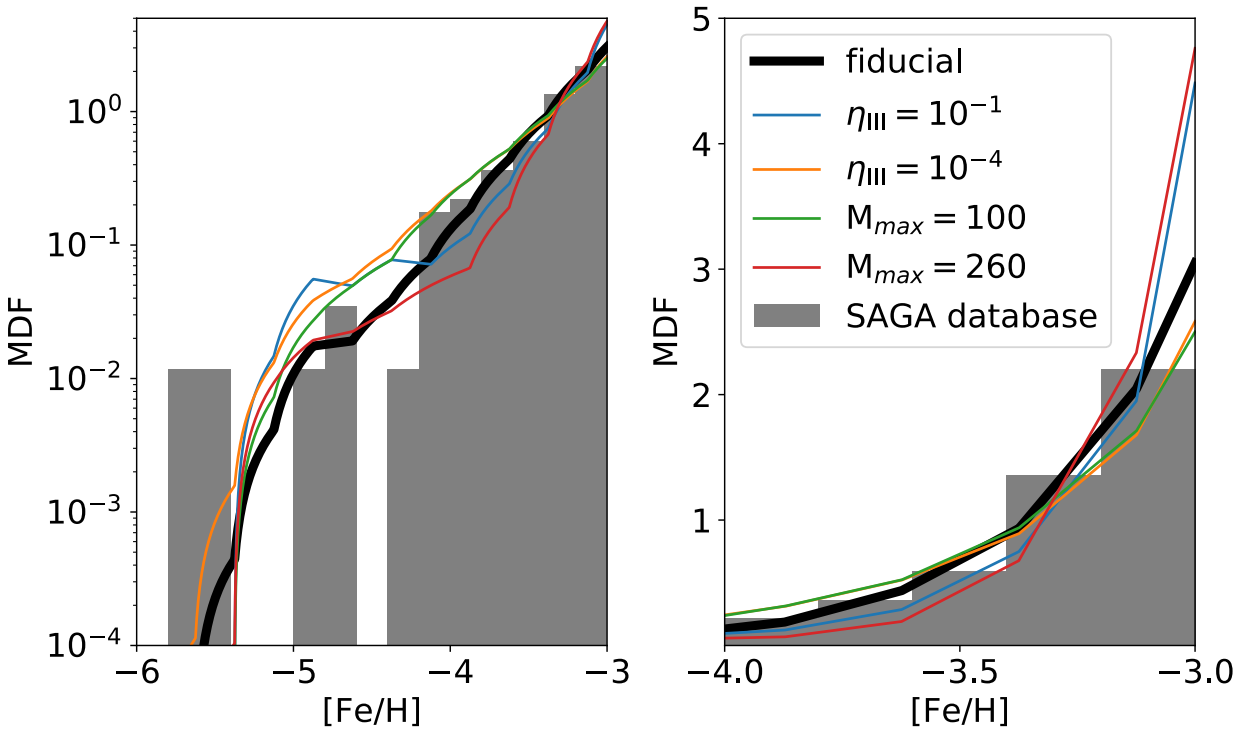


Figure 20: MDF comparison with different parameter sets. The values of the lines on the left and the right panels are the same. The difference is whether the y-axis is in log scale or linear scale, and the range of [Fe/H]. The gray histogram is the observational MDF (Suda et al. 2008). Black curve is the MDF with the fiducial parameter set. The other MDFs obtained by modifying any one of parameters are shown in lines with colors. We can see that A SLOTH forms too many stars in [Fe/H] $< -3.5$ with $M_{\rm max} = 100 {\rm M}_\odot$ and Pop III efficiency $= 10^{-4}$ models. These models tend to produce smaller amount of metals compared to the fiducial parameter set in each Pop III star formation event. After such small metal mass events, stars with quite low [Fe/H] can be formed. The number of stars at [Fe/H] $< -3.5$ is too large to match the observation. IMF maximum $M_{\rm max} = 260 {\rm M}_\odot$ and IMF minimum Pop III efficiency $= 10^{-1}$ are the parameter sets that behaves in the opposite way: they predict too little stars in [Fe/H] $< -3.5$. With these parameters the number of "small metal-mass event" is too small and consequently the number of stars at [Fe/H] $< -3.5$ is not enough to be compatible with the observational MDF.

## 6.2 Stellar mass - halo mass (SMHM) relation

The SMHM relation is a function $M_*(M_h)$. For the low-z galaxies, we can observe the luminosity (erg/s) and stellar velocity dispersion (km/s) or stellar rotational velocity (km/s). The luminosity can be used to estimate the stellar mass of the galaxy assuming mass-to-light ratio is known. The velocity dispersion and rotational velocity can be used to infer the total mass of the system, by virial theorem or rotation-curve fitting. By these methods, in principle we can recover the function $M_*(M_h)$.

In reality, for faint galaxies it is difficult to get velocity information from observation, compared to just getting the luminosity of the galaxy. As a consequence, for some low-luminosity galaxies we only have luminosity information, and we don't know the halo mass. In this case, "Abundance matching method" is often used to infer the halo mass and complete the function $M_*(M_h)$. Within ΛCDM paradigm, once we determine the cosmological parameters $\Omega_\Lambda, \Omega_m(, \Omega_K)$ we can obtain the halo mass function $n(M_h)$ by Press-Schechter theory or N-body simulation. For the details of PS theory, see Press and Schechter (1974). For the luminosity distribution function $n(L)$ we can directly observe. What abundance matching does is to match the heaviest and brightest, match the second, and so on. Since we have both $n(L) \simeq n(M_*)$ and $n(M_h)$, we can obtain the function $M_*(M_h)$.

The SMHM relation is observationally obtained at $z < 6$, but at higher redshift there is no reliable numbers of observation that determines SMHM relation. At higher redshift, the best we can do is the cosmological simulation with (current-best) star formation and stellar feedback scheme. There are some different schemes, and there is about 2 dex of difference in stellar mass among different models. SMHM relation comparison at $z > 6$ cannot be a stringent test, but the star formation we are interested in often happens at around $z \sim 10$, we have compared SMHM from A-SLOTH and the renaissance simulation at $z = 12$.

The SMHM relation is easily accessible in any simulation that forms many stars and galaxy, including the SAM. By matching SMHM, (Pop II) stellar feedback parameters are calibrated.

## 6.3 Internal enrichment fraction

Two channels of Pop III star formation to Pop II star formation transition have been proposed: internal and external enrichment (some reference). The difference is whether the galaxy undergoes a Pop III star formation by itself and then the metals from stars inside enrich the galaxy, changing the star formation mode to the one of Pop II, or the galaxy gets enriched by stars in neighboring galaxies and cannot form metal-free Pop III stars anymore. It is almost impossible to estimate this fraction observationally, because we need to observe the Pop III stars that is still alive, which is unlikely (Mattis paper). However, a bunch of cosmoligical simulations have consistently suggest that the internal enrichment fraction should be around 80% (some reference). We use this internal enrichment fraction to calibrate the Pop III wind velocity and recovery time. It seems the product of the Pop III wind velocity and the recovery time should be around 3000-3500 ($\mathrm{km/s \cdot Myr}$) to reproduce that the internal enrichment fraction is 80% of all the galaxies.

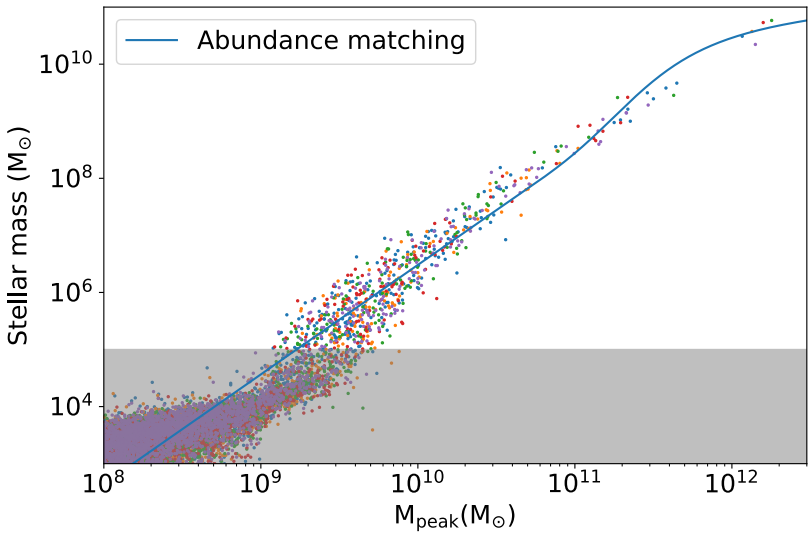


Figure 21: The stellar mass - halo mass relation at present-day. The dots are the galaxies in our model at $z = 0$. Dots of different colors come from different trees. Horizontal axis is the peak halo mass, and the vertical axis is the stellar mass. The solid line is the abundance matching relation by Garrison-Kimmel et al. (2014)

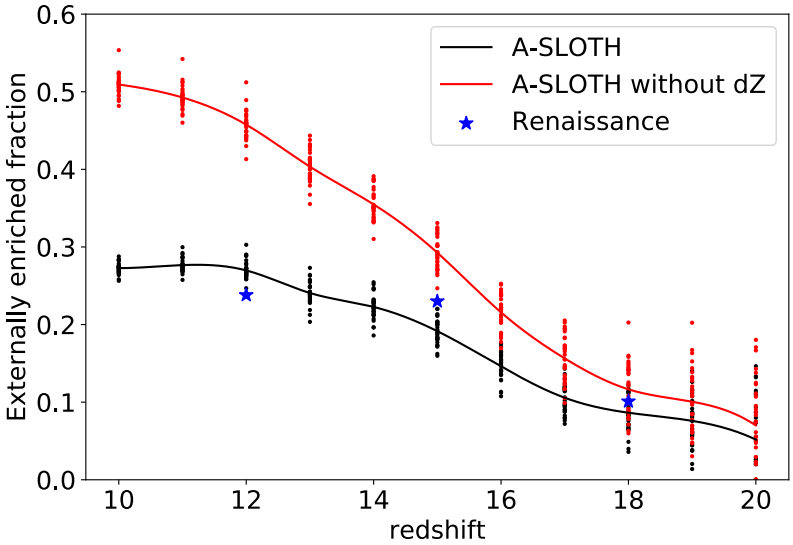


Figure 22: The redshift evolution of externally enriched halo fraction. The blue stars are values in Renaissance simulation at three different redshifts. The snapshots are taken from "Normal" dataset. The black line is the model prediction, and the red line is the model prediction without taking inhomogeneity into account.

### 6.4 Thomson scattering optical depth

The electron-photon scattering at low energy limit is called "Thomson scattering". In the cosmological context, the "Thomson scattering optical depth" $\tau$ is the optical depth that CMB photons experience due to the existence of free electrons in the Universe. The main source of electron is the ionization of hydrogen, so $\tau$ is one probe for ionization history of the Universe. From the cross correlations of different polarizations of CMB, we can measure the optical depth parameter $\tau$. The Planck 2018 results suggest that the $\tau \simeq 0.054$ at $z = 0$ (from the last scattering sufrace). The observational values are actually controversial: Planck 2014 results suggest 0.091 at $z = 0$, and they contradict with each other at $1\sigma$.

Theoretically there remains a huge uncertainty for the optical depth $\tau$, which leaves quite a large freedom in parameters. Optical depth is determined by the fraction of ionized region from $z = 1100$ to $z = 0$, which should be related to Pop III properties like the IMF or the overall Pop III stellar mass via the number of ionizing photons (photons with energy more than 13.6eV and contributes to ionization of the Universe). However, the "escape fraction" that determines the fraction of photons which can escape from the galaxy and contribute to the ionization of the Universe is highly uncertain. If the photons are trapped in the galaxy, it may contribute to the ionization of the H gas inside the galaxy, but since the density is quite high and proton-electron pairs can soon recombine, it does not produce any net effect. The uncertainty in the escape fraction let wide range of parameter space to be possibly consistent. Also, our volume is not enough to be a cosmological representative. Therefore, the optical depth calculated by our code may not match to the observation.

## 7 Discussions and Conclusion

Stellar archaeology is a powerful tool to study the early history of star and galaxy formation. Particularly we take a semi-analytic approach, in which we can test a wide variety of parameters and therefore useful to study the effect of each parameters on observables. With the SAM, each galaxy is represented with one resolution unit: therefore inhomogeneity in each galaxy is often ignored. However, we find that the metallicity distribution of gas inside each galaxy can be highly inhomogeneous: see Fig. 13. Taking the metallicity inhomogeneity into account is important because we use metallicity for the model calibration: wrong metallicity can result in wrong calibrated parameters. We have statistically analyzed the metallicity inhomogeneity inside high-redshift simulated galaxies. We searched for the best method to predict the metallicity difference between star-forming gas and average gas in a halo and define is as a parameter $dZ$. We found that the internal enriched halos and external enriched halos should be treated separately. For internally enriched halos, the inhomogeneity $dZ$ distributes around zero, suggesting that the inhomogeneity is not important and simple estimate of metallicity is enough to predict the metallicity of stars formed in the halo. However, for externally enriched halos, about 40 % of halos have $dZ$ less than -1, i.e. the star-forming gas clouds are more than 10 times metal-poorer than average gas in the halo. There were no other galactic properties that is informative for $dZ$. We simply derived distribution functions both for internally enriched and externally enriched halos.

We further estimated the effect of inhomogeneity on predictions obtained by archaeological approach. Despite the huge metallicity difference in externally enriched halos, it only has

a small effect on the prediction on the Pop III IMF. This is because the Pop III IMF is mainly calibrated by the MDF at [Fe/H] $< -3$, in which internal enrichment is dominant. We expect that our metal inhomogeneity model has a big influence on the various predictions, if it is calibrated by the MDF at [Fe/H] $< -4.5$. In our observational sample there were only six stars that fall in this range. Future observation will increase the number of observed stars in this range. The MDF at this low [Fe/H] can be used to test our inhomogeneous metallicity model.

The inhomogeneity parameter $dZ$ shifts the metallicity of star-forming gas to a lower value than homogeneous model in externally enriched halos. Consequently the externally enriched halo fraction decreases: see Fig. 22. Here we explain why we see this difference. A halo is "externally enriched", if the gas in the halo is enriched to break the relation of Eq. 14. With the parameter $dZ$ that shifts metallicity of dense gas to lower value, it is more difficult to sufficiently enrich the halo by external enrichment. Therefore the probability to have Pop III star formation before the Pop III to Pop II transition by external enrichment increases. This will decrease the externally enriched fraction of halos.

# Part III
# r-process enrichment of UFDs

## 8 Background: r-process

### 8.1 What is the "r-process"?

Currently more than 100 kinds of elements have been known to human, and 92 elements exist on the earth. However, only 3 elements are synthesized in the Big bang, due to the difficulty in 3-body interaction. A natural important question is: when the elements are synthesized, and what process synthesized the elements in the Universe.

Elements lighter than Fe are mainly synthesized in stars. Massive stars produce a lot of $\alpha$ elements (elements with even numbers of protons: they can be synthesized by the accumulation of $\alpha$ particles) through type-II Supernovae(SNe). Smaller stars ($0.6 \sim 8 M_{\odot}$) disperse metals through mass transfer when they are in Asymptotic Giant Branch (AGB) phase. Even smaller stars contribute to element (particularly elements around Fe) synthesis through type-Ia SNe: first the dead star become a white dwarf, and then they explode by merger or mass transfer (still on debate).

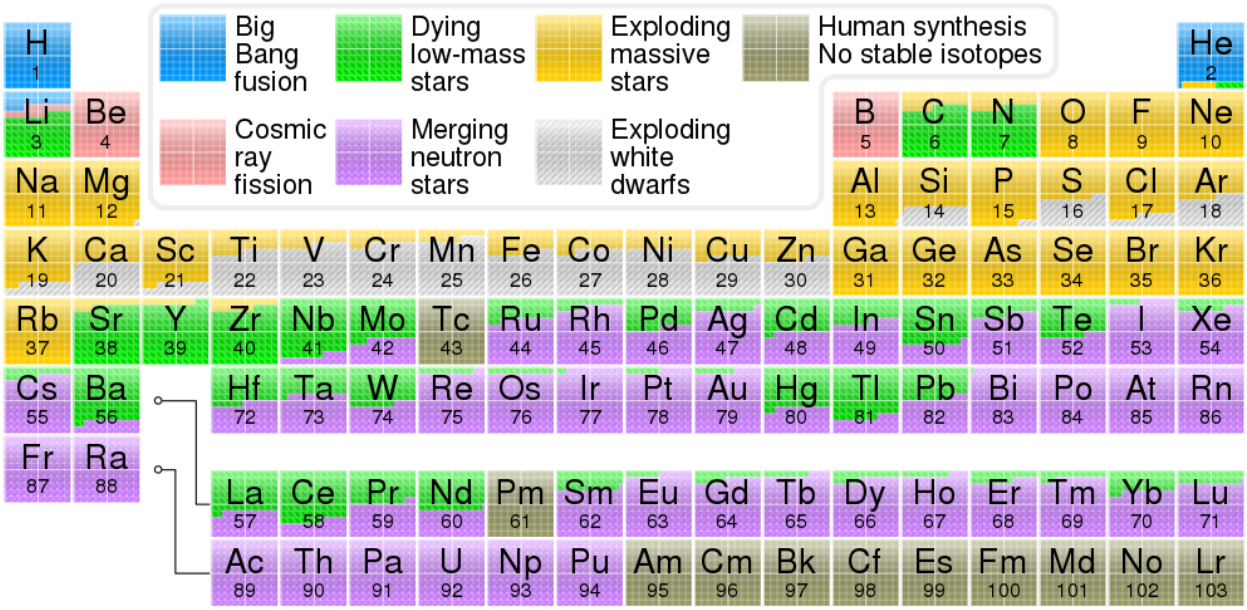


Figure 23: Periodic table colored by their origin. This figure is taken from wikipedia.

However, elements heavier than Fe is difficult to synthesize. Neutron-rich environment is needed to synthesize such heavy elements. Two processes are at play for heavy element synthesis: s(slow)-process and r(rapid)-process. The two processes are distinguished by whether the neutron-capture is occuring faster than the beta-decay of the elements. The difference in the neutron flux results in the different elemental abundance pattern. The origin of the s-process is relatively well-known: AGB stars (Gallino et al. 1998). However, the origin of

the r-process is still under debate. Currently the most promising candidate is a neutron-star merger (NSM). Great improvements in the observational technique let us observe (i) the NSM directly, and (ii) the r-process elemental abundance of stars. We are now on a stage where we can quantitatively discuss the r-process in the Universe.

## 8.2 Physical background

Here we summarize the background physics of the r-process. The discussions are based on the review paper (Cowan et al. 2019).

The Universe begins its history with the Big-Bang. Shortly after the Big-Bang, hydrogen (H, mass number: 1), helium (He, mass number:4), and a trace amount of lithium (Li, mass number:7) are produced. Heavier elements are not synthesized in the Big-Bang. Since the dominant components in the Universe is H or He, elements with mass number $5 = (1 + 4)$, and $8 = (4 + 4)$ can be produced. But they are (unfortunately?) unstable, and the heavy element synthesis halts at He.

For further reactions, a three-body interaction is required. Such interactions are important in a high-density environment. In the Universe, massive stars are the most important place for such reactions. Inside a massive star, triple-alpha reaction:

$$3\alpha \rightarrow^{12} \mathrm{C}$$

proceed. After the formation of carbon, various reactions come into play. Inside heavy stars, elements up to iron (Fe) can be synthesized by nuclear fusion. Among all the elements, Fe is the most stable element in terms of the binding energy per nucleus. Therefore inside heavy stars elements up to Fe can be synthesized. They produce $\alpha$ elements abundantly.

Elements heavier than Fe cannot be synthesized in massive stars. To synthesize such heavy elements, neutrons are important. If the neutron density is high enough, the atomic nuclei can capture the neutron to increase its mass number, and then the neutron decays into proton via $\beta$ decay. The reaction pathway is determined by the competition between the neutron capture rate and the $\beta$ decay rate. If the neutron capture is slower than the $\beta$ decay, the process is called "s-process", and if the neutron capture is faster than the $\beta$ decay, the process is called "r-process". We are mainly discussing the r-process.

### 8.2.1 Nuclear statistical equilibrium (NSE) and quasi-equilibrium (QSE)

Here we explain how we calculate the elemental abundance pattern produced in the r-process. The important ingredients are:

- Cross-section of each reaction,
- temperature, and
- Density of each element.

The equation governing the change of abundance pattern is (eq.1 of Cowan et al. (2019)):

$$\frac{dY_i}{dt} = \sum_j P^i_j \lambda_j Y_j + \sum_{j,k} P^i_{j,k} \frac{\rho}{m_u} \langle j,k \rangle Y_j Y_k + \sum_{j,k,l} P^i_{j,k,l} \frac{\rho^2}{m_u^2} \langle j,k,l \rangle Y_j Y_k Y_l. \tag{36}$$

The terms on the right hand side describe one-body, two-body, and three-body interactions. The factor P's include whether the particles are created or destroyed. The factor $\lambda_j$ is the decay rate, $\langle j,k\rangle$ is the $\langle\sigma v\rangle$ of reactions between nuclei $j,k$. The three-body interaction is acutally a sequence of two-body interactions, with unstable intermediate product. The $Y_i$ represents the abundance of nucleus $i$, and it can be translated to number density via $n_i = \rho Y_i/m_u$. The relevant interactions are:

- Neutron-capture: $n + (Z,A) \leftrightarrow (Z,A+1) + \gamma$, two-body interaction.
- Decay: one-body interaction.
- Photo-disintegration: one-body interaction, assuming photon density follows the black-body spectrum so that we do not treat photons as particles.
- electron, neutrino relevant interactions: one-body interaction, assuming we know the electron or neutrino density and temperature. For neutrinos it is required to calculate radiation transport, as they travel quite a long distance compared to photons or electrons.

In principle, if we know all the reaction cross-sections, we can solve the entire reaction network with thermodynamics and hydrodynamics. In reality, solving the entire reaction network is computationally expensive. What we astrophysicists usually do is first we only include reactions that is important in terms of energy production in hydrodynamics simulation. After having obtained the hydrodynamics solution, we then post-process the detailed reaction network.

When the temperature and density are sufficiently high, we can assume that the reactions are in equilibrium. In this case, we can relate the abundances of nuclei to the chemical potentials of the nuclei. The reactions in equilibrium is for example $p + (Z,A) \leftrightarrow (Z+1, A+1) + \gamma$, or $n + (Z,A) \leftrightarrow (Z,A+1) + \gamma$. The equilibria of these reactions correspond to the relation $\mu_p + \mu(Z,A) = \mu(Z+1,A+1), \mu_n + \mu(Z,A) = \mu(Z,A+1)$. If this relation holds for any nuclei, we can express the chemical potentials of any nuclei only by $\mu_n, \mu_p$, as $\mu(Z,A) = Z\mu_p + (A-Z)\mu_n$. Such condition is called nuclear statistical equilibrium (NSE). If we further assume that each nucleus is in equilibrium with thermal bath, i.e. the number density can be expressed by a Boltzmann distribution, the abundances are completely expressed with the nuclear properties and the physical conditions at time $t$. The actual expression is (taken from eq.2 of Cowan et al. (2019)):

$$Y_i = Y_n^{N_i} Y_p^{Z_i} \frac{G_i(T) A_i^{3/2}}{2^{A_i}} \left(\frac{\rho}{m_u}\right)^{A_i - 1} \times \left(\frac{2\pi\hbar^2}{m_u kT}\right)^{3(A_i-1)/2} \exp\left(\frac{B_i}{kT}\right) \tag{37}$$

$B_i$ is the binding energy of the nucleus, $G_i$ is the partition function of nucleus $i$, and $\rho$ is the density. The point is: **the abundances of elements are completely determined by a small number of conditions**. The conditions are: density $\rho(t)$, temperature $T(t)$, neutron fraction $Y_n(t)$, and proton fraction $Y_p(t)$. The $Y_n, Y_p$ are constrained by total mass

conservation and the electron fraction:

$$Y_n + Y_p + \sum_{i,(A_i>1)} (Z_i + N_i) Y_i(\rho, T, Y_n, Y_p) = 1 \quad (38)$$

$$Y_p + \sum_{i,(Z_i>1)} Z_i Y_i(\rho, T, Y_n, Y_p) = Y_e \quad (39)$$

This $Y_e = \sum Z_i Y_i$ is altered by reactions that are not in equilibrium: namely, $\beta$ decay, electron capture, and charged-current neutrino interactions. We have to solve these interactions explicitly to determine $Y_e(t)$.

Eq. 37 tells us that:

- at high density, heavier nuclei are preferentially formed due to $\rho^{A_i-1}$,
- at high temperature, lighter nuclei are favored due to $(kT)^{3(A_i-1)/2}$,
- in the intermediate regime, Fe-group elements are favored, as the binding energy term is the most important.

It is often the case that some "bottleneck" reaction exists, and not all nuclei are in equilibrium, but only certain regions on the nuclear chart are in equilibrium. This is called "quasi-statistical equilibrium" (QSE). One typical example is among elements at $Z \lesssim 30$. The nuclei are divided into: (i) Fe-group elements, (ii) Si-group elements, (iii) light group up to He, and (iv) the other nuclei that are not in equilibrium. This is important in the Big-Bang nucleosynthesis. The light group can be regarded as in equilibrium, but the formation of nuclei heavier than He is severely suppressed, because $^8$Be is unstable (and there is no element with mass numeber 5). We need quite a high density environment in order for the next synthesis to occur. As a result, the abundance of $\alpha$ particles is higher than the result obtained by assuming a full NSE, whereas the abundances of heavier particles are lower. This is called "$\alpha$-rich freeze out". QSE is also important when we discuss the r-process. In neutron-rich environment, we can ignore protons. Therefore we can assume that the nuclei with the same proton numbers are in quasi-equilibrium. On longer timescales, they experience $\beta^-$-decay to increase their proton numbers.

### 8.2.2 The special features of the r-process

In this section we summarize features specific in r-process. The environment is quite neutron-rich, so that we ignore the protons, consequently we assume that charged-particle reactions are frozen. We also assume that each group of isotopes (which share the same proton number but different mass number within) is in QSE. The only way for nuclei to increase proton number is the $\beta^-$-decay. The neutron density is so high that nuclei with neutron energies $S_n \simeq 2$MeV can be synthesized. Here, the $S_n$ is the energy that is required to pull one neutron out from the nucleus. If this value is less than zero, a neutron "drips" from the nucleus, therefore the half-life of the nucleus will be quite short ($\sim 10^{-20}$s). The line which the $S_n$ becomes zero on is called "neutron-drip line". The r-process path is somewhere between the stable region and the neutron-drip line.

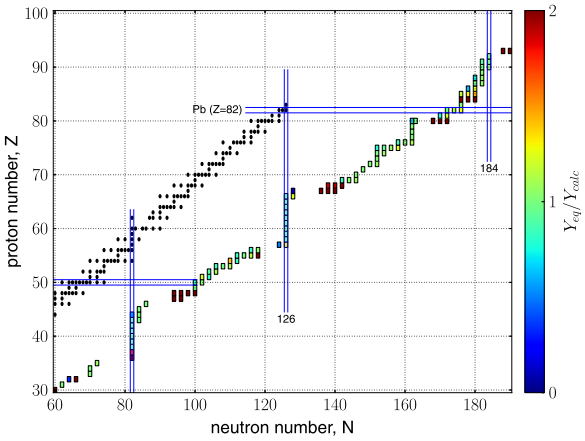


Figure 24: Figure showing the stable region in the Z-N plane and an r-process path. The horizontal axis is the neutron number, and the vertical axis is the proton number. The black dots are the stable nuclei. The colored boxes are the nuclei that are synthesized in r-process. The track of the colored boxes is called "r-process path". This figure is taken from Fig. 7 of Eichler et al. (2015).

We can derive an interesting consequence on the r-process path. Here we assume that the neutron-captures and photodisintegrations occur at very high rates (neutron density $n_n > 10^{20}/\mathrm{cm}^3$, temperature $T > 1\mathrm{GK}$). Consequently we can assume the reactions are in chemical equilibrium. On the nuclear chart, we are assuming that the horizontal line is in QSE. The abundance ratio of two neighboring nuclei is (the eq.4 in Cowan et al. (2019)):

$$\frac{Y(Z,A+1)}{Y(Z,A)} = n_n \frac{G(Z,A+1)}{2G(Z,A)} \left[\frac{A+1}{A}\right]^{3/2} \times \left[\frac{2\pi\hbar^2}{m_u kT}\right]^{3/2} \exp\left(\frac{S_n(A+1)}{kT}\right). \tag{40}$$

In Eq. 40 the right-hand side is mostly determined only by $n_n$, and $T$. On the r-process path the ratio should be almost one for any QSE groups with any proton numbers. Therefore the following statement is justified: **the r-process path almost coincides with the constant-$S_n$ value line**. In Fig. 24 we show the comparison between the elements synthesized in r-process and the stable elements. The r-process path is calculated with $S_n \simeq 2\mathrm{MeV}$. On $N = 50, 82, 126$ there is a vertical line that a wide range of proton number nuclei are allowed to exist. These numbers are called "magic numbers", where nuclei tend to be stable. Here we can understand the difference of peak positions between s- and r-process. In s-process, typically the $\beta$-decay rate is higher than the neutron-capture rate, therefore nuclei synthesized by s-process are almost on the stable region on the nuclear chart. The peaks in the s-process is determined by the stable region and the magic numbers of neutrons. The $N = 50$ peak corresponds to $^{88}$Sr, $N = 82$ corresponds to $^{138}$Ba, and $N = 126$ corresponds to $^{208}$Pb. The peaks in the r-process, however, is determined by the r-process path and the magic numbers of neutrons. The r-process path runs below the stable region by about 10 protons. Therefore, the peaks are shifted to lower-mass end in the r-process than in the s-process by about 10 in mass number and 5 in proton number: $N = 50$ corresponds to elements around $A \simeq 80$, $N = 82$ corresponds to elements around $A \simeq 130$, and $N = 126$ corresponds to elements around $A \simeq 190$.

First r-process simulations assume $(n, \gamma)$ and $(\gamma, n)$, namely neutron-capture and photo-disintegration are in equilibrium. This is a good approximation if the temperature is high enough. Theorists assume neutron densities, temperatures, and the durations of r-process to derive abundance patterns in various conditions, but they failed to find the pattern that matches the Solar r-process abundance. Later it is recognized that not only the "hot" r-process but also "cold" r-process, in which $(n, \gamma)$ and $(\gamma, n)$ are not in equilibrium, is important in astrophysical environments.

In the later stages of r-process, the number of free neutrons become small, so that neutron-capture rate becomes comparable or lower than $\beta$-decay rate. The evolution after this moment is called r-process freeze-out. This is quite different between s-process and r-process. In s-process, $\beta$-decay is faster than the neutron-capture throughout the nucleosynthesis. In r-process, the winner reverses in the middle. This reverse makes a difference in the elemental abundance pattern. the abundance pattern of r-process is smoother than the one of s-process.

## 8.3 Astrophysical r-process origin

The origin of r-process in the Universe has long been a huge mystery, and many theoretical models try to explain observed r-process elemental abundances. In previous section we summarize the condition required for r-process. The important condition is: neutron-richness. Historically the first astrophysical phenomena that drew attention was the CCSNe. However, in current understanding of SNe mechanism neutrino is abundantly produced. Neutrinos can convert a neutron to proton via

$$\nu_e + n \leftrightarrow p + e^-. \tag{41}$$

Therefore the regular CCSNe are not likely the r-process origin. We will discuss various possible sites of r-process.

### 8.3.1 Neutrino winds from CCSNe

The most promising scenario for the explosion is the "neutrino delayed explosion mechanism". A hot proto-neutron star is formed in the center of a dying massive star. When the proto-neutron star enters the Kelvin-Helmholtz cooling phase, it emits neutrinos of all flavors. These neutrinos convey energy to outer envelope of the dying massive star, therefore an explosion occurs. In this scenario, $\nu_e, \bar{\nu}_e$ are produced abundantly, therefore through the reactions in Eq. 41 and

$$\bar{\nu_e} + p \leftrightarrow n + e^+. \tag{42}$$

the abundance of $n$ and $p$ is determined only by the $\nu_e, \bar{\nu}_e$ fluxes. The $Y_e$ is calculated as:

$$Y_e = \left[1 + \frac{L_{\bar{\nu_e}} W_{\bar{\nu_e}}}{L_{\nu_e} W_{\nu_e}} \times \frac{\epsilon_{\bar{\nu_e}} - 2\Delta + \Delta^2/\langle E_{\bar{\nu_e}}\rangle}{\epsilon_{\nu_e} + 2\Delta + \Delta^2/\langle E_{\nu_e}\rangle}\right]^{-1}. \tag{43}$$

Here the $L_{\nu_e}, L_{\bar{\nu_e}}$ are the neutrino and antineutrino luminosities, $W_{\nu_e} \simeq 1{+}1.01\langle E_{\nu_e}\rangle/(m_n c^2), W_{\bar{\nu_e}} \simeq 1{-}7.22\langle E_{\bar{\nu_e}}\rangle/(m_n c^2)$ are the weak-magnetism corrections, $\epsilon_{\bar{\nu}} = \langle E^2_{\nu_e}\rangle/\langle E_{\nu_e}\rangle, \epsilon_{\bar{\nu_e}} = \langle E^2_{\bar{\nu_e}}\rangle/\langle E_{\bar{\nu_e}}\rangle$ is the ratio between second moment and first moment of neutrino and antineutrino spectra, and $\Delta = 1.2933$MeV is the mass difference between a neutron and a proton. Under the assumption that Eqs. 41, 42, the condition to make neutron-rich is the high luminosity of $\bar{\nu}_e$

compared to the luminosity of $\nu_e$. With this condition, the Eq. 42 is biased to the right-hand side and the Eq. 41 is biased to the left-hand side, therefore $Y_e$ decreases.

In general, the neutrino emission in CCSNe and the one in NSM are different. In CCSNe, the neutrino emission is mainly from the central hot neutron-star. Since the neutrino is the leftover of "de-leptonization", the flux is higher from $\nu_e$ than from $\bar{\nu}_e$. In order for the neutrino-driven winds to be neutron-rich, the $\epsilon_\nu - \epsilon_{\bar{\nu}}$ should be larger than $4\Delta \simeq 5.2$MeV. Detailed calculations shows that this value is unreachable in this system. In NSM, the system is already neutron-rich in the first place. When the moment of two neutron stars merge, the system is heated to high temperature, leading to protonization. This protonization produces the energy and flux difference between $\bar{\nu}_e$ and $\nu_e$: in this case the system is neutron-rich, enough to allow weak r-process. Note that this is the discussion on the late ejecta: the early ejecta, which emerges from the spiral arms after the merger, is very neutron-rich. Therefore such dynamical ejecta is responsible for the strong r-process in NSM.

### 8.3.2 Other candidates

I will discuss each candidate model in turn.

1. Regular CCSNe. When a massive star dies, it can form a neutron-star in the center (depending on the progenitor mass). The baryon components around the central neutron-star should be neutron-rich, because the physical condition is similar and components should also be similar. The remaining problem is to explain how the neutrons in the center ejected to lower-density environment and allow r-process. This is actually difficult. The simulations of SNe suggest that the stellar explosion is driven by the energy transport mediated by neutrinos. Detailed calculation showed that in most cases the ejecta would rather be proton-rich. In such a condition (called $\nu p$-process) neutron deficient elements, auch as $^{92}$Mo are synthesized.

2. Electron-capture SNe. The problem in the regular CCSNe scenario is the existence of strong neutrino radiation. In this scenario the matters are ejected promptly so that the ejecta is not affected by the neutrino radiation. In this scenario weak r-process can be expected (Mirizzi et al. 2016).

3. Magneto-rotational SNe (MRSNe). In this scenario the explosion is caused by magnetic field pressure (and also the neutrino-wind, depending on the physical conditions). The calculations have been expensive, but recently a high resolution-simulation that resolves the magneto-rotational instability (MRI) that is essential for the strong magnetic field (Nishimura et al. 2017a). The simulation showed that in certain conditions it is possible. The initial conditions of the progenitor stars are still unknown. Particularly the strength of the magnetic field and the rotation are important. The MRSNe produce a wide variety of abundance pattern, depending on these parameters. In Fig. 27 we show the comparison of elemental abundance patterns in parameter sets. The "m-model", "i-model", and "h-model" are the models which differ in neutrino luminosity from the central neutron star. In the "m-model" the magnetic field pressure is dominant compared to neutrino flux, and in the "h-model" the neutrino heating is dominant, and the "i-model" is the intermediate model between the m- and h- models. In Fig. 28 we

show the effect of the different parameters on the r-process yield. In the "m-model", $M_{\rm Eu} \simeq 10^{-5}{\rm M}_\odot$ is produced. This is comparable to the amount of Eu produced in one NSM. In the "i-model", the amount of Eu synthesized can be about one dex less than the values in "m-model".

4. Collapsars. In this scenario neutron excess required for r-process is realized at the inner region of accretion disk around a black hole formed in the center of the collapsing star. When the gas becomes sufficiently dense, protons capture electrons and make neutron excess. The r-process elements are ejected by a jet perpendicular to the accretion disk.

   Here we breifly show how the neutron-rich environment appears. Assuming that the electron and positron are in equilibrium with photons, the number densities can be expressed as:

$$n_\pm = \frac{(m_e c^2)}{\pi^2 \hbar^3} \int_0^\infty f_\pm \left( \sqrt{p^2+1} \right) p^2 dp \tag{44}$$

   where $p$ is a momentum of the particle in units of $m_e c$, and $f_\pm$ is the Fermi-Dirac distribution function, namely

$$f_\pm = \frac{1}{\exp[(x \pm \mu)/\theta]} \tag{45}$$

   where $\theta = kT/m_e c^2$. Note that the equilibrium with photons produced the condition: $\mu_+ + \mu_- = 0$ and is already used in Eq. 45. The $Y_e$ is also constrained by charge neutrality:

$$n_- - n_+ = Y_e \frac{\rho}{m_e}. \tag{46}$$

   Substituting Eq. 45 into Eq. 44 $n_\pm$ can both be described by one variable, $\mu(T)$. If we give temperature $T$, density $\rho$, and electron fraction $Y_e$, then we can obtain $\mu(T)$. Since the electrons are fermions, they will be degenerate if the density is high and the temperature is (relatively) low. Let me estimate the condition of electron degeneracy. Suppose an electron is confined in a box with $L \times L \times L$. The temperature is high, so that the electron is relativistic. The number of states with wavenunber less than $k$ is $N(k) = \frac{L^3}{6\pi^2} k^3$. Energy $E$ and wavenumber $k$ is related to each other by $E^2 - m_e^2 c^4 = c^2 \hbar^2 k^2$. Therefore the number density of states up to energy $E$ can be expressed as:

$$n = \frac{k^3}{6\pi^2} = \frac{1}{6\pi^2} \frac{\left(E^2 - m_e^2 c^4\right)^{3/2}}{c^3 \hbar^3}. \tag{47}$$

   Considering the electrons have spin 1/2, the fermi energy $E_F$ is connected to electron density $n_e$ as:

$$n_e = \frac{1}{3\pi^2} \frac{\left(E_F^2 - m_e^2 c^4\right)^{3/2}}{c^3 \hbar^3}. \tag{48}$$

   Electrons are degenerate, if the typical thermal energy $kT$ is less than the fermi energy. Therefore the condition is (assuming $E_F >> m_e$):

$$\begin{aligned} kT &= E_F & (49)\\ &= (3\pi^2 c^3 \hbar^3)^{1/3} (n_e)^{1/3} & (50)\\ &= 2.8 \times \left( \frac{\rho}{10^{11} {\rm g \cdot cm^{-3}}} \right)^{1/3} {\rm MeV}. & (51) \end{aligned}$$

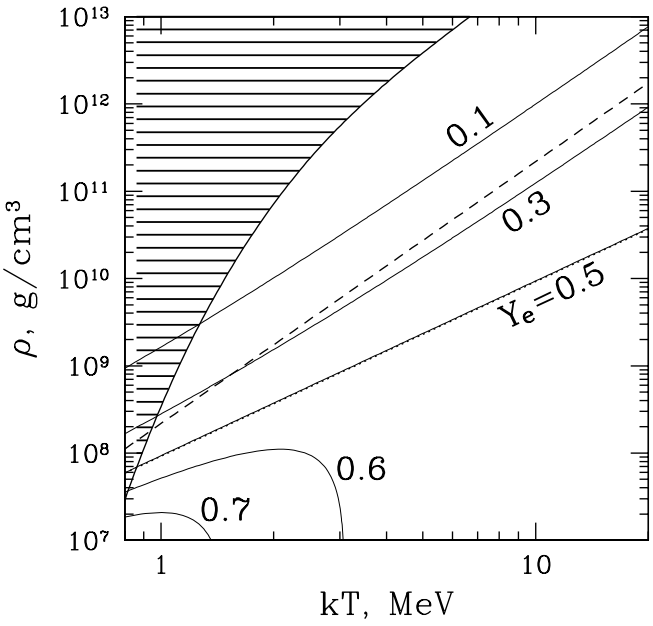


Figure 25: This figure shows the relation between $Y_e$ and $\rho, T$. The $Y_e$ on $\rho - T$ plane is determined by Eqs. 46, and 55. The shaded region is where the calculations are not valid since baryons are dominated by composite nuclei. The dashed line shows the boundary of electron degeneracy. This figure is taken from Fig.1 of Beloborodov (2003).

If there are abundant electrons and positrons, the reaction below proceeds:

$$e^- + p \to n + \nu, e^+ + n \to p + \bar{\nu}. \tag{52}$$

These reactions quickly adjust the $n_\pm$ to the equilibrium $Y_e(T, \rho)$. The condition is different whether the neutrino backreaction is important or not. To proceed further, we need to consider neutrino reactions. Here we only review the $\nu$-transparent case, i.e. we ignore the neutrino-absorbing reactions. The rates of $e^-, e^+$ captures can be calculated with the electroweak theory. Assuming that the nucleons are not degenerate, the capture rates are:

$$\dot{n}_{e^-p} = Kn_p \int_0^\infty f_-(\omega + Q)(\omega + Q)^2 \left[1 - \frac{1}{(\omega + Q)^2}\right]^{1/2} \omega^2 d\omega \tag{53}$$

$$\dot{n}_{e^+p} = Kn_p \int_{Q+1}^\infty f_+(\omega - Q)(\omega - Q)^2 \left[1 - \frac{1}{(\omega - Q)^2}\right]^{1/2} \omega^2 d\omega. \tag{54}$$

where $\omega$ is the neutrino energy in units of $m_e c^2, Q = (m_n - m_p)/m_e = 2.531$, and $K = 6.5 \times 10^{-4} \mathrm{s}^{-1}$. If the system is in equilibrium, we can impose additional equation:

$$\dot{n}_{e^-p} = \dot{n}_{e^+p}. \tag{55}$$

This equation finally let us determine $Y_e$ for a given set of $\rho, T$. In Fig. 25 we show the figure taken from Beloborodov (2003). The solid lines are the $Y_e$ contours calculated by assuming the $\nu$-transparancy.

We are discussing a bit more detail into the condition for neutron-excess. The transition from $Y_e > 0.5$ to $Y_e < 0.5$ occurs at a mild degeneracy, $\mu < \theta$. At $\mu < \theta$ and $\theta > Q + 1$,

$$\dot{n}_{e^-p} = Kn_p\left[\frac{45}{2}\zeta(5) + \frac{7\pi^4}{60}\frac{(2\mu - Q)}{\theta}\right] \quad (56)$$

$$\dot{n}_{e^+p} = Kn_p\left[\frac{45}{2}\zeta(5) - \frac{7\pi^4}{60}\frac{(2\mu - Q)}{\theta}\right]. \quad (57)$$

Here we neglect the higher-order terms, such as $O(Q^2/\theta^2), O(\mu^2/\theta^2)$, and $O[(Q+1)^5/\theta^5]$. The equation between the two time derivatives yields:

$$Y_e = \frac{1}{2} + \frac{7\pi^4}{1350\zeta(5)}\frac{(Q/2 - \mu)}{\theta} = \frac{1}{2} + 0.487\frac{(Q/2 - \mu)}{\theta}. \quad (58)$$

Now the neutron-excess region on the $T - \rho$ plane can be expressed as $\theta < \theta_n(\rho)$, where

$$\theta_n = \left(\frac{3\lambda\!\!\!^{-3}\rho}{Qm_p}\right)^{1/2}, kT_n = 33\rho_{11}^{1/2}\mathrm{MeV} \quad (59)$$

The relation between $kT_n, \rho$ is exactly the line of $Y_e = 0.5$ in Fig. 25. It is instructive to express the $n_\pm$ with $\mu$ using Taylor expansion to the first order of $\mu$. The results is:

$$n_\pm = \frac{1}{\pi^2\lambda\!\!\!^{-3}}\left[\frac{3}{2}\zeta(3)\theta^3 \mp \frac{\pi^2}{6}\mu\theta^2\right], \mu < \theta \quad (60)$$

With the definition of $Y_e$, $\mu$ can be expressed as:

$$\mu = 3Y_e\frac{\lambda\!\!\!^{-3}\rho}{m_p\theta^2} \quad (61)$$

The sound speed in a gravitationally bound object cannot exceed the gravitational potential. This relation can be expressed as:

$$\frac{P}{\rho} \lesssim 0.1c^2\left(\frac{r}{3r_g}\right)^{-1} \quad (62)$$

The pressure includes radiation, $e^\pm$, neutrinos, and baryons. The first three components are relativistic particles, and their contributions can be put together as $aT^4$, where $a = (\pi^2k^4/15\hbar^3c^3)$. Therefore the overall pressure can be expressed as

$$P \simeq aT^4 + \frac{\rho}{m_p}kT. \quad (63)$$

The ratio of two terms is:

$$\frac{aT^4}{(\rho/m_p)kT} = \frac{\pi^2}{15}\frac{\theta^3}{\theta_{\rm deg}} \quad (64)$$

The radiation pressure is dominant if $\theta \gtrsim \theta_{\rm deg}$. We just consider this case and let $P \sim aT^4$. Then the Eq. 62 becomes

$$\frac{\theta}{\theta_{\rm deg}} \lesssim 2\rho_{11}^{-1/12}\left(\frac{r}{3r_g}\right)^{-1/4}. \quad (65)$$

In Eq. 61 we show the relation between $\mu$ and $T$. With this equation, we can have the condition from Eq. 65:

$$\frac{\mu}{Q} \gtrsim 5 Y_e \rho_{11}^{1/2} \left( \frac{r}{3r_g} \right)^{1/2}. \tag{66}$$

The object is neutron-rich if $\mu > Q/2$. This is satisfied if

$$\rho \gtrsim 10^{10} \left( \frac{r}{3r_g} \right)^{-1} \text{g cm}^{-3}. \tag{67}$$

Therefore, **any matter that satisfies Eq. 67 can be the source of neutron-capture elements.**

In order to show that the collapsar actually produce r-process elements, we have to calculate the density and temperature. The electron-captures by protons occur at the inner side of the accretion disk. Therefore we estimate the $\rho, T$ of the accretion disk.

Collapsars are associated with hypernovae, which are energetic by about 10 times more than usual SNe. Interestingly, there was a very energetic SN event at 1998. The event was classified as Type Ic SN, and was linked to a long-duration gamma-ray burst. The $^{56}$Ni production and the explosion energy were estimated to be 0.5 $M_\odot$ and $3 \times 10^{52}$ erg. The large amount of $^{56}$Ni production is representing that there should exist a region where $Y_e \simeq 0.5$.

In this event r-process elements can be synthesized within certain model parameters.

5. NSM. Since neutron-stars are (by definition) neutron-rich, it is natural to consider the possibility of r-process in the NSMs. Here we summarize the observational status. Neutron stars are observed as pulsars. Humans have already observed many pulsars, enough to draw the mass distribution. Also some binaries are observed (Hulse and Taylor 1975). The orbital energy loss (estimated by the change in the rotation period) is consistent with the gravitational-wave emission (Weisberg and Huang 2016).

   Here we follow the time evolution of NSM. A neutron-star is formed as the leftover of a SN. The formation of a binary neutron-stars is still under debate, but the most widely accepted model is the "common-envelope". Initially there is a massive stellar binary. The first star explode, and leave a NS. Then the envelope of the second star inflates just before the explosion (when it used up the central hydrogen), and swallows the NS. While the two stars share the common envelope, the orbital separation gets smaller and smaller by dynamical friction. This phase decreases the NS-NS separation. The separation should be small, otherwise the BNS cannot merge within the age of the Universe. Soon the second SN happen. The SN can have anisotropy, which easily lead to a few 100 km/s of kick velocity $v$ on the second NS. This is the origin of the kick on the BNS: $v/2$ (if the two NS have the same masses) will be the kick velocity of the BNS. This common-envelope scenario is the best to explain the fast-merging BNS we need to explain the chemical evolution, but this is far from perfect. Other models such as dynamical capture of two neutron-stars (reference) are still considered.

   After the explosion of the second star, the separation of the BNS gets smaller and smaller by the energy loss of gravitational wave emission. The orbits can be highly

eccentric, but the eccentricity quickly decreases when they in-spiral. The time duration between the BNS formation and the merger is called "delay-time", and its distribution is called "delay-time distribution" (DTD). The DTD is highly uncertain, as the knowledge on the distribution of initial separation is quite limited. The slope of the DTD is relatively well-constrained to $dN/dt \propto t^{-1}$. Often we assume $t_{\rm min} \simeq 10$Myr and $t_{\rm max} \simeq 10$Gyr when we model the BNS formation in the Universe. The $t_{\rm max}$ is not so important, because the slope of the DTD is negative. This is just degenerate with the BNS formation rate.

Just before the merger, we can assume that the orbit is almost circular. With this simple situation numerical simulation is an effective way to model the merger. The two neutron stars are deformed by the tidal force and centrifugal force, and finally some of the neutrons are ejected on the equatorial plane that the BNS rotates. This ejecta is called "cold dynamical ejecta". The particles are cold, and quite neutron-rich, therefore this is the origin of strong r-process in NSM. The amount of cold dynamical ejecta depends on the mass ratio of the binary. Smaller mass ratio results in larger amount of cold dynamical ejecta, but if the mass ratio is too small ($\lesssim 0.1$), the smaller one is just swallowed into the massive one, and no cold dynamical ejecta comes out. The amount of cold dynamical ejecta also depends on the compactness of the neutron stars. This information is not observable. If the amount of cold dynamical ejecta from a NSM with well-known mass ratio is determined precisely, we can have the information on the size of a neutron star. This helps nuclear theorists to find the equation of states (EoS) in neutron stars. Therefore, the detailed modeling (on mergers and on galactic chemical evolution) to determine the mass of cold dynamical ejecta is quite important. At the moment of the merger, a shock propagates from the contact surface. The ejected components are heated by the shock, gets hotter, and ejected by the thermal pressure. The electron-positron pairs produced in the high temperature make the initially low $Y_e$ to increase. The $Y_e$ further increases if the central remnant if a NS and neutrino wind comes out. This "hot dynamical ejecta" has $Y_e \simeq 0.5$ and is ejected to polar directions.

After the merger, still mass ejection continues. The notable components are "neutrino-wind component", and "accretion-disk outflow". Here we explain these in turn. The neutrino-wind component is similar to the case of CCSNe. Typically, the merger remnant will first exist as a hot NS, supported by high temperatures and rotation. The difference from CCSNe case is the anisotropy: the central NS is surrounded by a hot and dense torus, and the neutrino-driven wind occurs mainly in the polar direction. The ejected matter reach an equilibrium between $\nu, \bar{\nu}$ absorption reaction. The resulting $Y_e$ is determined by the spectra of $\nu, \bar{\nu}$, which lead to $Y_e \gtrsim 0.25$ in this case. This mild neutron-richness leads to a weak r-process, where lighter (typically up to second peak) r-process elements are synthesized. The accretion-disk outflow occurs $1 \sim 10$ seconds after the merger. This is an outflow from the accretion disk around the central remnant. The disk is heated by viscosity and nuclear recombination, therefore the outflow occurs thermally. The component of the outflow depends strongly on what the remnant will be: specifically on the lifetime of the massive neutron-star. If the MNS lives longer than one second, neutrino from the MNS significantly increases the $Y_e$ of the disk to $\sim 0.3$. On the other hand, if the MNS collapses to a BH within one second,

the $Y_e$ remains quite low, comparable to the dynamical ejecta.

### 8.3.3 Kilonova observation

A gravitational wave event GW170817 is the first detection of a NSM. This event was also observed electromagnetically. Since the injected energy is comparable to a SN, it behaves somewhat similar way. Both in NSM and SN the energy source is radioactive decay of some elements. By the fitting of the light curve r-process is confirmed. We also have the information on the amount of ejected material and its component. At present some NSM has been confirmed with gravitational wave, but still GW170817 is the only event with confirmed electromagnetic counterpart. Here we summarize the physics around the NSM and the light curve.

The shape of the light curve is determined by (i) radioactive heating, (ii) thermalization efficiency, and (iii) opacity. We explain each in turn.

- Radioactive heating. Within the first $\sim 10$ seconds after the merger, nucleosynthesis proceeds on the r-process path. In case of strong r-process ($Y_e \lesssim 0.2$), a wide variety of elements are synthesized, and the light curve follows a power-law. In case of weak r-process ($Y_e \gtrsim 0.4$), the light curve looks a bit more bumpy, as a result of fewer kinds of elements contribution. The contributing element is different depending on which timescale we focus on. The first few hours neutron decay is the dominant energy source. The free neutrons are on the surface layer of the ejecta, therefore they are bright in UV/blue bands. At $10 \sim 100$ days later, the energy sources are only a few kinds of elements. The dominant reaction of heating is still not well-known. If the $Y_e$ is high, lighter elements are preferred, and the heating is dominated by $\beta$-decay. If the $Y_e$ is low, heavier elements are also synthesized, and the heating is dominated by $\alpha$-decay and nuclear fission.

- Thermalization efficiency. Initially the ejecta is quite dense, and the energy input by radioactive elements are completely thermalized (therefore light curve is affected by the radioactive heating). However, as the ejecta expands, density gets lower and the energy escape fraction increases. Then the energy injected by the radioactive decay is not converted to thermal energy. To take this effect into account, light curve modeling usually contain a time-dependent parameter "thermalization efficiency". This parameter depends on various physical conditions, such as the mass and velocity of the ejecta, magnetic field, and the geometry of the ejecta. The thermalization efficiency of $\gamma$-ray drops rapidly and at a few tens of days their contribution is negligible. The thermalization efficiency of charged particle remains larger, and they are the dominant heat source at late times. This difference makes $\alpha$-decay and nuclear fission more important to shape the later phase of the light curve.

- Atomic opacities. Right after the merger, the ejecta is extremely dense. It is dense enough to capture the photons produced inside the ejecta: therefore, initially we only see the emission from the surface, which is not luminous. At later phases, in which the opacity decreases and the emission from inside can also be observed, the luminosity peaks. The timescale for the clearing-up can be calculated with the photon diffusion

timescale. Assuming that the ejecta expands spherically with a constant speed $v$. Then the diffusion timescale is:

$$t_{\rm diff} = \frac{\rho\kappa R^2}{3c} \tag{68}$$

with $\rho = 3M/(4\pi R^3)$ is the density and $\kappa$ is the opacity of the ejecta. The luminosity peaks when this $t_{\rm diff}$ is comparable to the dynamical timescale, $t = R/v$. Comparing the two timescales, the luminosity peaks at:

$$t_{\rm peak} \simeq \left(\frac{\kappa M}{4\pi c v}\right)^{1/2} \tag{69}$$

$$\simeq 1.5{\rm days}\left(\frac{M}{0.01{\rm M}_\odot}\right)^{1/2}\left(\frac{v}{0.1c}\right)^{1/2}\left(\frac{\kappa}{1{\rm cm}^2{\rm g}^{-1}}\right)^{1/2} \tag{70}$$

After reaching the peak, the luminosity can be approximated by "Arnett's law": $L(t) = M\dot{Q}(t)$, where $\dot{Q}(t)$ is the energy deposition rate. This should already be corrected by the energy thermalization efficiency. This $\dot{Q}(t)$ can be approximated as $\dot{Q}(t) \simeq \epsilon \times 10^{10}(t/1{\rm day})^{-\alpha}{\rm erg\ s^{-1}\ g^{-1}}$, where $\epsilon$ is the thermalization efficiency. The peak luminosity is:

$$L_{\rm peak} \simeq 1.1\epsilon \times 10^{41}{\rm erg\ s^{-1}}\left(\frac{M}{0.01{\rm M}_\odot}\right)^{1-\alpha/2}\left(\frac{v}{0.1c}\right)^{\alpha/2}\left(\frac{\kappa}{1{\rm cm}^2{\rm g}^{-1}}\right)^{-\alpha/2} \tag{71}$$

It is clear that opacity $\kappa$ plays an important role. The value of $\kappa$ depends on the component of the ejecta. Lanthanides, which has open f-shell, is optically thick because they have complex energy level structures from the transitions between different f-shell energy levels. If the ejecta do not contain lanthanides, $\kappa \lesssim 1{\rm cm}^2\ {\rm g}^{-1}$. With this opacity the luminosity should peak at $\sim 1$ day, consistent to the GW170817 observation. If the ejecta do contain lanthanides (and/or actinides), $\kappa \gtrsim 10{\rm cm}^2\ {\rm g}^{-1}$. Often the light curve is fitted with multiple components. The observation favors two or three components, which are low-$\kappa$ and high-$\kappa$ component. This is consistent to the numerical simulation result that the ejecta contains multiple component with different $Y_e$.

In Fig. 26 we show the light curves in eight different wavebands. Basically the simulation well explains the observed datapoints. The light curve is modeled with two components, one with high-$\kappa$ ("red component") and the other with low-$\kappa$ ("blue component").

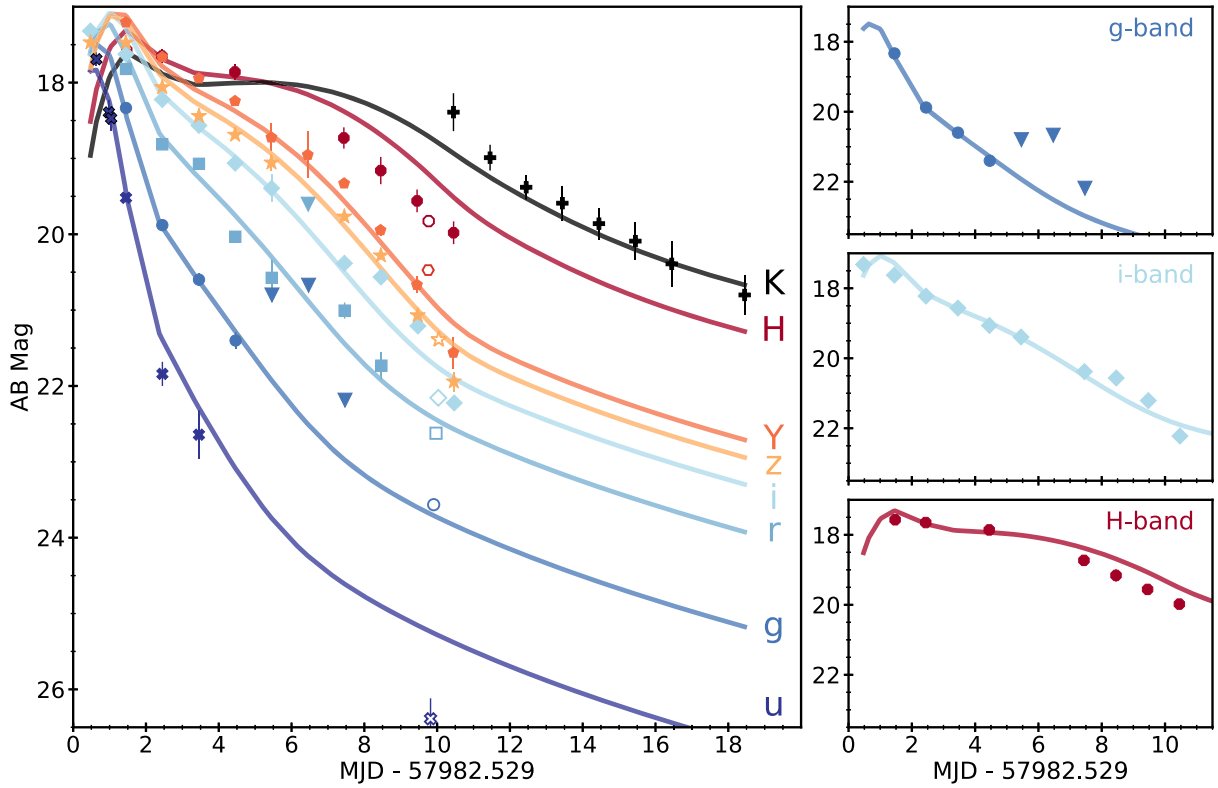


Figure 26: A figure shows the luminosities in various wavebands in the first ten days. Solid lines are the model predictions from their two-component model. The points and bars are showing the observation and its error. The triangles are upper limits with $3\sigma$. Bluer bands peak earlier and redder bands follow later. This figure is taken from Fig. 1 of Cowperthwaite et al. (2017).

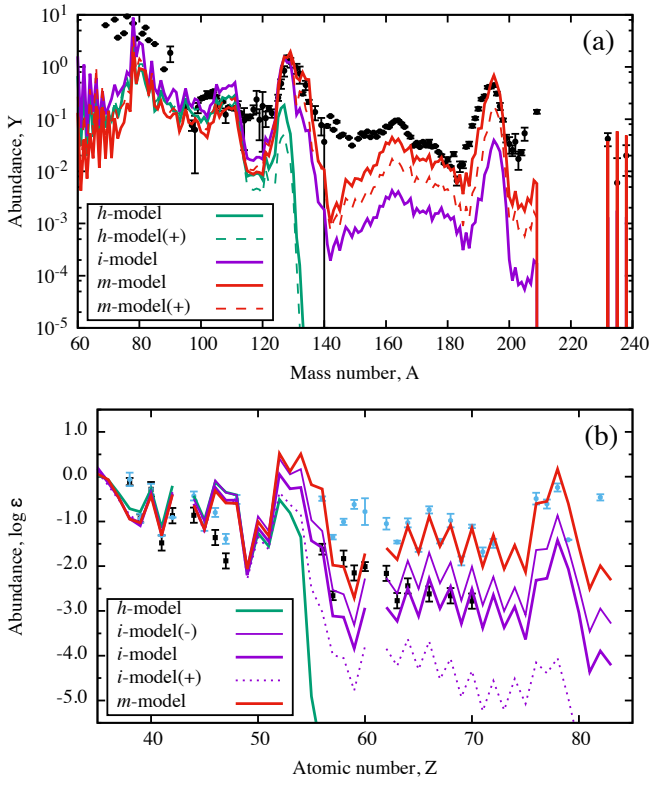


Figure 27: A figure that shows the overall abundance pattern in their various models. The "m-model" matches well with the Solar r-process abundance pattern. The "i-model" matches well only up to the second peak, and the abundances of heavier elements are lower than the Solar value. The "h-model" only matches up to the first peak. This figure is taken from Fig. 4 of Nishimura et al. (2017a).

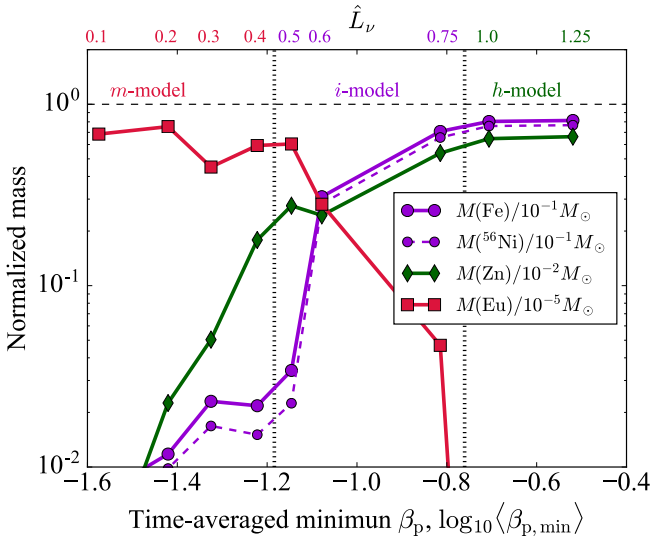


Figure 28: A figure shows the ejecta masses of a MRSN, with different $\beta_p$. The horizontal parameter represents whether the explosion is dominantly caused by magnetic field pressure or neutrino-driven wind: on the left-hand side the magnetic field pressure is dominant, and on the right-hand side the magnetic field effect is not important. With some reasonable parameter sets a MRSN can synthesize neutron-rich elements through r-process. This figure is taken from Fig. 5 of Nishimura et al. (2017a).

# 9 r-process in astrophysics

Humans can observe the sky and get various information. Here I summarize such information which is relevant to r-process.

## 9.1 Eu abundance evolution of MW stars

Recently we can observe numerous elements by conducting high dispersion spectroscopy even at wavelength close to UV. For r-process, the important elements are europium (Eu, for example 4130Å), barium (Ba, for example 4131, 4554Å) and strontium (Sr, for example 4078, 4216Å). Eu is produced (almost) only by r-process, but Ba and Sr can also be produced by s-process. Using only Eu is the most clean way of analyzing, but Ba and Sr are easier to detect, and actually for some stars only Ba and Sr are detected, whereas Eu abundance is below detection limit. The origin of s-process is the AGB stars. Since they are the last moment of low-mass (typically the initial mass of $0.6 \sim 8$ $M_\odot$) stars, there exists a long time-lag between the formation of stars and their contribution to s-process. In terms of chemical evolution, the time delay means they only contribute to metal-rich stars. Therefore it is often assumed that for stars with [Fe/H] $< -2.5$ the contribution from s-process is not prominent.

In Fig. 29 we show the MW stellar [Eu/Fe] - [Fe/H] distribution. Here we explain the conspicuous trends observed in the plot from low [Fe/H] to high [Fe/H].

- [Fe/H] $< -2.0$: The Eu abundance is scattered over more than 3 dex (it is impossible to determine the lower [Eu/Fe] end because such stars do not show Eu feature at all). We usually interpret this feature as the consequence of the rarity of r-process event. These low [Fe/H] stars are formed out of gas that experience small number of enrichment events. Since r-process is rarer than usual enrichment event, we expect that the poisson noise is large, therefore the stellar Eu abundance can be diverse.

- $-2.0 <$ [Fe/H] $< -1.0$: The scatter of Eu abundance is not so large, and [Eu/Fe] is nearly constant around 0.5.

- $-1.0 <$ [Fe/H]: The scatter of Eu abundance is not large, and [Eu/Fe] decreases as the star gets Fe rich. We usually interpret this feature as the consequence of the type-Ia SNe contribution. Type-Ia SNe are the explosions of white dwarfs. White dwarf is a remnant of dead low-mass stars. The same logic as the AGB stars applies to type-Ia SNe: their contribution is only dominant at $-1.0 <$ [Fe/H]. Type-Ia SNe produce a lot of Fe, but they do not produce Eu at all. Therefore we observe the decreasing trend as the increasing [Fe/H]. This decreasing trend is also observed in [$\alpha$/Fe] - [Fe/H] distribution, because $\alpha$ elements are not produced in type-Ia SNe as well.

The chemical evolution suggests that (i) the r-process event should be rare, and (ii) the shorter delay-time is favored, in order to explain the contribution at low-[Fe/H] and the decreasing trend in high-[Fe/H].

An interesting question is: can NSMs explain the evolution of Eu abundance? From the discussions above, the NSM scenario faces two severe problems. Namely,

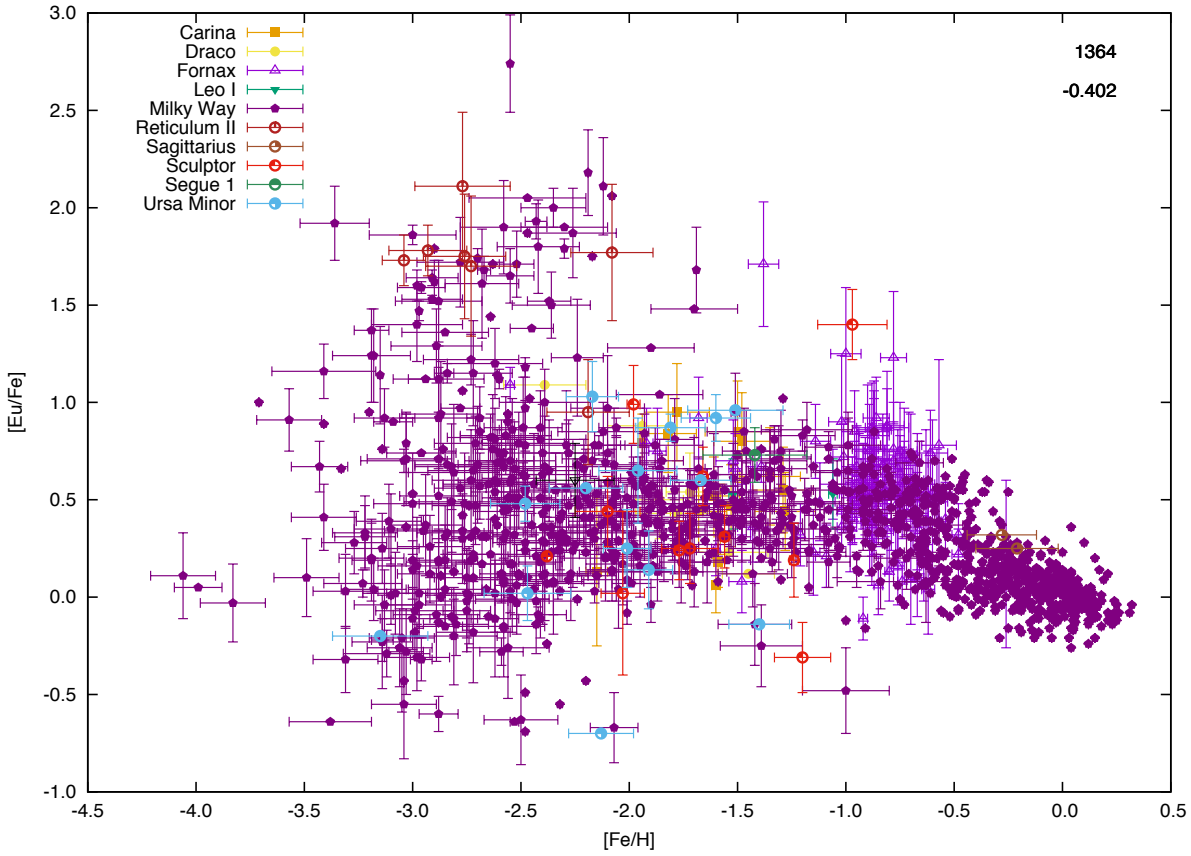


Figure 29: The r-process element abundances of MW and dwarf stars, extracted from SAGA database (Suda et al. 2008) on November 2019.

- The Eu enrichment of low [Fe/H] stars. Even a small number of gas processing by SNe of massive stars can easily enrich gas to [Fe/H] $\sim -2$. The fact that such stars are already enriched by r-process elements, the r-process events should happen soon after the star formation. However, it is expected that a long merging time is required before the merging of binary neutron-stars.

- The decreasing trend of [Eu/Fe] in high [Fe/H] stars. Binary population synthesis predicts that the delay-time distribution is proportional to $t^{-1}$ (because the delay time $t$ depends on separation by $t \propto a^4$, so the distribution of separation $P(a) \propto a^q$ means distribution of delay time $P(t) \propto t^{(q-3)/4}$. Typically $q = -1$ (Abt 1983) and the exact value of $q$ is insensitive to the delay time distribution). This is similar to the delay-time distribution of type-Ia SNe (Maoz et al. 2012). It makes it difficult to explain the decreasing [Eu/Fe] trend as the increase of [Fe/H], as the same power-law index means at later times their contribution compensate with each other.

- Abundance pattern. We know the elemental abundance pattern in the solar system. Since we (think we) know the contribution from the s-process to the elemental abundance pattern, we can subtract the s-process and obtain "pure" r-process contribution. This In Fig. 30 we show the Solar r-process abundance pattern.

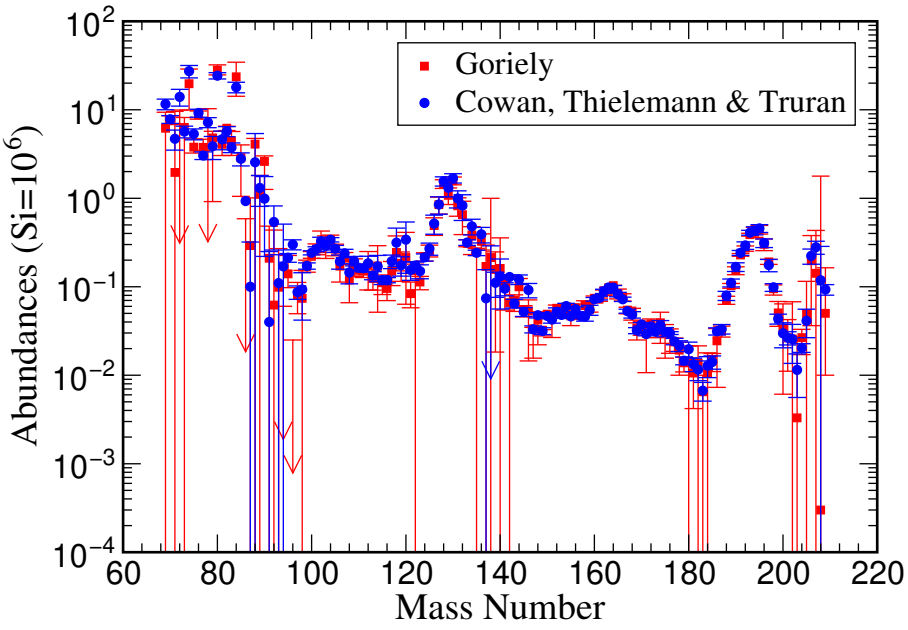


Figure 30: The solar r-process pattern taken from Cowan et al. (2019).

- Total amount of r-process elements today. In Fig. 31 we show the comparison of total Eu abundance at present and NSM rate or yield. The horizontal axis is the rate of NSM, and the vertical axis is the r-process ejecta mass from one NSM. Three tilted lines are observational constraints. The product of NSM rate and ejecta mass can be constrained, assuming that all the r-process elements are synthesized in NSMs. The difference of the three lines is from which element we count as the r-process elements.

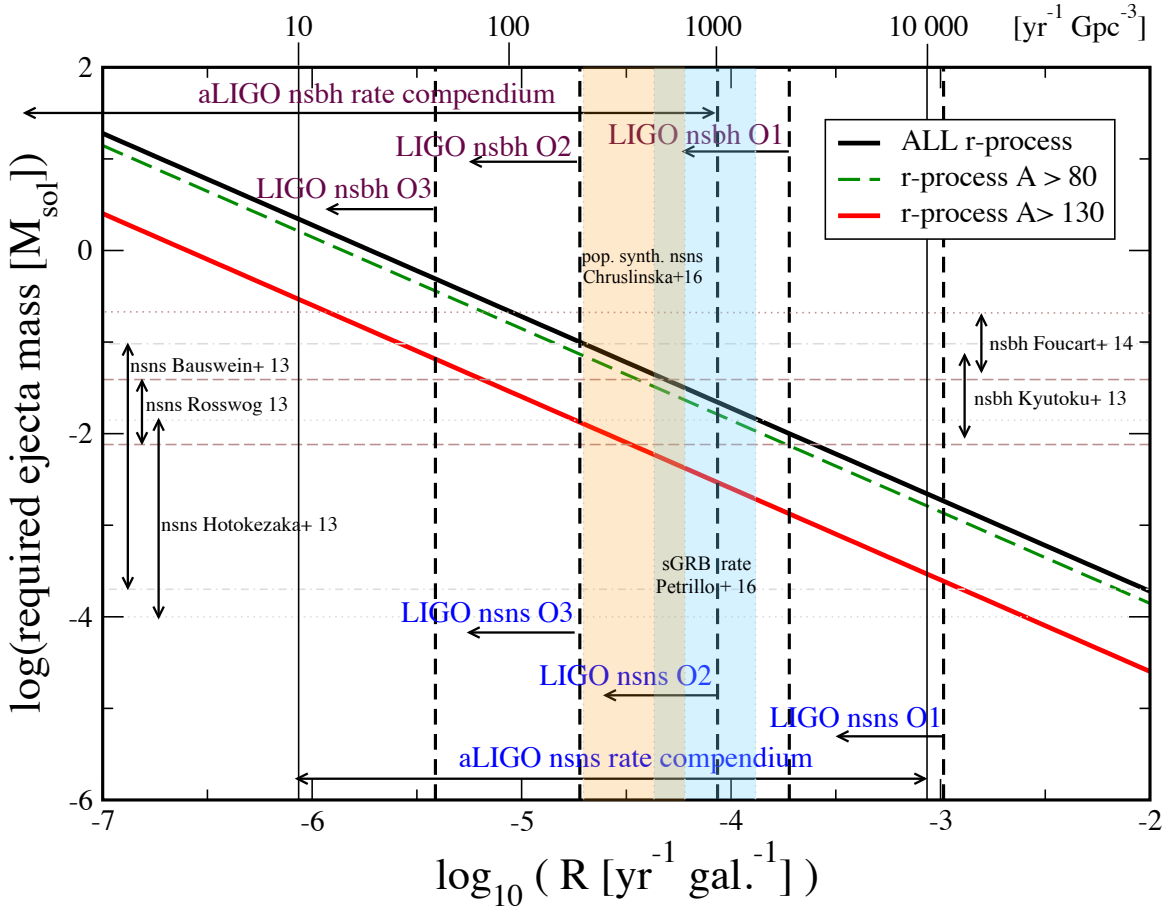


Figure 31: A figure shows the rate and yield estimate. The rate ($110 \sim 3840$ Gpc$^{-3}$yr$^{-1}$) and yield ($\sim 0.05 M_\odot$) estimated from GW170817 are roughly consistent to the total r-process element mass. This figure is taken from Fig. 2 of Rosswog et al. (2017).

"ALL" is from the beggining of the first peak, A $>$ 80 is from the middle of the first peak, and A $>$ 130 is from the second peak. It shows that the rate and yield estimate roughly matches to the observed r-process element abundance.

## 9.2 Ultra-Faint Dwarf (UFD) galaxies

UFDs are important for understanding the galaxy formation. In hierarchical structure formation predicted by the ΛCDM paradigm, large galaxies like the MW are formed via the mergers and accretions of smaller galaxies. UFDs are satellite galaxies of the MW, and also, they are the "building-blocks" of the larger galaxies (Simon 2019). Understanding physical processes (like star formation history, mixing of the UFDs

In Fig. 32 the scatter plot of Eu abundance in UFD stars are presented. Recently two r-process enriched UFDs are observed (Ji et al. 2016; Hansen et al. 2017; Marshall et al. 2018). Particularly the enrichment level of the highly enriched UFD (Ret-II) is consistent with one-NSM scenario. There are 12 other UFDs, without any trace of r-process elements.

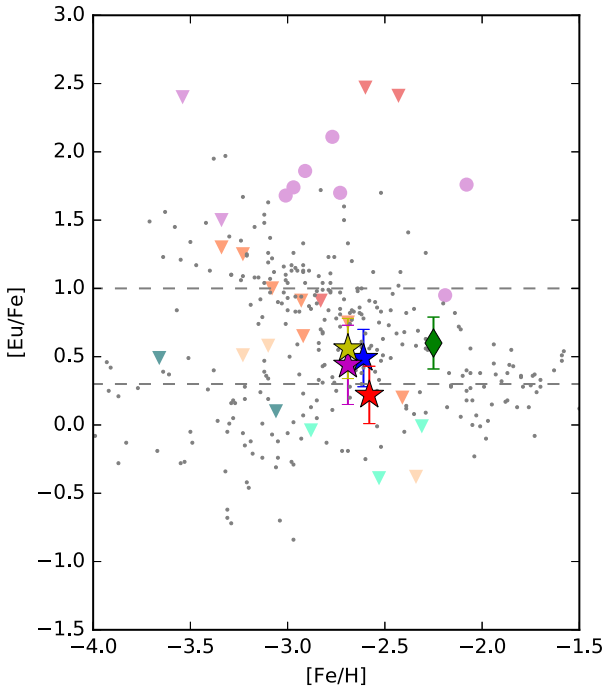


Figure 32: A figure that shows the stellar Eu abundance of UFDs. The diamond and four star symbols are showing the stars of Tuc III. The circles are stars with Eu detection, which are Ret II stars. Other colored downward triangles are stars of UFDs without Eu detection. The background gray dots are halo stars in the MW. This figure is taken from Fig. 5 of Marshall et al. (2018).

The rarity (2 out of 14 UFDs are enriched. This is one event per $10^5$ $M_\odot$) and the prolificacy (stars are enriched to [Eu/H] $\sim -1$) are both consistent to the NSM origin. Therefore NSM is the most promising candidate for the r-process in the Universe.

## 9.3 NSM observation

### 9.3.1 GW170817

The first direct detection of neutron-star merger (NSM) was the gravitational wave event named "GW170817". This event is especially important because we observe not only gravitational waves, but also the electro-magnetic counterpart. The fitting of the observed light curve by the theoretically predicted ones tells us that: (i) r-process is confirmed in the NSMs (by the decay of light curve), (ii) the total yield of r-process element is about 0.05 $M_\odot$ (by the fitting of the light curve), (iii) the NSM rate is about 1000 per $\mathrm{Mpc}^{-3}\mathrm{Gyr}^{-1}$. With the total yield and the rate estimate, we can check that the NSM alone can be the origin of all the r-process elements. (reference) stated that NSM can explain the amount of r-process elements we observe today, or if anything it overshoots the total amount. Since there remains a huge uncertainty both on yield and rate, it is not a serious tension, but many researchers come to believe that the NSMs are the dominant site of r-process element production.

### 9.3.2 short Gamma-Ray Burst (sGRB)

GRB is a bursty and temporal radiation of gamma-ray. The long-lasting ones ($\sim$ 1 month) are called just "GRB", and short-lasting ones are called "sGRB". The origin of the burst is unknown, but one promising candidate of sGRB is the NSM. R-process in sGRB is confirmed by Barnes and Kasen (2013).

# 10 Previous works on r-process enrichment

## 10.1 Constraining formation of neutron-star binary by the number of r-process enriched dwarfs (Safarzadeh et al. 2019b)

They investigated the formation of binary neutron stars. Although the merger of binary neutron stars is relatively well understood by the GR simulations and observation, the formation of binary is highly uncertain. The authors tried to constrain the formation by the rate of fast-merging binary neutron stars. With their analysis a common-envelope model that considers the separation between stellar cores is favored over another model that do not consider the separation and therefore the two stellar cores always merge.

They compare $2 \times 2 \times 2 = 8$ models. The first two stands for different common-envelope models, whether the stellar core merge or not. The second two is the metallicity. The evolution of common-envelope phase is metallicity dependent: they compare two different metallicities, $Z = Z_\odot$ and $Z = 0.1Z_\odot$. The last factor comes from the kick velocity: they compare a fast-kick model ($\sigma = 265\mathrm{km\ s}^{-1}$) and a slow-kick model ($\sigma = 135\mathrm{km\ s}^{-1}$). For all these settings, they calculate the formation rate of "candidate double neutron stars (DNSs)". A candidate DNS is a binary neutron star that merges inside the virial radius of the halo.

Their assumed kick velocity is anyway larger than typical escape velocity of the UFD progenitors, so they do not consider systems that captured in the halo and orbits for a long time.

In Fig. 33 we show a figure taken from Safarzadeh et al. (2019b). With this figure they argue that the "submodel A" in which the separation of stellar cores are taken into account matches the observed fraction of r-process enriched UFDs. In submodel B, the stellar core merges, and the formation rate of binary neutron stars is small in the first place, which fails to reproduce the fraction of r-process enriched UFDs. The caveat is the fact that the stellar mass estimate strongly depends on the stripped mass. They assume that more than 90 % of stellar masses are stripped, but this is highly uncertain.

## 10.2 r-process enhanced stars of the MW (Safarzadeh et al. 2019a)

They investigated the r-process enrichment of the MW stars. They have tested five models with different $t_{\rm min}, E_{\rm NSM}$, assuming that NSM is the only source of r-process elements. They use the fraction of CEMP-r stars, MP-rI stars, and MP-rII stars as the comparison metric between simulation and observation. With the analysis, they concluded that even with extremely short coalescence time model, NSM alone is not viable to explain the r-process abundance observation in the MW.

To identify MW-like halo, first they run a dark-matter only simulation to $z = 0$. They regard the halo is "MW-like" if (i) the halo mass is appropriate: at $z = 0$ the mass is $1 \sim 2 \times 10^{12} M_\odot$, and (ii) the halo is isolated: the maximum isolation parameter $\tau_{\rm iso,max}$ is small. The isolation parameter against halo $i$ $\tau_{\rm iso}$ is defined as:

$$\tau_{\rm iso,i} = \frac{M_{200,\rm i}}{M_{200}} \times \left( \frac{R_{200}}{r_i} \right)^3$$

they compute this $\tau_{\rm i}$ against all the halos, and take the maximum. The isolation parameter $\tau_{\rm iso,i}$ is large if a heavy halo exists close to the halo of interest. The small $\tau_{\rm iso,max}$ means the halo of interest do not get much external gravitational effect. They also compare the star formation history against various observations and simulations to increase the credibility of their method, including MW-like selection.

The origin of r-process is only the NSM. The NSM rate per CCSNe is $10^{-3}$, which corresponds to one NSM per $10^5 {\rm M}_\odot$. They investigated three different minimum delay time with $1, 10, 100$ Myr, while they fix the slope and the maximum of the delay time to $t^{-1}$ and 10Gyr. As for the explosion energy, they investigated three explosion energies, $10^{50}, 10^{51}, 10^{52}$erg. The Eu yield per event is taken to be $1.5 \times 10^{-5} {\rm M}_\odot$, which corresponds to assuming 0.04 $\rm M_\odot$ of ejecta with solar r-process pattern comes out.

In order to discuss the fraction of CEMP-r stars, they also need the source for carbon enhancement. They assume that all the Pop III SNe are C-rich and Fe-poor, so that they can naturally form CEMP stars. On each gas cells, they define a parameter $P$ that holds a pristine gas fraction. The $P$ is inherited to star particles when the gas particle is converted to a star particle. This $P$ stands for the fraction of Pop III stars in the star particle.

They conducted three tests to compare simulated result and observation: the fraction of MP-rI stars (stars with [Fe/H]$< -1$ and [Eu/Fe]$> 0.3$), the fraction of MP-rII stars (stars with [Fe/H]$< -1$ and [Eu/Fe]$> 1.0$), and the fraction of CEMP-r stars (stars with

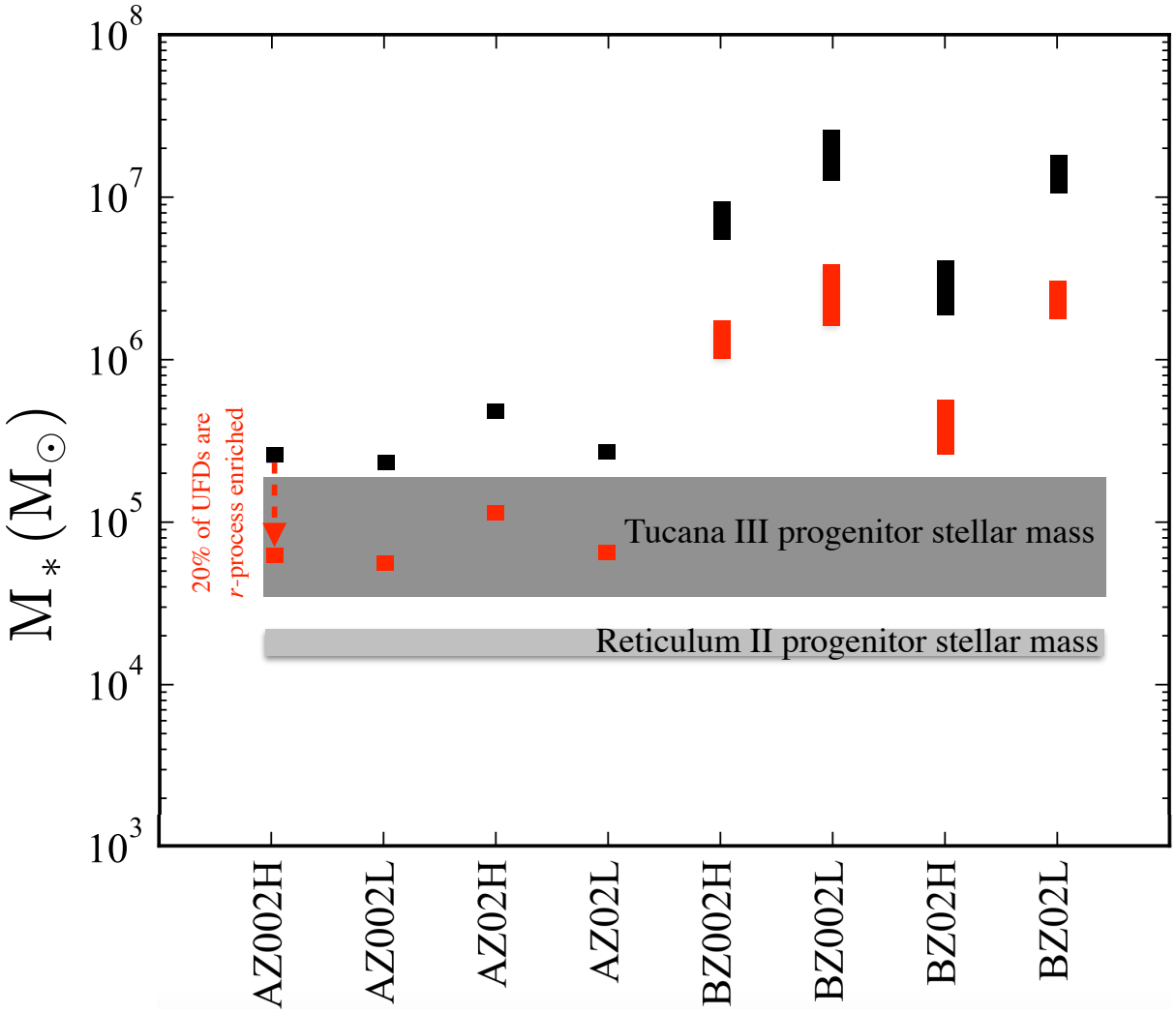


Figure 33: A figure compares the formation rate of fast-merging binary neutron stars that contribute to r-process enrichment of UFDs. The black dots or bars are showing the total stellar mass to form one binary neutron stars that enrich the host UFD. The orange dots or bars are 0.7 dex below the black ones, meaning observationally 20 % of UFDs are r-process enriched, therefore the actual stellar mass needed to reproduce the observed r-process rich fraction. The shaded regions are estimated progenitor stellar masses of two r-process rich UFDs, namely Ret II and Tuc III. This figure is taken from Fig. 5 of Safarzadeh et al. (2019b).

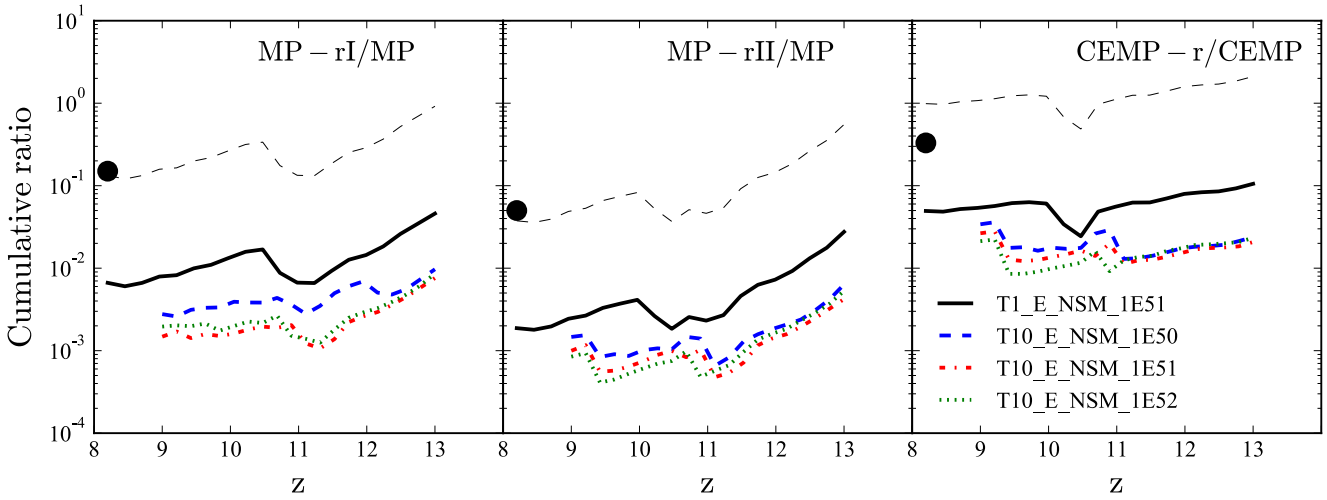


Figure 34: The stellar mass estimate of UFD progenitors with different models. The observed value (at $z = 0$) is shown with the black dot at $z = 8$. They justify comparing the observation at $z = 0$ to the simulation at $z > 8$ with the assumption that most of the metal-poor stars they use for comparison are formed before $z = 8$, when reionization happens. The four lines in the bottom are simulation results from four different model parameters. In the fifth parameter $t_{\rm min} = 100$ Myr no r-process enrichment was observed, so they cannot draw the curve from the model. The one line that matches the observation well is the model based on $(t_{\rm min}, E_{\rm NSM}) = (1{\rm Myr}, 10^{51}{\rm erg})$ in which they artificially boost the Eu production by a factor of 20. This figure is taken from Fig. 5 in Safarzadeh et al. (2019a).

[Fe/H]$< -2$, [Eu/Fe]$> 1.0$, and [C/Fe]$> 1.0$). In Fig. 34 we show the result figure taken from the paper. In all the three comparisons, any models they have used fail to reproduce the observed value. The shorter delay time model matches to the observation a bit better, although $t_{\rm min} = 1$ Myr is already quite short if we consider binary population synthesis. The difference in energy has a minor effect on the observed r-process relevant fractions. They argue that NSM alone is unlikely to be the dominant r-process site in the MW, because even with the best model parameter they investigated the NSM rate or the Eu yield should be 20 times more than the simulated value, which is unlikely.

Their work is interesting that they advanced one step from the naive abundance argument. When the Gravitational wave and its electromagnetic counterpart from a NSM was observed two years ago, from the rate estimate (with the survey volume, the survey period, and the number of detections) and the r-process yield estimate (with the light-curve fitting) it is argued that NSM alone can explain all the r-process elements in the MW. Their analysis suggests that the fraction of NSM ejecta to be captured by metal-poor stars is lower than naive expectations, because of the significant delay time of NSM.

## 10.3 The r-process element chemical evolution of the MW (Côté et al. 2019)

They investigated the r-process element abundance evolution of the MW stars. They claim that if we consider NSM as the only sites of r-process, it is difficult to reproduce the decreasing

trend in [Eu/Fe] as the increase in [Fe/H] observed in the high [Fe/H] stars. The key feature is the delay time distribution. They also consider two different delay times: steeper slope and burst in the first 100 Myr, and they succeed in reproducing the decreasing trend, but now it contradicts to the fact that sGRBs and SNe Ia both have high fractions of occurence in early-type galaxies.

Using a one-zone chemical evolution code, they follow the chemical evolution of the MW. In Fig. 35 we show the result of their chemical evolution model. The lower panel shows that the constant delay time model predicts the decrease of [Eu/Fe] vary well, whereas the $t^{-1}$ delay time fails to reproduce the trend. This is because the $t^{-1}$ delay time is similar to the one of type Ia SNe. The iron production is dominated by type Ia SNe after $\sim$ Gyr, which also follows $t^{-1}$ delay time. Therefore the two contributions cancels with each other.

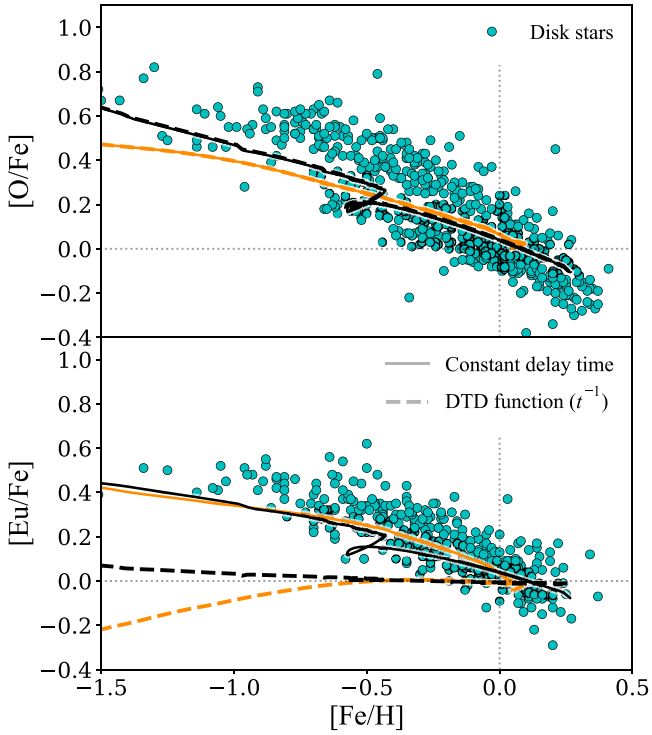


Figure 35: The chemical evolution of the MW with their model. The top panel shows the evolution of oxygen abundance. The bottom panel shows the evolution of Eu with different delay time distribution. Constant delay time matches well with the observation, whereas the usual $t^{-1}$ delay time fails to reproduce the decreasing trend in this [Fe/H] regime. This figure is taken from Fig. 3 of Côté et al. (2019).

They also test non-standard delay time distributions. The results are shown in Fig. 36. They consider two types of exotic delay time distributions: (i) steeper ($t^{-1.5}$) slope, and (ii) boost (10, 100 times) in the first 100 Myr. The bottom panel shows the highest boosting factor model matches the best with the observation. In this model about 90 % of Eu production happens before the onset of type-Ia contribution.

## 10.4 Constraining a sub-grid mixing parameter by r-process element abundance of stars in dwarf galaxies (Hirai and Saitoh 2017)

They investigated the effect of the mixing model in their SPH simulation. SPH simulation is a Lagrange method, in which we represent continuous field (like density) with particles. Usually in SPH simulation particles do not exchange mass with each other, but it has been pointed out that additional mixing is required to reproduce the observational elemental distribution (particularly $\alpha$ elements: (Revaz et al. 2016)). They have used barium (Ba) instead of $\alpha$ to determine a parameter that control the efficiency of the mass exchange between particles. Through the comparison of [Ba/Fe] distribution between the simulated stars and the observed stars, they have concluded that the mixing parameter $C_d$ should be larger than 0.01. With this parameter it takes $\sim 40$ Myr to mix the galaxy well. We are giving a further explanation.

They implement a new model to include sub-grid turbulent metal diffusion in their SPH simulation. The equation is as follows: "The $i$th metal, $Z_i$, diffuses to surrounding gas particles with the equation

$$\begin{aligned} \frac{dZ_i}{dt} &= \nabla(D\nabla Z_i) \\ D &= C_d|S_{ij}|h^2 \end{aligned}$$

where $C_d$ is the scaling factor for metal diffusion, $S_{ij}$ is the trace-free shear tensor, and $h$ is the smoothing length of SPH." With the parameter $C_d$ they can manipulate the efficiency of sub-grid mixing. They have tested five different diffusion parameters: $C_d = 0.0$(no mixing implemented), $10^{-4}, 10^{-3}, 10^{-2}, 10^{-1}$.

They prepare an isolated dwarf galaxy with $7 \times 10^8 \mathrm{M}_\odot$ as the initial condition. The final stellar mass is $5 \times 10^6 \mathrm{M}_\odot$, corresponding to the stellar masses of dwarf galaxies.

In Fig.10.4 we show the plots taken from their paper. The left panel shows the Mg (typical $\alpha$ element) abundances, and the right panel shows the Ba (typical r-process element) abundances. From the Mg distribution it is difficult to favor any of the models: the observed Mg abundance scatter in dwarf galaxies is similar to the models (c), (d) and (e), but the observational error ($\sim$ 0.5dex) is already enough to explain the scatter. The Ba distribution is more informant on the mixing parameter. They focus on whether the models produce stars with [Ba/Fe]$\geq$ 1. Observationally except for Ret II there are no stars in dwarf galaxies with [Ba/Fe]$\geq$ 1. The stellar mass of Ret II is quite small compared to the simulated galaxy, and they ignore Ret II. The right panel shows that in models (c), (d), (e) there are some stars with [Ba/Fe]$\geq$ 1. (a) and (b), which are $C_d > 0.01$, models are favored over $C_d < 0.01$ models.

Two other representations of the mixing parameter $C_d$ exist. One is the diffusion coefficient $D(\mathrm{kpc}^2\mathrm{Myr}^{-1})$. The favored $Cd = 0.01, 0.1$ corresponds to $D = 2\times10^{-4}\mathrm{kpc}^2\mathrm{Myr}^{-1}, 2\times 10^{-5}\mathrm{kpc}^2\mathrm{Myr}^{-1}$. The other is the mixing timescale. They estimated the mixing timescale of $C_d = 0.01, 0.1$ models to be $\leq 10\mathrm{Myr}, \sim 40\mathrm{Myr}$, respectively. These are shorter than the dynamical time of their simulated galaxy ($\sim$ 100Myr), suggesting that the mixing take place before the typical star formation occurs in the galaxy.

Their results, "Ba distribution is more informant than $\alpha$ element distribution on the mixing in the galaxy", is natural and interesting. It is natural because Ba is only produced in

rare occasion, but $\alpha$ elements are produced in almost all core-collapse supernovae (CCSNe). CCSNe is not rare in dwarf galaxies ($\geq$ 1000 times), and the spread in spatial positions naturally homogenizes the $\alpha$ element distribution. On the other hand, typically Ba is produced in rare events ($\sim$ 10 times), and the number of events is not enough to well sample the overall galaxy. This suggests that the r-process element distribution is useful to investigate the metal mixing in galaxies.

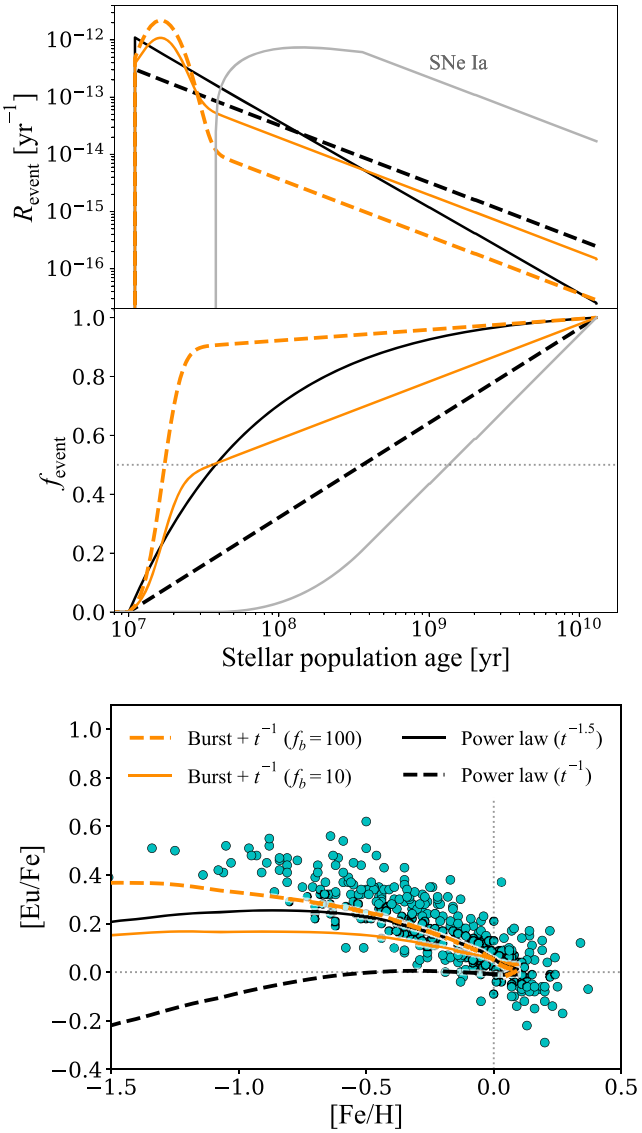


Figure 36: Different delay times and corresponding chemical evolution of the MW. The top two panels show the time evolutions of event rate and cumulative event rate. The bottom panel shows the evolution of Eu abundance with different delay time distributions. The model with the highers boosting factor reproduces the evolution of Eu abundance best. The figure is taken from Fig. 7 of Côté et al. (2019).

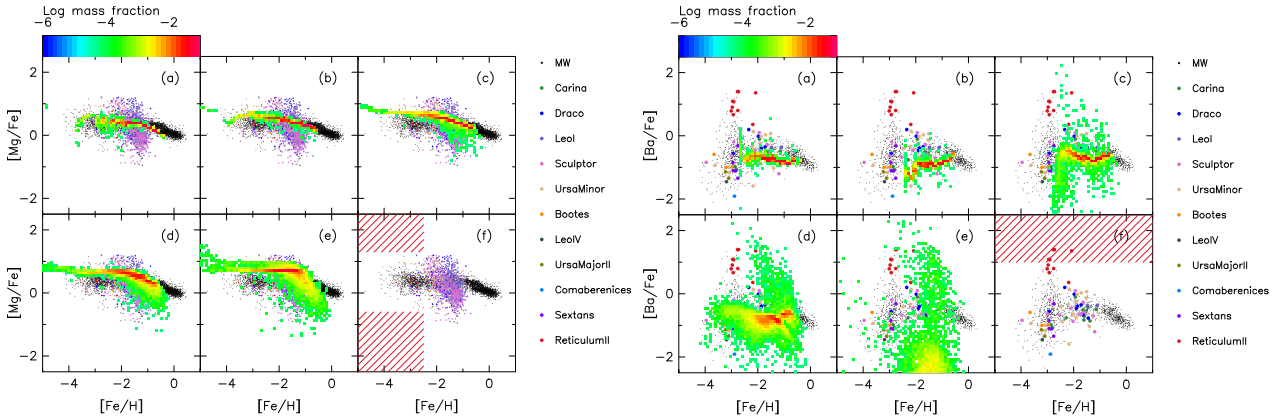


Figure 37: The Mg, Ba and Fe abundance patterns of dwarf galaxy in their simulation with different mixing coefficients. The difference of two panels is the elements: the left panel shows the Mg (typical $\alpha$ element) abundance, while the right panel shows the Ba (typical r-process element). In all six panels the Mg/Ba abundances of observed stars are plotted in the background. In (a) to (e) they overplot the simulated Mg/Ba abundance distribution. (a) is the most efficient mixing model ($C_d = 0.1$), (b) is $C_d = 0.01$ model, (c) is $C_d = 0.001$ model, (d) is $C_d = 0.0001$ model, and (e) is no mixing model ($C_d = 0$). The red shaded region in (f) shows the region that no observed stars exist. When they plot Ba abundance of stars with [Fe/H]$> -2.75$, they calculate the Ba abundance from Eu abundance assuming [Ba/Eu]$= -0.89$, to avoid the contamination from the s-process. The figures are taken from Fig. 1 and Fig. 2 in Hirai and Saitoh (2017).

# 11 Motivation

Our purpose is to investigate what we can learn about the host galaxy and the origin of r-process elements, from the [Eu/Fe] - [Fe/H] scatter plot of UFDs. The overall abundance of Eu is consistent to a scenario in which a rare, prolific event enriches the galaxy with r-process elements. However, the diversity in the progenitor system or the environment is still not investigated in detail. For instance, since binary neutron-stars receive a kick when they are born. Therefore the merger can happen at the outskirt of the galaxy.

Particularly I want to study the effect of explosion position and the star formation history of the galaxy. Scientific topics that we can address with this work are:

- What is the typical star formation history of UFD, which are the building blocks of galaxies?
- what is the origin of r-process elements? Are they NSM, or some rare CCSNe?

We will address to these questions in the discussion section.

# 12 Method

## 12.1 cosmological simulation

We use cosmological simulation to investigate the mixing of r-process elements in the galaxy. The boxsize is 1.0 cMpc/h. The masses of the dark matter particles and the gas particles are 102 $M_\odot$ and 19 $M_\odot$. The simulation is evolved to $z \sim 6$, when reionization proceeds and the star formation in UFD progenitors quench. The code settings such as star formation and feedback models are the same as in Auriga simulation (Grand et al. 2017). The details of the model are presented in the paper. Our purpose for using the cosmological simulation is to see how the r-process ejecta mix with gas in a galaxy.

First we run a non-zoom simulation of $2 \times (256)^3$ particles. The initial conditions are created with MUlti-Scale Initial Condition generator MUSIC (Hahn and Abel 2011). The box size is (1 comoving Mpc/$h$)$^3$. With this low-resolution simulation, we can identify some halos using friend-of-friend algorithm. We select halos to zoom-in and investigate by the stellar mass and the halo mass. First, the halo mass at $z = 8$ should be around $10^8$ $M_\odot$ (Safarzadeh et al. 2018b). Second, substantial amount of star formation occurs so that the possibility of hosting one binary neutron stars is not too small. We identify three halos that satisfy these conditions. In Fig. 38 we show the projection plots of metallicities and star formation histories. Typical [Fe/H] of three halos are [Fe/H] $= -2.35, -2.49$, and $-2.64$. These are consistent to the values of UFDs: Ret II (-2.65: Simon et al. (2015)) and Tuc III (-2.42: Simon et al. (2017)), suggesting that our simulated galaxies reasonably resemble the observed UFDs.

## 12.2 r-process production treatment

We do not simulate the evolution of the progenitor system like the NSM. What we do is something like "bubble painting". At a time when (i) the galaxy has some stellar mass,

and (ii) the galaxy forms substantial amount of stars. The first condition is necessary to produce binary neutron-stars, and the second condition is necessary because what we want to investigate is how the elements are captured by the stars. I assume that $2 \times 10^{-4} M_\odot$ of Eu is produced by one NSM. This is consistent to the scenario that 0.05 $M_\odot$ of r-process elements are produced, and the abundance pattern is the same as the solar r-process abundance pattern starting at mass number $A = 90$ (Arnould+07).

A binary neutron star receive a kick when they are born (Beniamini et al. 2016). It also has some time between the formation and merger. Therefore we expect some of the merger happens outside the star-forming region. We model such explosion at off-center of the galaxy. We pick up many points inside and outside the virial radius. One point in the center, and 26 points on each sphere with radius [0.1, 0.5, 1.0, 1.5, 2.0, 2.5, 3.0, 5.0] times virial radius. If we express the "26 points" with polar coordinates, $(\theta, \phi) = (0, 0), (\pi/4, i), (\pi/2, i), (3\pi/4, i), (\pi, 0)$ with $i$ runs every $\pi/4$ from 0 to $7\pi/4$. In the simulation we distinguish the ejecta from different points. Since the kinematic effect of each NSM is small, we can investigate many models at one simulation.

We prepare three different galaxies with different star formation histories (Table 2 and Fig. 38). The dilution of r-process rich ejecta into the ISM is driven mainly by star formation and feedback. Therefore the timing of star formation and NSM is crucial. This timing is chosen so that (i) the galaxy already forms some stars, therefore the formation of a binary neutron stars is possible, and (ii) the galaxy still form stars so that the ejecta from NSM can be captured by stars. We prepare four groups of models with different star formation durations. Two of them are on halo 1: long star formation (that the r-process ejecta is deposited at the left horizontal solid line of Fig. 38), and short star formation (that the r-process ejecta is deposited at the horizontal dashed line of Fig. 38). The other two are the models on halo 2 and 3. For all the galaxies the star formation is quenched by the end of the simulation ($z = 6.6$). This quench is the result of heating and evaporation of hydrogen gas by the external radiation field. This is a common feature of UFD progenitors.

We model the dilution of NSM ejecta on a galactic scale. Turbulent motion of ISM driven by gas in-fall and stellar feedback is the dominant driver of the mixing. Therefore we only need to simulate from the end of the "snowplough phase" (Mo et al. 2010). Here we explain how we calculate the radius. First we calculate the radius and velocity of a shocked shell in the self-similar phase as a function of $t$, assuming that the explosion energy $E$ is $10^{51}$ erg. Then we assume that the self-similar phase ends when 1/4 of the injected energy is radiated away. The shell radius and velocity at the endpoint are:

$$r_{\rm sh} = 23 \times \left(\frac{n}{1{\rm cm}^{-3}}\right)^{-19/45} \times \left(\frac{E}{10^{51}{\rm erg}}\right)^{13/45} {\rm pc} \tag{72}$$

and

$$v_{\rm sh} = 200 \times \left(\frac{n}{1{\rm cm}^{-3}}\right)^{2/15} \times \left(\frac{E}{10^{51}{\rm erg}}\right)^{1/45} {\rm km\ s}^{-1}, \tag{73}$$

where the $n$ represents the number density of hydrogen atoms in cm$^{-3}$. Once the radiative cooling becomes important, the shell cannot receive the pressure support. Then the shell become "momentum-driven snowplough phase". In this case the momentum is conserved, therefore the velocity scales as $v \propto r^{-3}$. We assume that the momentum-driven snowplough

ends when the velocity of the shell becomes comparable to the turbulent velocity of the ambient gas ($\sim$ 10km s$^{-1}$. Then the final radius is

$$r_{\rm sp} = r_{\rm sh} \times \left( \frac{v_{\rm sh}}{10{\rm km\ s^{-1}}} \right)^{1/3}. \tag{74}$$

On each explosion point, we define a "NSM bubble" with the radius $r_{\rm sp}$. For the cells within $r_{\rm sp}$, we distribute r-process elements proportional to its cell volume. This treatment is effectively assuming that the dense region is less likely to be enriched with r-process elements.

We also ran two other simulations with different explosion energies: $10^{50}, 10^{52}$ erg and checked that the qualitative result did not change. This is consistent to the result of Safarzadeh and Scannapieco (2017). As I presented before, the main physical process for the mixing of ejecta into the ISM is a large-scale turbulence by star formation and kinematic galaxy evolution. The exact size of the $r_{sp}$ is not important for abundance pattern.

| | stellar mass after NSM($M_\odot$) | SF duration(Myr) |
|---|---|---|
| Halo 1 | 15000 | 335 |
| Halo 2 | 4000 | 250 |
| Halo 3 | 1500 | 142 |
| Halo 1, late | 5000 | 95 |
| Ret II | 2600 | - |

Table 2: Halo star formation properties. The stellar mass of Ret II is the observed value at present (Bechtol et al. 2015).

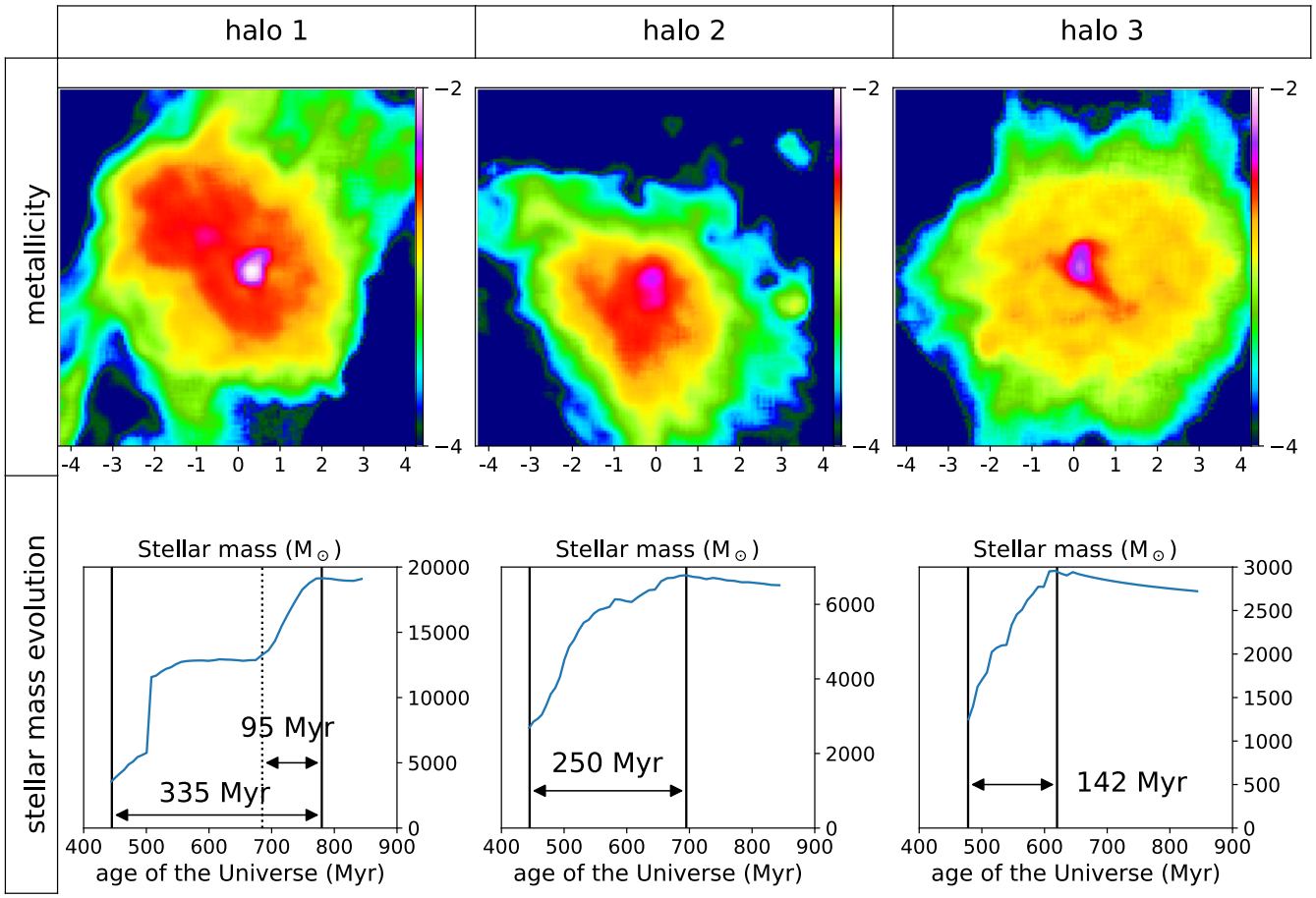


Figure 38: Top panels are the projection plots of gas metallicity distributions and star formation histories. Three halos are presented from left to right. We call them Halo 1, Halo 2, and Halo 3. The density-weighted metallicity is the value in log, normalized to Solar metallicity. The bottom ticks show the distances from each galactic centre in physical kpc. The bottom panels are the star formation history of simulated galaxies. Each panel has two solid vertical lines. The left one is the moment of r-process elements deposition, and the right one is the end of star formation. Only the left bottom panel contains a dashed vertical line. This is the moment of r-process elements deposition in "late" simulation.

# 13 Result

We compare the Eu abundances of stars in the simulated galaxies with those of the two r-process enriched UFDs, Ret II and Tuc III.

## 13.1 NSM explosion site

In Fig. 39 we show the relation between the overall Eu abundance and the distance of NSM from the center. We can see an decreasing trend outside the virial radius ($R > r_{\rm vir}$). This is natural because the virial radius is the typical distance that the gravity from the galaxy becomes negligible. The resulting [Eu/H] in this region depends strongly on the star formation duration. Halo1, in which star formation continues for 335 Myr, the [Eu/H] tail extends to relatively large radius. The other halos, in which star formation quench within shorter period of time ($\lesssim$ 250 Myr), the halo contains smaller amount of Eu, and often negligible. For distance shorter than the virial radius ($R \leq 0.5 r_{\rm vir}$), we only see a weak dependence of [Eu/H] on the radius. All the halos are enriched to [Eu/H] $= -0.5 \sim -1.0$. This is consistent to the Eu abundance of Ret II ($-0.82$ if we only include stars with detection, and $-0.93$ if we include all the stars in Ret II (Ji et al. 2016)). Since the r-process enrichment of UFDs are a stochastic event (because the stellar mass is not so large to allow multiple r-process events), [Eu/H] does not correlate with the stellar mass, but it correlates with the dilution mass of the halo.

Another r-process enriched UFD, Tuc III is less enriched with Eu: [Eu/H] $\sim -2.0$ (Marshall et al. 2018). This can be explained by either (i) NSM happens around or outside the virial radius, or (ii) the dilution gas mass is large. I will discuss each scenario in turn. For the first scenario, it is suggested from Fig. 39 that the NSM distance from the galactic center should be around virial radius. Since the typical virial radius is 1 kpc, it is possible that the BNS is kicked out with velocity 25km/s ($\sim$ escape velocity of the galaxy) and travel for more than 40 Myr, exploding around the virial radius in the end. For the second scenario, we need 10 times more gas to explain the [Eu/H] of Tuc III. This means typically the UFD progenitor halo should be more massive by 10 times, resulting in $10^9 {\rm M}_\odot$ at $z = 8$. This is too massive as a UFD progenitor (Safarzadeh et al. 2018b). Therefore we argue that the first scenario is favored over the second scenario.

With the shorter star formation halos, halo2 and 3, the mean [Eu/Fe] of Tuc III can be reproduced in some of our models. However, the small scatter of the [Eu/Fe] distribution cannot be reproduced. This is a consequence of incomplete mixing of r-process elements. With their short star formation duration, the r-process elements cannot be mixed well before the Eu abundances are locked in stars. We further discuss this point.

## 13.2 Star formation duration

Stars in the two r-process enriched UFDs have quite a similar [Eu/Fe] values within each galaxy. We also need to reproduce the trend. Here we explain how the duration of star formation plays a role.

In Fig. 41 we compare the Eu abundances of stars in Halo 1. The left panel is the early explosion, in which the star formation continues for 335 Myr after the r-process element

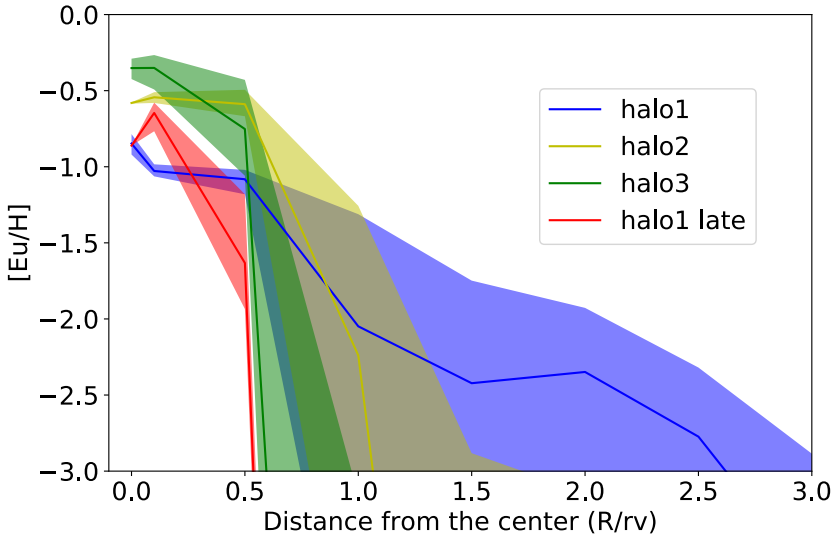


Figure 39: The relation between r-process element retainment fraction and the distance of explosion site from the center. On each radius values between 75 percentile and 25 percentile are colored.

injection. The right panel is the late explosion, in which the star formation quenches 95 Myr after the NSM. The distribution in the left panel shows that the [Eu/Fe] of star particle is similar to each other. This is a consequence of long star formation after the r-process element injection: since there is enough time to mix the galaxy, the [Eu/Fe] is almost the same among stars. The right panel is the opposite example. The [Eu/Fe] distributes in a wide range with more than 1 dex of scatter. The large scatter in Eu abundance can be explained by the short mixing time: there is not enough time to mix, therefore stars distribute in a wide range of Eu abundances.

The points on the figure also show the formation epochs of the star particles. Both in Figs. 40 and 41, we see the evolution from low [Fe/H] to high [Fe/H] as time elapses. There is also a slight downward tilt. This is the consequence of constant Eu abundance and increasing Fe abundance, as iron production by stars proceeds over time.

The analysis above clarifies that the dilution of r-process elements critically affects stellar Eu abundances. Here we explain the stellar feedback treatment in our simulation. When SNe happen, they inject momentum into the ISM of the galaxy. The momentum causes galactic winds which stir the ISM, helping NSM ejecta to dilute. Such stellar kinetic feedback is modeled by ejecting "wind particles" in random directions (Springel and Hernquist 2003). Wind particles carry 40 % of the metals ejected by the SNe, and the remaining metals are directly distributed to nearby gas cells (Vogelsberger et al. 2013). The wind particles travel until they reach to a gas cell with $\rho_{\rm g} < 0.05\rho_{\rm th}$, or their age exceeds the maximum travel time. Finally the wind particle deposits its mass and other properties when they disappear.

SNe-driven mixing is efficient in the center of each galaxy, where star formation mainly take place. Also in the outskirt of a galaxy, r-process ejecta eventually dilutes into the surrounding hydrogen gas by gas accretion and galaxy mergers, but longer time is required.

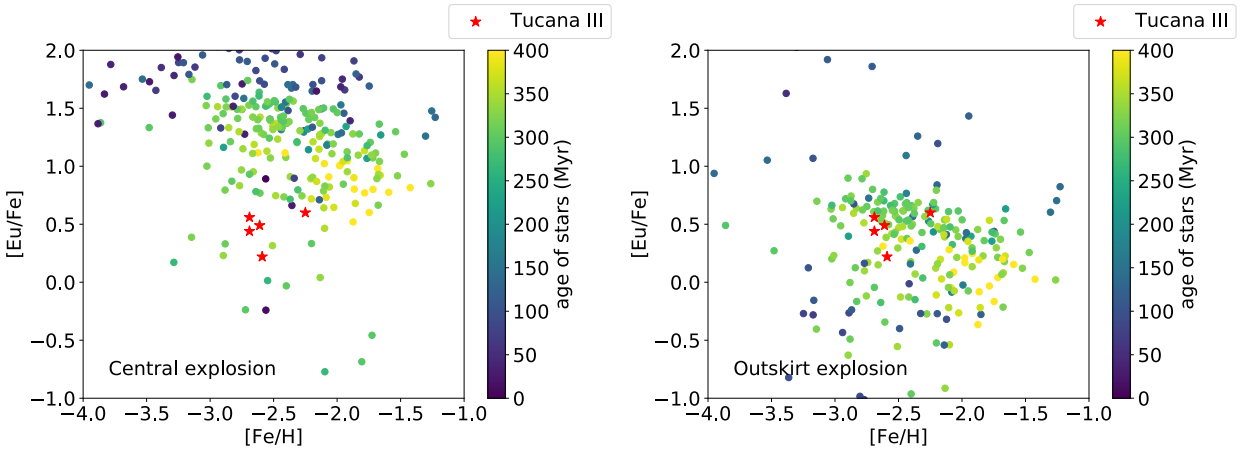


Figure 40: [Eu/Fe] - [Fe/H] abundances of star particles in halo 1, compared to the observed stellar abundances of Tuc III. Left panel: The NSM occurs at the center of the galaxy where the main star formation occurs. Right panel: The NSM occurs at around the virial radius of the galaxy. The mean [Eu/Fe] in the right panel is closer to the observed value of Tuc III.

In order for the model prediction to be consistent with the observed Eu distribution of stars in UFDs.

In Fig. 42 we show the diffusion coefficients of halo 1. This is obtained by fitting the Eu abundance of gas cells with a 3-dimensional Gaussian function. By the fitting we obtain the parameter $\sigma$ in Gaussian at each snapshot. Then the diffusion coefficient $D$ can be calculated by a relation $2Dt = \sigma$. The estimated diffusion coefficients are: in the center of the UFD progenitor $D \simeq 1 \times 10^{-3}$ kpc$^2$ Myr$^{-1}$ $\simeq 3 \times 10^{26}$ cm$^2$ s$^{-1}$, and in the outskirt of the galaxy $D \simeq 2 \times 10^{-4}$ kpc$^2$ Myr$^{-1}$ $\simeq 6 \times 10^{25}$ cm$^2$ s$^{-1}$. Within 250 Myrs, the r-process elements deposited in the center of a galaxy is mixed with the gas in the central 50% of UFD, which includes its star-forming region well inside.

The diffusion coefficient $D$ is of great importance and there are a lot of works on the parameter. Karlsson (2005) argued that, with his stochastic metal production model, $D \simeq 7 \times 10^{-4}$ kpc$^2$ Myr$^{-1}$ best reproduces the metallicity distribution function of low-mass stars in the MW. Hirai and Saitoh (2017) implement a sub-grid diffusion recipe in their SPH simulation, and studied the efficiency of mixing. By the comparison of barium abundances of stars in their simulated galaxies and in the MW or in dwarf galaxies, they find that $D > 2 \times 10^{-5}$ kpc$^2$ Myr$^{-1}$ is required. Ji et al. (2015) use $2.4 \times 10^{-3}$ kpc$^2$ Myr$^{-1}$ as their fiducial value of the effective diffusion coefficient. Our derived diffusion coefficient is consistent to all these values in the literature.

# 14 Discussions

## 14.1 Star formation histories of the UFDs

Our results suggest that the mixing efficiency of NSM ejecta into the ISM is important for the Eu abundance distribution. The efficiency is determined by the timing of the NSM and

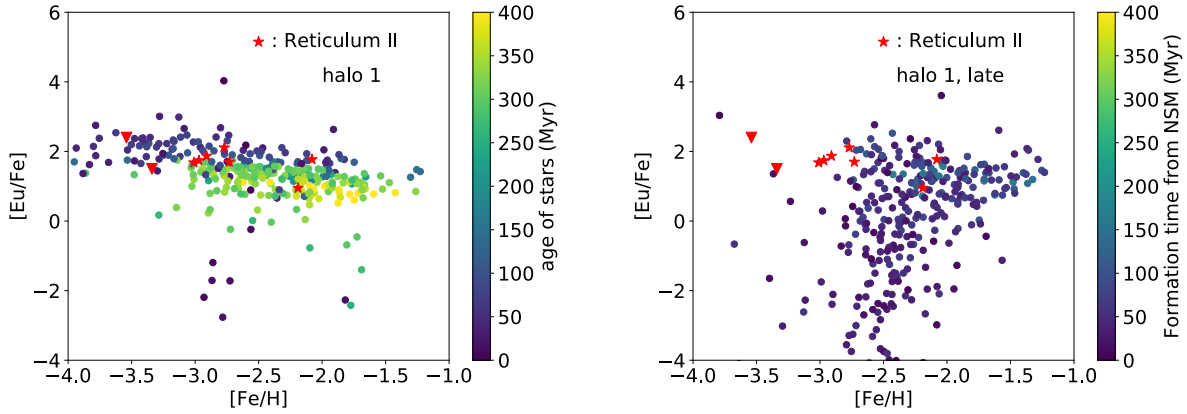


Figure 41: [Eu/Fe] - [Fe/H] abundances of star particles in halo 1, compared to the observed stellar abundances of Ret II. In both panels NSM occurs at the center of the galaxy. Left panel: The NSM occurs at the early stages of star formation. The simulated star particle have similar [Eu/Fe] to each other, consistent to the observation of stars in Ret II. Right panel: The NSM occurs at late stages of star formation. It shows a significantly large scatter of [Eu/Fe] among the member stars, which is inconsistent with the observations of Ret II.

star formation in the galaxy. The Eu abundance scatter among stars in UFDs can be used to infer the star formation histories of the UFDs. Assuming a continuous star formation, the duration should be longer than 300 Myr. This is long compared to the typical free-fall time $t_{\rm ff} = \sqrt{\frac{3\pi}{32G\rho}} \simeq 70$ Myr. In order for the gas to be mixed sufficiently, the binary neutron-stars should be formed early in the history, and the binary merges with short delay time, and star formation continues for a long time.

Such difficulties lead us to consider multiple, separated star formation scenario. However, we do not have enough observation to make any decisive argument. It is interesting to observationally confirm the existence of "first-generation" stars in r-process enriched UFDs, which do not contain Eu at all. The fraction of the Eu-less stars tell us the timing of NSM in its star formation history.

## 14.2 Natal kick of neutron-star binaries

Our analysis have shown that the high Eu abundance in Ret II stars can be reproduced if an NSM occurs at the center of the progenitor. If a binary neutron stars receive a small kick at its formation, such central explosion happens after the delay time. Also, if the delay time is quite small, NSM happens near the center. For Tuc III, explosion at the outskirt better explains the stellar Eu abundance. This corresponds to a case with medium kick, comparable to the virial radius of the galaxy, and the binary neutron stars orbits at around virial radius. It is interesting that the velocity distribution has two populations: high kick and low kick (Beniamini et al. 2016).

Typical natal kick of each neutron star is the order of 100 km/s. This is larger than the escape velocity of a typical UFD progenitor. Therefore a good fraction of binary neutron

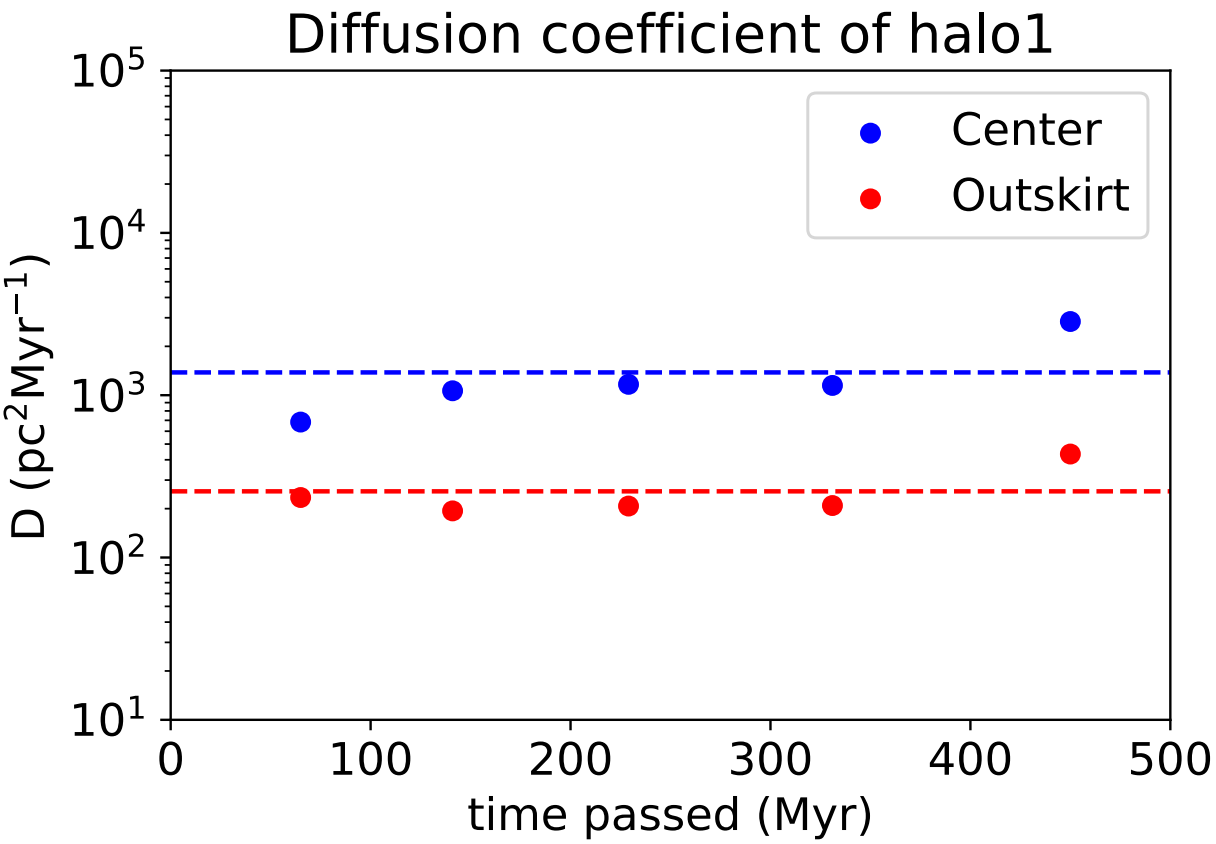


Figure 42: The diffusion coefficients calculated by the dilution of r-process elements. We fit the r-process elemental abundance in each gas cell with a three-dimensional Gaussian to estimate the coefficients. The details are described in the main text. The horizontal dashed lines are the average values of the coefficients measured at different moments.

stars can escape from the original halo before they merge. We calculate the fraction of binary neutron stars that contribute to the enrichment of the UFD progenitor. Here we assume the virial radius of the UFD progenitor is 1 kpc and the binary kick velocity follows the Maxwell-Boltzmann distribution with a velocity dispersion $\sigma$. For the delay time we assume a $t^{-1}$ distribution from $t_{\rm min} = 10$ Myr to $t_{\rm max} = 10$ Gyr. Fig. 43 shows the inner explosion fraction as a function of the velocity dispersion $\sigma$. In general, the inner explosion fraction is actually low. This inner explosion fraction can be used to constrain the kick velocity distribution. However, note that there are a few factors that we have to make crude assumptions. Our discussion is based assumptions below. (i) Dead stars correction: since the stellar population in UFDs we observe today is very old, only low-mass (less than 0.8 $M_\odot$) stars survive. Assuming that the IMF is the one proposed by Chabrier (Chabrier 2001), the mass fraction of currently surviving stars is 36 % of all the stars. The surviving fraction is not sensitive in the range from 0.6 $M_\odot$ to 1.0 $M_\odot$. (ii) No tidal stripping: the UFDs we observe today do not lose their mass by tidal stripping. There are 14 UFDs for which the stellar Eu abundance is observed (Simon 2019). With the two corrections above, the total initial stellar mass of 14 UFDs is $2.3 \times 10^5 M_\odot$. With a typical formation rate (1 per $10^5 M_\odot$)

of merging neutron-star binaries, we have 2.3 merging neutron-star binaries on average. Note that we have not applied the kick-out effect: it is already consistent to the number of r-process enriched UFD. We can deduce that most merging binary neutron-stars explode within the galaxy they are formed. High velocity dispersion model is disfavored with this argument. To make the $\sigma > 100$ km/s model compatible, The UFD progenitor should lose its mass more than 90 % on average.

In metal enrichment by SNe, external enrichment can be important. However, for binary neutron stars or r-process elements such scenario is unlikely. In our cosmological simulation, the typical physical distance between a pair of star-forming galaxies is $\sim 60$ kpc at $z \sim 11$, and the size of each UFD progenitor is $\sim 2$ kpc. Then the success rate is $\sim 10^{-4}$ if we only consider the direction of the initial velocity (because solid angle of the neighboring galaxy is $\pi/(60)^2$). In addition we have the third axis: in order for the NSM of externally formed binary neutron-stars to happen, we have to fine-tune the explosion moment. A rough estimate of rate for the merger to occur inside a galaxy (under the assumption that the velocity vector is perfect) is (2 kpc)/(60 kpc) = 1/30. Multiplying these factors, it is quite rare for UFD progenitors to experience an "external" r-process enrichment.

## 14.3 NSMs or CCSNe?

In this work we have assumed that NSMs are the only r-process enrichment sources. However, theoretically other origins are also considered: magneto-rotational SNe and collapsars (Woosley 1993; Siegel et al. 2019; Nishimura et al. 2015). These are rare types of CCSNe. Since the lifetime of a massive star is short, their delay time is also short. This is a conspicuous difference: NSM can occur at a distant place from its formation, but these rare CCSNe mostly occur at the place of its birth.

Galactic chemical evolution works suggest that the main r-process origin should be some kind of rare CCSNe. In van de Voort et al. (2019), the authors argue that the model in which only NSMs are the r-process origin is incompatible with the observation. The point is the behavior of [Eu/Fe] at low-[Fe/H] regime. Since NSMs require quite a long time after the formation, they cannot contribute to the Eu enrichment of low-[Fe/H] stars. Any r-process source with no delay time can be the candidate source of Galactic Eu enrichment.

Tuc III is an UFD moderately enriched with Eu. In our models the model that cause NSM at the point with the offset of a virial radius (Fig. 39). All models of central explosion was disfavored. For the low Eu abundance three interpretations are possible. (i) Explosion happens at outside the galaxy, as in our model. The total amount of Eu captured in stars is small. (ii) The halo mass is large, therefore the [Eu/H], which is determined by Eu mass over H mass, is low. (iii) The Eu yield in one NSM is small. We here argue that the first scenario is the most likely one. For scenario (ii), the hydrogen mass should be $4 \times 10^7 M_\odot$ to obtain [Eu/H] $\simeq -2.0$. Assuming the Eu is diluted to 30 % of hydrogen within virial radius (this is the typical value in our simulation), and the cosmic baryon fraction is about $1/5 \sim 6$, the halo mass should be about $8 \times 10^8 M_\odot$. This is too massive compared to the predicted mass range of UFD progenitors (Safarzadeh et al. 2018b). The estimate on the mixing mass is degenerate with the Eu yield from each event. If we combine both the (ii) and (iii) arguments, it is possible to explain the Eu abundance of Tuc III. To reject such possibility we need a lot of UFD observations at relatively low [Eu/H]. Since the hydrogen

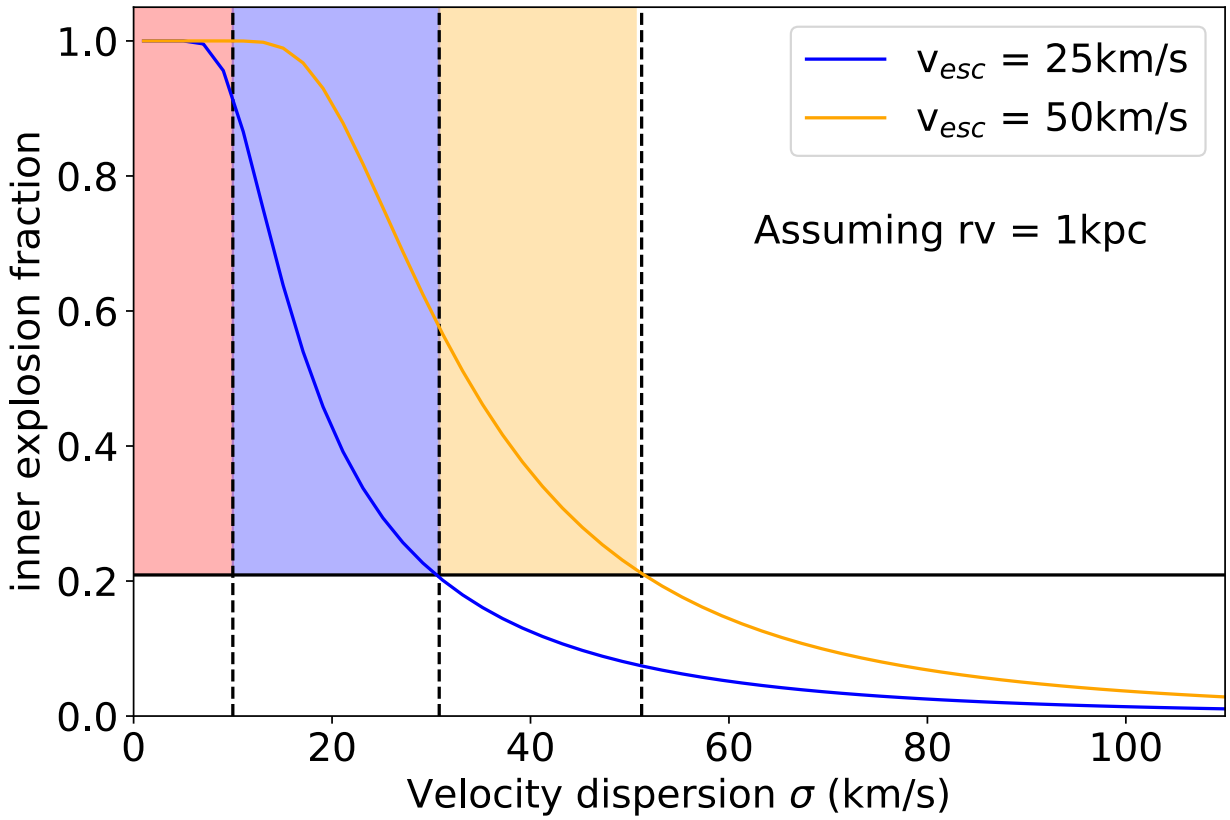


Figure 43: The fractions of NSM that happens inside virial radius. Blue and orange curves represent two different halos with different escape velocities. For this calculation we assume that the velocity distribution follows Maxwell-Boltzmann distribution. The horizontal axis is the velocity dispersion of the velocity distribution. The horizontal solid line is the "5% significance level". This fraction corresponds to the level below which the inner explosion fractions are incompatible with the observation at 5 % significance level. Any binary neutron star system is kicked at least $\sim$ 10 km/s (Beniamini et al. 2016) because the instant mass-loss via neutrino kicks the binary neutron-star system with this speed.

dilution mass range of UFD progenitors is narrow, a wider distribution of [Eu/H] can be used as the proof of outskirt explosion. For scenario (iii), we have i-process in magneto-rorational SNe (MRSNe) (Nishimura et al. 2017b) as a candidate for small-yield event. In this event the neutron richness is moderate, therefore elemental abundances do not follow the full pattern of r-process elements. Since the nucleus of Eu is massive in r-process path, the production of Eu is smaller than the values usually assumed. However, stars in Tuc III are lanthanide-rich (Ji et al. 2019a), suggesting that the origin of r-process elements in Tuc III should have quite neutron-rich environment. Since we do not know any such a neutron-rich but low r-process yield event, this scenario is also unlikely.

It is interesting to point out that we have never detected Eu in stars in other UFDs, but some stars contain Ba and Sr. The origins can be s-process or r-process, but it is shown that considering their metallicities the s-process contribution should be minor, leaving r-process

| | Time-lag < 100 Myr | Time-lag > 100 Myr |
|---|---|---|
| R<$r_v$ | High abundance, large scatter | High abundance, small scatter |
| R>$r_v$ | Almost no r-process elements | Medium abundance, medium-small scatter |

Table 3: A summary of the relation between Eu abundance observation and progenitor halo properties.

as the only source of these elements (Ji et al. 2019b). In Fig. 39 we show that if an NSM happens outside the virial radius, the stars in UFDs can be enriched to a very low level. The stars in other UFDs that contain Ba are typically enriched to [Ba/H]$\sim -4$ (Ji et al. 2019b). If we assume that all the Ba in these stars come from r-process, their Eu abundances should be [Eu/H]$\sim -3.1$ (Burris et al. 2000). Although in Fig. 39 the range is not shown, this [Eu/H] typically corresponds to the models that NSM happens at the point with the offset of $3r_{\rm vir}$.

In summary, the moderate Eu enrichment of Tuc III can be explained naturally be an NSM in the ourskirt of the progenitor. If we find more UFDs with [Eu/H] $\sim -3$ we can be more confident that the origin of r-process element in the UFDs are NSMs. They are the only source that allow moderate enrichment.

## 14.4 Other implications

In Table 3 we summarize our analysis. From the Eu abundances of stars in a UFD, we can infer the time lag between the NSM and typical star formation in the galaxy, and the distance of the explosion site from the center. The time-lag between NSM and typical star formation determines the scatter of Eu abundance. If the time-lag is short, so that most of the stars are formed before the NSM ejecta dilution, the abundance scatter is large. If the star formation lasts long, so that most of the stars are formed after the dilution, then the abundance scatter is small. The distance of the explosion site from the center determines the overall abundance of Eu. The critical radius is around the virial radius. A larger explosion energy leads to larger mixing mass, which makes our initial condition more homogeneous. However, the radius of the snouplough bubble only depends weakly on the energy. Therefore also in such cases the dominant dilution mechanism is the turbulent motions of ISM. The explosion energy do not significantly affect the result.

Lastly, we discuss the implications for r-process enrichment in globular clusters (GCs). At least half of GCs contain r-process enriched stars (Roederer 2011). The modeling of r-process enrichment of GCs is far from complete. The important problems are: the origin of r-process enrichment, and the very small scatter of Eu abundance (Bekki and Tsujimoto 2017). We argue that the r-process enrichment of stars in GCs can possibly explained by one of our models, although the UFDs we have investigated are more extended systems. In a UFD with long star formation, r-process elements are mixed well with the hydrogen gas in the galaxy. This is consistent to the chemical feature of stars in GCs.

Our conclusion for the Part III is as follows:

1. The Eu abundance in Ret II and Tuc III both can be explained by a NSM scenario.

2. The UFD can be enriched to [Eu/H] $\sim -0.5$, if an NSM or any kinds of r-process events occurs inside the virial radius of a UFD progenitor. Considering the shallow potential well of UFD progenitors, the NSM should happen before the cosmic reionization.

3. The high Eu abundance in Ret II is consistent to the central explosion scenario, and the mediocre Eu abundance in Tuc III is consistent to the outskirt ($\sim$ virial radius) explosion scenario. Binary neutron-stars can have initial velocity of a few tens of km/s, which is similar to the escape velocity of the galaxy and is consistent to the outskirt explosion scenario.

# Part IV
# Summary

In this thesis I investigated the dilution of heavy elements produced in explosive events in the Universe. Our work has clarified that inhomogeneity of metallicity in each galaxy is large if the galaxy has never formed stars. When we try to model the Pop III to Pop II transition analytically we have to be aware of this inhomogeneity: we need more metals to sufficiently enrich neighboring halos than in naive calculation. We have built a model to properly take inhomogeneity into account. With this model we can further study the chemical evolution of galaxies.

Through the hydrodynamical modeling of an r-process enriched UFD we have suggested that the elemental abundance distribution of stars in a galaxy can be used to infer the star formation history of the UFD progenitor. Since r-process dominantly occurs in rare events, small systems such as UFDs are an ideal laboratory for disentangling complex chemical evolution. An interesting connection has pointed out that typical [Eu/Fe] of highly r-process enriched stars in the halo is similar to the one of Ret II, a highly r-process enriched UFD. This coincidence may suggesting that the halo stars are originated from disrupted dwarf galaxies. Also, very recently "dynamical tagging" of halo stars are conducted with Gaia DR2. Such detailed dynamical information can increase the sample size of satellite galaxies. Chemical modeling of satellite (dwarf, ultrafaint dwarf) galaxies are important because it is quite promising to have new information on multiple fields, including the element synthesis, by directly comparing the results to upcoming observations.

It would be interesting if we could study the evolution of other elements. The origin of CEMP-s stars is probably the AGB stars, but the origin of CEMP-r stars is unknown, since we do not know any nucleosynthesis event that produces carbon and r-process elements at the same time. The origin may just be a coincidence of carbon-enhancing and r-process nucleosynthesis events, or there may be some unknown astrophysical site. Such combination modeling can further constrain the chemical evolution of the Universe. A perfect chemical evolution model should reproduce the abundances of all elements. Of course this is nothing but a dream from the current status, but through the refinement of chemical evolution models we continuously learn about the physics in the Universe. In this sense the "dream" can serve as a guidance for us to keep going. We still have quite a long way to go, but the future is bright: there are a lot of mysteries waiting to be solved.

# 15 Acknowledgement

I would like to express my deepest gratitude to my supervisor Naoki Yoshida for his generous supports. He introduced me to a very interesting and stimulating research topic, help me learn the backgrounds to do research, and give me very valuable advices to present the results in a sophisticated manner. He help me improve my poorly written draft (like abstracts of conferences or the texts of papers) to a sophisticated science text.

My research would not have been possible without the greatest help from Tilman Hartwig. I would like to cordially thank him. He let me use the code he has implemented, and patiently keep teaching me how to use the code. I learned a lot from innumerable discussions I had with him. I asked so many questions, and he answers most of them: he is the source of most of the knowledge I have acquired. Also he gave me very constructive advice to all of my scientific things, including presentations and this thesis. I also learned a lot of non-scientific things through the discussions: it was a very good breather for me to hear his stories.

I also want to thank Shigeki Inoue for teaching me how to run a cosmological simulation with AREPO, which made me possible to write Part III of this thesis. His technical support has been essential for my work, and the skills he let me acquire will also be very useful throughout my research.

I want to thank my current roommates: Kazumi, Taizo, Masataka, Kojiro, Yuta, Conor, Shijie, and Kana for very enjoyable atmosphere. They helped me in many moments, for instance how to show figures on a paper on Overleaf, or to buy a boxful of orange and share with us to relax. I also want to thank my former roommates: Hiroto, Takumi, Jun'ya, Takuya, Saku, Yuting for relaxing but stimulating atmosphere we had in M1 room. Special thanks to Takumi, who often let me stay at his house and help me learn physics.

Finally, I want to thank my family, especially my parents, to support me throughout my life. Without their support I would not have been able to work for the stimulating world of research that I love. Especially I want to thank my mother, Yukiko, for patiently teaching me the importance of diligence when I learn new things.

# References


H. A. Abt. Normal and abnormal binary frequencies. *Annual Review of Astronomy and Astrophysics*, 21:343–372, Jan 1983. doi: 10.1146/annurev.aa.21.090183.002015.

Bhaskar Agarwal, Sadegh Khochfar, Jarrett L. Johnson, Eyal Neistein, Claudio Dalla Vecchia, and Mario Livio. Ubiquitous seeding of supermassive black holes by direct collapse. *Monthly Notices of the Royal Astronomical Society*, 425:2854–2871, Oct 2012. doi: 10.1111/j.1365-2966.2012.21651.x.

A. Arentsen, E. Starkenburg, M. D. Shetrone, K. A. Venn, É. Depagne, and A. W. McConnachie. Binarity among CEMP-no stars: an indication of multiple formation pathways? *Astronomy and Astrophysics*, 621:A108, Jan 2019. doi: 10.1051/0004-6361/201834146.

Jennifer Barnes and Daniel Kasen. Effect of a High Opacity on the Light Curves of Radioactively Powered Transients from Compact Object Mergers. *Astrophysical Journal*, 775(1): 18, Sep 2013. doi: 10.1088/0004-637X/775/1/18.

K. Bechtol et al. Eight New Milky Way Companions Discovered in First-year Dark Energy Survey Data. *Astrophysical Journal*, 807(1):50, Jul 2015. doi: 10.1088/0004-637X/807/1/50.

Kenji Bekki and Takuji Tsujimoto. Formation of Globular Clusters with Internal Abundance Spreads in r-Process Elements: Strong Evidence for Prolonged Star Formation. *Astrophysical Journal*, 844(1):34, Jul 2017. doi: 10.3847/1538-4357/aa77ae.

Andrei M. Beloborodov. Nuclear Composition of Gamma-Ray Burst Fireballs. *Astrophysical Journal*, 588(2):931–944, May 2003. doi: 10.1086/374217.

Paz Beniamini, Kenta Hotokezaka, and Tsvi Piran. Natal Kicks and Time Delays in Merging Neutron Star Binaries: Implications for r-process Nucleosynthesis in Ultra-faint Dwarfs and in the Milky Way. *Astrophysical Journal*, 829(1):L13, Sep 2016. doi: 10.3847/2041-8205/829/1/L13.

Greg L. others Bryan. ENZO: An Adaptive Mesh Refinement Code for Astrophysics. *Astrophysical Journal Supplement Series*, 211(2):19, Apr 2014. doi: 10.1088/0067-0049/211/2/19.

Debra L. Burris et al. Neutron-Capture Elements in the Early Galaxy: Insights from a Large Sample of Metal-poor Giants. *Astrophysical Journal*, 544(1):302–319, Nov 2000. doi: 10.1086/317172.

Gilles Chabrier. The Galactic Disk Mass Budget. I. Stellar Mass Function and Density. *Astrophysical Journal*, 554(2):1274–1281, Jun 2001. doi: 10.1086/321401.

K.-J. Chen, A. Heger, D. J. Whalen, T. J. Moriya, V. Bromm, and S. E. Woosley. Low-energy Population III supernovae and the origin of extremely metal-poor stars. *Monthly Notices of the Royal Astronomical Society*, 467:4731–4738, June 2017. doi: 10.1093/mnras/stx470.

G. Chiaki, H. Susa, and S. Hirano. Metal-poor star formation triggered by the feedback effects from Pop III stars. *Monthly Notices of the Royal Astronomical Society*, 475:4378–4395, April 2018. doi: 10.1093/mnras/sty040.

Gen Chiaki, Nozomu Tominaga, and Takaya Nozawa. Classification of extremely metal-poor stars: absent region in A(C)-[Fe/H] plane and the role of dust cooling. *Monthly Notices of the Royal Astronomical Society*, 472(1):L115–L119, Nov 2017. doi: 10.1093/mnrasl/slx163.

Benoit Côté, Devin W. Silvia, Brian W. O'Shea, Britton Smith, and John H. Wise. Validating Semi-analytic Models of High-redshift Galaxy Formation Using Radiation Hydrodynamical Simulations. *Astrophysical Journal*, 859(1):67, May 2018. doi: 10.3847/1538-4357/aabe8f.

Benoit Côté et al. Neutron Star Mergers Might Not Be the Only Source of r-process Elements in the Milky Way. *Astrophysical Journal*, 875(2):106, Apr 2019. doi: 10.3847/1538-4357/ab10db.

John J. Cowan et al. Making the Heaviest Elements in the Universe: A Review of the Rapid Neutron Capture Process. *arXiv e-prints*, art. arXiv:1901.01410, Jan 2019.

P. S. Cowperthwaite et al. The Electromagnetic Counterpart of the Binary Neutron Star Merger LIGO/Virgo GW170817. II. UV, Optical, and Near-infrared Light Curves and Comparison to Kilonova Models. *Astrophysical Journal Letters*, 848(2):L17, Oct 2017. doi: 10.3847/2041-8213/aa8fc7.

M. de Bennassuti, S. Salvadori, R. Schneider, R. Valiante, and K. Omukai. Limits on Population III star formation with the most iron-poor stars. *Monthly Notices of the Royal Astronomical Society*, 465(1):926–940, Feb 2017. doi: 10.1093/mnras/stw2687.

M. Eichler, A. Arcones, A. Kelic, O. Korobkin, K. Langanke, T. Marketin, G. Martinez-Pinedo, I. Panov, T. Rauscher, S. Rosswog, C. Winteler, N. T. Zinner, and F. K. Thielemann. The Role of Fission in Neutron Star Mergers and Its Impact on the r-Process Peaks. *Astrophysical Journal*, 808(1):30, Jul 2015. doi: 10.1088/0004-637X/808/1/30.

A. Emerick et al. Metal Mixing and Ejection in Dwarf Galaxies Are Dependent on Nucleosynthetic Source. *Astrophysical Journal*, 869:94, December 2018. doi: 10.3847/1538-4357/aaec7d.

Roberto Gallino, Claudio Arlandini, Maurizio Busso, Maria Lugaro, Claudia Travaglio, Oscar Straniero, Alessandro Chieffi, and Marco Limongi. Evolution and Nucleosynthesis in Low-Mass Asymptotic Giant Branch Stars. II. Neutron Capture and the S-Process. *Astrophysical Journal*, 497(1):388–403, Apr 1998. doi: 10.1086/305437.

Shea Garrison-Kimmel, Michael Boylan-Kolchin, James S. Bullock, and Evan N. Kirby. Too big to fail in the Local Group. *Monthly Notices of the Royal Astronomical Society*, 444(1): 222–236, Oct 2014. doi: 10.1093/mnras/stu1477.

Simon Glover. *The First Stars*, volume 396 of *Astrophysics and Space Science Library*, page 103. 2013. doi: 10.1007/978-3-642-32362-1_3.

Robert J. J. Grand, Facundo A. G¥'omez, Federico Marinacci, R¥"udiger Pakmor, Volker Springel, David J. R. Campbell, Carlos S. Frenk, Adrian Jenkins, and Simon D. M. White. The Auriga Project: the properties and formation mechanisms of disc galaxies across cosmic time. *Monthly Notices of the Royal Astronomical Society*, 467(1):179–207, May 2017. doi: 10.1093/mnras/stx071.

Thomas H. Greif and Volker Bromm. Two populations of metal-free stars in the early Universe. *Monthly Notices of the Royal Astronomical Society*, 373(1):128–138, Nov 2006. doi: 10.1111/j.1365-2966.2006.11017.x.

Brendan F. Griffen et al. The Caterpillar Project: A Large Suite of Milky Way Sized Halos. *Astrophysical Journal*, 818(1):10, Feb 2016. doi: 10.3847/0004-637X/818/1/10.

Oliver Hahn and Tom Abel. Multi-scale initial conditions for cosmological simulations. *Monthly Notices of the Royal Astronomical Society*, 415(3):2101–2121, Aug 2011. doi: 10.1111/j.1365-2966.2011.18820.x.

T. T. Hansen, J. D. Simon, J. L. Marshall, T. S. Li, D. Carollo, D. L. DePoy, D. Q. Nagasawa, R. A. Bernstein, A. Drlica-Wagner, and F. B. Abdalla. An r-process Enhanced Star in the Dwarf Galaxy Tucana III. *Astrophysical Journal*, 838(1):44, Mar 2017. doi: 10.3847/1538-4357/aa634a.

Tilman Hartwig and Naoki Yoshida. Formation of Carbon-enhanced Metal-poor Stars As a Consequence of Inhomogeneous Metal Mixing. *Astrophysical Journal Letters*, 870(1):L3, Jan 2019. doi: 10.3847/2041-8213/aaf866.

Tilman Hartwig, Volker Bromm, Ralf S. Klessen, and Simon C. O. Glover. Constraining the primordial initial mass function with stellar archaeology. *Monthly Notices of the Royal Astronomical Society*, 447(4):3892–3908, Mar 2015. doi: 10.1093/mnras/stu2740.

Tilman Hartwig et al. Descendants of the first stars: the distinct chemical signature of second-generation stars. *Monthly Notices of the Royal Astronomical Society*, 478(2):1795–1810, Aug 2018. doi: 10.1093/mnras/sty1176.

Yutaka Hirai and Takayuki R. Saitoh. Efficiency of Metal Mixing in Dwarf Galaxies. *Astrophysical Journal*, 838(2):L23, Apr 2017. doi: 10.3847/2041-8213/aa6799.

S. Hirano, T. Hosokawa, N. Yoshida, K. Omukai, and H. W. Yorke. Primordial star formation under the influence of far ultraviolet radiation: 1540 cosmological haloes and the stellar mass distribution. *Monthly Notices of the Royal Astronomical Society*, 448(1):568–587, Mar 2015. doi: 10.1093/mnras/stv044.

Shingo Hirano et al. One Hundred First Stars: Protostellar Evolution and the Final Masses. *Astrophysical Journal*, 781(2):60, Feb 2014. doi: 10.1088/0004-637X/781/2/60.

R. A. Hulse and J. H. Taylor. Discovery of a pulsar in a binary system. *Astrophysical Journal Letters*, 195:L51–L53, Jan 1975. doi: 10.1086/181708.

Miho N. Ishigaki, Nozomu Tominaga, Chiaki Kobayashi, and Ken'ichi Nomoto. Faint Population III Supernovae as the Origin of the Most Iron-poor Stars. *Astrophysical Journal Letters*, 792(2):L32, Sep 2014. doi: 10.1088/2041-8205/792/2/L32.

M. Jeon, A. H. Pawlik, V. Bromm, and M. Milosavljević. Recovery from Population III supernova explosions and the onset of second-generation star formation. *Monthly Notices of the Royal Astronomical Society*, 444:3288–3300, November 2014. doi: 10.1093/mnras/stu1980.

A. P. Ji, A. Frebel, and V. Bromm. Preserving chemical signatures of primordial star formation in the first low-mass stars. *Monthly Notices of the Royal Astronomical Society*, 454: 659–674, November 2015. doi: 10.1093/mnras/stv2052.

Alexander P. Ji, Anna Frebel, Anirudh Chiti, and Joshua D. Simon. R-process enrichment from a single event in an ancient dwarf galaxy. *Nature*, 531(7596):610–613, Mar 2016. doi: 10.1038/nature17425.

Alexander P. Ji, Maria R. Drout, and Terese T. Hansen. The lanthanide fraction distribution in metal-poor stars: a test of neutron star mergers as the dominant r-process site. *arXiv e-prints*, art. arXiv:1905.01814, May 2019a.

Alexander P. Ji et al. Chemical Abundances in the Ultra-faint Dwarf Galaxies Grus I and Triangulum II: Neutron-capture Elements as a Defining Feature of the Faintest Dwarfs. *Astrophysical Journal*, 870(2):83, Jan 2019b. doi: 10.3847/1538-4357/aaf3bb.

T. Karlsson. Stochastic chemical enrichment in metal-poor systems. I. Theory. *Astronomy and Astrophysics*, 439(1):93–106, Aug 2005. doi: 10.1051/0004-6361:20041934.

Sara Lucatello, Stelios Tsangarides, Timothy C. Beers, Eugenio Carretta, Raffaele G. Gratton, and Sean G. Ryan. The Binary Frequency Among Carbon-enhanced, s-Process-rich, Metal-poor Stars. *Astrophysical Journal*, 625(2):825–832, Jun 2005. doi: 10.1086/428104.

Mattis Magg, Ralf S. Klessen, Simon C. O. Glover, and Haining Li. Observational constraints on the survival of pristine stars. *Monthly Notices of the Royal Astronomical Society*, 487 (1):486–490, Jul 2019. doi: 10.1093/mnras/stz1210.

Mattis Magg et al. Predicting the locations of possible long-lived low-mass first stars: importance of satellite dwarf galaxies. *Monthly Notices of the Royal Astronomical Society*, 473(4):5308–5323, Feb 2018. doi: 10.1093/mnras/stx2729.

Dan Maoz, Filippo Mannucci, and Timothy D. Brandt. The delay-time distribution of Type Ia supernovae from Sloan II. *Monthly Notices of the Royal Astronomical Society*, 426(4): 3282–3294, Nov 2012. doi: 10.1111/j.1365-2966.2012.21871.x.

J. Marshall et al. Chemical Abundance Analysis of Tucana III, the Second *r*-process Enhanced Ultra-Faint Dwarf Galaxy. *arXiv e-prints*, art. arXiv:1812.01022, Dec 2018.

A. Mirizzi et al. Supernova neutrinos: production, oscillations and detection. *Nuovo Cimento Rivista Serie*, 39(1-2):1–112, Jan 2016. doi: 10.1393/ncr/i2016-10120-8.

H. Mo, F. C. van den Bosch, and S. White. *Galaxy Formation and Evolution*. May 2010.

H. J. Mo, Shude Mao, and Simon D. M. White. The formation of galactic discs. *Monthly Notices of the Royal Astronomical Society*, 295(2):319–336, Apr 1998. doi: 10.1046/j.1365-8711.1998.01227.x.

N. Nishimura, H. Sawai, T. Takiwaki, S. Yamada, and F. K. Thielemann. The Intermediate r-process in Core-collapse Supernovae Driven by the Magneto-rotational Instability. *Astrophysical Journal Letters*, 836(2):L21, Feb 2017a. doi: 10.3847/2041-8213/aa5dee.

N. Nishimura, H. Sawai, T. Takiwaki, S. Yamada, and F. K. Thielemann. The Intermediate r-process in Core-collapse Supernovae Driven by the Magneto-rotational Instability. *Astrophysical Journal*, 836(2):L21, Feb 2017b. doi: 10.3847/2041-8213/aa5dee.

Nobuya Nishimura, Tomoya Takiwaki, and Friedrich-Karl Thielemann. The r-process Nucleosynthesis in the Various Jet-like Explosions of Magnetorotational Core-collapse Supernovae. *Astrophysical Journal*, 810(2):109, Sep 2015. doi: 10.1088/0004-637X/810/2/109.

Ken'ichi Nomoto, Chiaki Kobayashi, and Nozomu Tominaga. Nucleosynthesis in Stars and the Chemical Enrichment of Galaxies. *Annual Review of Astronomy and Astrophysics*, 51 (1):457–509, Aug 2013. doi: 10.1146/annurev-astro-082812-140956.

John E. Norris and David Yong. The Most Metal-poor Stars. V. The CEMP-no Stars in 3D and Non-LTE. *Astrophysical Journal*, 879(1):37, Jul 2019. doi: 10.3847/1538-4357/ab1f84.

Kazuyuki Omukai. Protostellar Collapse with Various Metallicities. *Astrophysical Journal*, 534(2):809–824, May 2000. doi: 10.1086/308776.

Brian W. O'Shea and Michael L. Norman. Population III Star Formation in a ΛCDM Universe. II. Effects of a Photodissociating Background. *Astrophysical Journal*, 673(1): 14–33, Jan 2008. doi: 10.1086/524006.

Vinicius M. Placco, Anna Frebel, Timothy C. Beers, and Richard J. Stancliffe. Carbon-enhanced Metal-poor Star Frequencies in the Galaxy: Corrections for the Effect of Evolutionary Status on Carbon Abundances. *Astrophysical Journal*, 797(1):21, Dec 2014. doi: 10.1088/0004-637X/797/1/21.

William H. Press and Paul Schechter. Formation of Galaxies and Clusters of Galaxies by Self-Similar Gravitational Condensation. *Astrophysical Journal*, 187:425–438, Feb 1974. doi: 10.1086/152650.

Yves Revaz, Alexis Arnaudon, Matthew Nichols, Vivien Bonvin, and Pascale Jablonka. Computational issues in chemo-dynamical modelling of the formation and evolution of galaxies. *Astronomy and Astrophysics*, 588:A21, Apr 2016. doi: 10.1051/0004-6361/201526438.

Ian U. Roederer. Primordial r-process Dispersion in Metal-poor Globular Clusters. *Astrophysical Journal*, 732(1):L17, May 2011. doi: 10.1088/2041-8205/732/1/L17.

S. Rosswog et al. Detectability of compact binary merger macronovae. *Classical and Quantum Gravity*, 34(10):104001, May 2017. doi: 10.1088/1361-6382/aa68a9.

Mohammadtaher Safarzadeh and Evan Scannapieco. Simulating neutron star mergers as r-process sources in ultrafaint dwarf galaxies. *Monthly Notices of the Royal Astronomical Society*, 471(2):2088–2096, Oct 2017. doi: 10.1093/mnras/stx1706.

Mohammadtaher Safarzadeh, Richard Sarmento, and Evan Scannapieco. On Neutron Star Mergers as the Source of r-process Enhanced Metal Poor Stars in the Milky Way. *arXiv e-prints*, art. arXiv:1812.02779, Dec 2018a.

Mohammadtaher Safarzadeh, Richard Sarmento, and Evan Scannapieco. On Neutron Star Mergers as the Source of r-process-enhanced Metal-poor Stars in the Milky Way. *Astrophysical Journal*, 876(1):28, May 2019a. doi: 10.3847/1538-4357/ab1341.

Mohammadtaher Safarzadeh et al. Selecting ultra-faint dwarf candidate progenitors in cosmological N-body simulations at high redshifts. *Monthly Notices of the Royal Astronomical Society*, 476(4):5006–5015, Jun 2018b. doi: 10.1093/mnras/sty595.

Mohammadtaher Safarzadeh et al. r-process Enrichment of the Ultra-faint Dwarf Galaxies by Fast-merging Double-neutron Stars. *Astrophysical Journal*, 872(1):105, Feb 2019b. doi: 10.3847/1538-4357/aafe0e.

R. Sarmento, E. Scannapieco, and L. Pan. Following the Cosmic Evolution of Pristine Gas. I. Implications for Milky Way Halo Stars. *Astrophysical Journal*, 834:23, January 2017. doi: 10.3847/1538-4357/834/1/23.

R. Sarmento, E. Scannapieco, and B. Côté. Following the Cosmic Evolution of Pristine Gas. III. The Observational Consequences of the Unknown Properties of Population III Stars. *Astrophysical Journal*, 871:206, February 2019. doi: 10.3847/1538-4357/aafa1a.

Anna T. P. Schauer, Simon C. O. Glover, Ralf S. Klessen, and Daniel Ceverino. The influence of streaming velocities on the formation of the first stars. *Monthly Notices of the Royal Astronomical Society*, 484(3):3510–3521, Apr 2019. doi: 10.1093/mnras/stz013.

Raffaella Schneider, Kazuyuki Omukai, Simone Bianchi, and Rosa Valiante. The first low-mass stars: critical metallicity or dust-to-gas ratio? *Monthly Notices of the Royal Astronomical Society*, 419(2):1566–1575, Jan 2012. doi: 10.1111/j.1365-2966.2011.19818.x.

Daniel M. Siegel, Jennifer Barnes, and Brian D. Metzger. Collapsars as a major source of r-process elements. *Nature*, 569(7755):241–244, May 2019. doi: 10.1038/s41586-019-1136-0.

J. D. Simon et al. Stellar Kinematics and Metallicities in the Ultra-faint Dwarf Galaxy Reticulum II. *Astrophysical Journal*, 808(1):95, Jul 2015. doi: 10.1088/0004-637X/808/1/95.

J. D. Simon et al. Nearest Neighbor: The Low-mass Milky Way Satellite Tucana III. *Astrophysical Journal*, 838(1):11, Mar 2017. doi: 10.3847/1538-4357/aa5be7.

Joshua D. Simon. The Faintest Dwarf Galaxies. *arXiv e-prints*, art. arXiv:1901.05465, Jan 2019.

Britton D. Smith, John H. Wise, Brian W. O'Shea, Michael L. Norman, and Sadegh Khochfar. The first Population II stars formed in externally enriched mini-haloes. *Monthly Notices of the Royal Astronomical Society*, 452(3):2822–2836, Sep 2015. doi: 10.1093/mnras/stv1509.

Volker Springel and Lars Hernquist. Cosmological smoothed particle hydrodynamics simulations: a hybrid multiphase model for star formation. *¥mnras*, 339(2):289–311, Feb 2003. doi: 10.1046/j.1365-8711.2003.06206.x.

T. Suda et al. Stellar Abundances for the Galactic Archeology (SAGA) Database — Compilation of the Characteristics of Known Extremely Metal-Poor Stars. *PASJ*, 60:1159–1171, October 2008. doi: 10.1093/pasj/60.5.1159.

Freeke van de Voort, Rüdiger Pakmor, Robert J. J. Grand , Volker Springel, Facundo A. Gómez, and Federico Marinacci. Neutron star mergers and rare core-collapse supernovae as sources of r-process enrichment in simulated galaxies. *arXiv e-prints*, art. arXiv:1907.01557, Jul 2019.

F. Vincenzo, F. Matteucci, F. Belfiore, and R. Maiolino. Modern yields per stellar generation: the effect of the IMF. *Monthly Notices of the Royal Astronomical Society*, 455:4183–4190, February 2016. doi: 10.1093/mnras/stv2598.

Mark Vogelsberger, Shy Genel, Debora Sijacki, Paul Torrey, Volker Springel, and Lars Hernquist. A model for cosmological simulations of galaxy formation physics. *Monthly Notices of the Royal Astronomical Society*, 436(4):3031–3067, Dec 2013. doi: 10.1093/mnras/stt1789.

J. M. Weisberg and Y. Huang. Relativistic Measurements from Timing the Binary Pulsar PSR B1913+16. *Astrophysical Journal*, 829(1):55, Sep 2016. doi: 10.3847/0004-637X/829/1/55.

S. E. Woosley. Gamma-Ray Bursts from Stellar Mass Accretion Disks around Black Holes. *Astrophysical Journal*, 405:273, Mar 1993. doi: 10.1086/172359.

Hao Xu, John H. Wise, Michael L. Norman, Kyungjin Ahn, and Brian W. O'Shea. Galaxy Properties and UV Escape Fractions during the Epoch of Reionization: Results from the Renaissance Simulations. *Astrophysical Journal*, 833:84, Dec 2016. doi: 10.3847/1538-4357/833/1/84.

Jinmi Yoon et al. Observational Constraints on First-star Nucleosynthesis. I. Evidence for Multiple Progenitors of CEMP-No Stars. *Astrophysical Journal*, 833(1):20, Dec 2016. doi: 10.3847/0004-637X/833/1/20.

K. Youakim et al. The Pristine survey - III. Spectroscopic confirmation of an efficient search for extremely metal-poor stars. *Monthly Notices of the Royal Astronomical Society*, 472 (3):2963–2974, Dec 2017. doi: 10.1093/mnras/stx2005.